



Schweizerische Eidgenossenschaft
Confédération suisse
Confederazione Svizzera
Confederaziun svizra

Eidgenössisches Departement des Innern EDI
Bundesamt für Meteorologie und Klimatologie MeteoSchweiz

Veröffentlichung MeteoSchweiz Nr. 79

Radiation and clouds: observations and model calculations for Payerne BSRN site

Daniela Nowak



Veröffentlichung MeteoSchweiz Nr. 79

ISSN: 1422-1381

Radiation and clouds: observations and model calculations for Payerne BSRN site

Daniela Nowak

Bitte zitieren Sie diese Veröffentlichung folgendermassen

Nowak, D: 2008, Radiation and clouds: observations and model calculations for Payerne BSRN site, *Veröffentlichungen der MeteoSchweiz*, **79**, 101 pp.

Herausgeber

Bundesamt für Meteorologie und Klimatologie, MeteoSchweiz, © 2008

MeteoSchweiz
Krähbühlstrasse 58
CH-8044 Zürich
T +41 44 256 91 11
www.meteoschweiz.ch

Weitere Standorte
CH-8058 Zürich-Flughafen
CH-6605 Locarno Monti
CH-1211 Genève 2
CH-1530 Payerne

Diss. ETH No. 17687

Radiation and clouds: observations and model calculations for Payerne BSRN site

A dissertation submitted to the
SWISS FEDERAL INSTITUTE OF TECHNOLOGY (ETH)
ZURICH

for the degree of
DOCTOR OF SCIENCES

presented by
DANIELA NOWAK
Dipl. phil. nat.
born 20 June 1975
citizen of Luzern (LU)

accepted on the recommendation of
Prof. Dr. A. Ohmura, examiner
Dr. L. Vuilleumier, co-examiner
Prof. Dr. H. Fischer, co-examiner
Prof. Dr. R. Knutti, co-examiner

2008

Abstract

Effect of clouds in a changing climate represent a major source of uncertainty in simulation for future climate. Among other, these uncertainties include changes in cloud cover, cloud lifetime, and response of cloud cover to increasing greenhouse gases. Cloud effect on the radiation budget in a future climate change is therefore an important issue.

The aim of this thesis is to improve the understanding of radiation transfer in cloudy atmosphere by determining the effect of a given cloud class (stratiform clouds) on short-wave (solar) radiation fluxes at Payerne (Switzerland). For this purpose, a method is devised that can be applied to longterm time series issued from operational monitoring at aerological stations. A first step is devoted to verifying how well single cloud layer situations can be identified, and how well the lower and upper boundary of the cloud layer can be determined. This step relies on comparing data obtained via operational monitoring (remote sensing and in-situ radiosounding) with data from an intensive observational period (TUC - Temperature hUmidity and Cloud campaign) conducted at Payerne. In a second step, the validity of our understanding (model simulation) of radiation transfer in clear-sky atmosphere is tested with observational data. In a third step, selected single cloud layer situations are simulated with a radiation transfer model, and the simulation results are verified with observational data at the surface and the top of the atmosphere. These simulations are then used to infer the absorbance, transmittance and reflectance of the single cloud layer for each selected situation. In parallel an empirical method is also applied to determine the cloud effect uniquely from observational data.

The Baseline Surface Radiation Network (BSRN) aims at longterm high accuracy radiation monitoring, and includes 39 stations over the globe. One of the BSRN stations is collocated with the Payerne aerological station of the Federal Office of Meteorology and Climatology, MeteoSwiss. Since 1992, short- and longwave downward and upward radiation is observed according to BSRN guidelines. Additionally, aerosol optical depth (AOD) observations are performed since October 2000. Surface observations of the cloud cover, type and altitude are performed at 3 hours intervals (synop), during day and night. Finally, balloon-borne meteorological radiosoundings including temperature, humidity and pressure profiles, are performed twice a day. Together with additional surface observations from Payerne and from other meteorological stations in Switzerland, these data sets are the basis for the studies presented here.

During the experimental TUC campaign in winter 2003/2004, a cloud radar and a ceilometer were simultaneously operated in Payerne. A method for automatic detection of fog and stratus cloud lower and upper boundaries is presented. The ceilometer shows high

efficiency for fog and cloud-base detection ($> 95\%$). The cloud radar, which represents a prototype instrument, reveals less reliability ($< 60\%$) for the cloud- and fog-top detection. Furthermore, a comparison of the cloud-top detection with cloud radar and radiosounding temperature and humidity profiles is performed. The results show that a positive bias on the order of 50 m exists between the radiosounding and cloud radar determination of the upper cloud boundary.

AOD observations, radiosounding profiles and further meteorological observations from 2001 to 2005 are used for clear sky radiation simulations with MODTRANTM. Comparison of modeled shortwave downward radiation (*SDR*) and BSRN observations show good agreement for the global *SDR*, with an accuracy well within instrument precision ($< 1\%$). The model simulations for diffuse *SDR* reveal more difficulties, and the model to observation linear regression slope and zero-intercept differ significantly from their ideal value of 1 and 0. Hypothesis for explaining the discrepancies and propositions for improving the agreement between modeled and observed diffuse *SDR* are given. The clear sky radiation transfer simulations allow the determination of the RTM MODTRANTM performance for the Payerne site.

An empirical method to determine the cloud effect on radiation was tried in parallel to the theoretically based method at the core of this thesis. An algorithm based on *SDR* and *LDR* observations is used for the detection of clear sky radiation measurements and the estimation of clear sky *SDR* and *LDR* during cloudy moments. A combination of the synoptic surface cloud observations and the BSRN radiation data allows the determination of the effect of all sky situations on the incoming *SDR* and *LDR*. For the time period 1998 to 2003, clouds are responsible for an average 36 Wm^{-2} reduction of the net incoming radiation at the Payerne observation site. Furthermore, the effect of clouds on incoming radiation depends on the cloud type.

Relying on the previous findings, a method is developed to deduce absorbance, absorption and reflectance of solar radiation for well-defined stratiform cloud cases with RTM MODTRANTM. The Clouds and the Earth's Radiant Energy System experiment provided a data set of shortwave upward radiation (*SUR*) observations at the top of atmosphere (TOA), collocated with the Payerne BSRN station. This data set allows to simulate radiation transfer including a single cloud layer so that there is reasonable agreement with observations both for surface *SDR* and *SUR* at TOA. The median differences of the model and the observations are on the order of 9 % at the TOA, and the corresponding differences for surface model and observation is $< 1\%$. The median absorbance between cloud base and cloud top is 0.22, and the absorption is on the order of 28 Wm^{-2} .

Zusammenfassung

Der Effekt der Wolken sorgt für grosse Unsicherheiten bei der Modellierung der künftigen Klimaentwicklung. Diese Unsicherheiten beinhalten Veränderungen der Wolkenbedeckung und Lebensdauer der Wolken sowie die Reaktion der Wolkendecke auf die Zunahme der Treibhausgase. Die Effekte von Wolken auf den globalen Strahlungshaushalt in einem künftigen, sich verändernden Klima stellen eine Herausforderung dar.

Das Ziel dieser Dissertation ist die Verbesserung des Verständnis des Strahlungstransfers in einer bewölkten Atmosphäre. Dafür wird der Effekt von Schichtwolken (stratiformer Bewölkung) auf die kurzwellige Strahlung für Payerne im Schweizerischen Mittelland ermittelt und eine Methode entwickelt, die für lange Zeitreihen operationeller Beobachtungen von atmosphärischen Messstationen angewandt werden kann. Zuerst wird geprüft, mit welcher Genauigkeit Wolkensituationen mit einer einzelnen Wolkenschicht identifiziert werden, und wie gut ihre Ober- und Untergrenze bestimmt werden kann. Dieses Verfahren beruht auf Vergleichen zwischen operationellen Messdaten mittels Fernerkundung und Radiosondenprofilen, und Daten einer Messkampagne (TUC - Temperature hUmidity and Cloud) in Payerne. In einem zweiten Schritt wird unser Verständnis des Strahlungstransfers in klaren (wolkenlosen) Situationen durch Modellsimulationen vertieft. Resultate solcher Strahlungsberechnungen für Situationen mit einer einzelnen Wolkendecke werden mit Messdaten an der Erdoberfläche und an der Obergrenze der Atmosphäre verglichen. Diese Simulationen werden schliesslich dazu verwendet, um die Absorption, Transmission und Reflexion in einzelnen Wolkenschichten zu ermitteln. Parallel dazu wird auch eine empirische Methode angewendet, wobei der Wolkeneffekt ausschliesslich mittels Beobachtungsdaten bestimmt wird.

Das *Baseline Surface Radiation Network* (BSRN) strebt lange Zeitreihen mit präzisen Strahlungsmessungen an und betreibt weltweit 39 Stationen. Eine dieser BSRN Stationen befindet sich an der Aerologischen Station in Payerne und wird durch das Bundesamt für Meteorologie und Klimatologie (MeteoSchweiz) betreut. Die kurz- und langwellig einfallende und reflektierte Strahlung wird seit 1992 gemäss BSRN Richtlinien gemessen, während seit Oktober 2000 auch die Aerosol optische Dicke (AOD) erfasst wird. Beobachtungen der Wolkenbedeckung, Wolkengattung und Höhe der Wolkenuntergrenze werden Tag und Nacht alle 3 Stunden durchgeführt (Synop). Schliesslich werden in Payerne zweimal täglich Ballonsondierungen durchgeführt, mit denen die Temperatur-, Feuchte-, und Druckprofile bis in grosse Höhen ermittelt werden. Zusammen mit weiteren Bodenmessungen vom Standort Payerne und anderen meteorologischen Stationen in der Schweiz bilden diese Daten die Grundlage der hier vorgestellten Studien.

Während der TUC Messkampagne im Winter 2003/2004 waren ein Wolkenradar und ein Ceilometer in Payerne in Betrieb. Eine Methode für die automatische Erkennung der vertikalen Ausdehnung von Nebel und tiefliegenden Stratuswolken wird vorgestellt. Der Ceilometer erwies sich als sehr effizient für die Erkennung von Nebel und der Wolkenuntergrenze (>95% der Fälle). Das Wolkenradar ist noch in der Entwicklungsphase und zeigt eine geringere Zuverlässigkeit (<60%). Ausserdem wird ein Vergleich der Wolkenobergrenze zum einen durch das Wolkenradar, zum anderen mittels Radiosonden durchgeführt. Dabei ergibt sich eine Unterschätzung der Wolkenobergrenze durch das Radar von etwa 50 m.

Über einen Zeitraum von 2001 bis 2005 werden AOD Messungen, Radiosondenprofile und andere meteorologische Beobachtungen für die Simulation einer Anzahl wolkenloser Situationen mit MODTRANTM verwendet. Vergleiche modellierter kurzweiliger Strahlung (*SDR* - shortwave downward radiation) mit BSRN Strahlungsmessungen weisen für die Globalstrahlung eine gute Übereinstimmung innerhalb der Messgenauigkeit auf (<1%). Die Modellsimulationen für die diffuse *SDR* erwiesen sich als schwieriger wobei die lineare Regression zwischen der modellierten und der gemessenen Diffusstrahlung signifikant von ihrer idealen 1 : 1 - Linie abweicht. Nachfolgend werden Hypothesen aufgestellt um diese Unterschiede zu erklären, sowie Vorschläge gemacht, um die Übereinstimmung zwischen modellierter und gemessener diffuser *SDR* zu verbessern. Die Simulationen des Strahlungstransfers für wolkenfreie Situationen ermöglichen die Ermittlung der Güte des Modells MODTRANTM für den Standort Payerne.

Parallel zur deterministischen Methode mit den Modellrechnungen wird auch eine empirische Methode getestet um den Effekt der Wolken auf die Strahlung zu bestimmen. Ein auf kurz- und langwelligen Strahlungsmessungen basierender Algorithmus wird verwendet, um Strahlungsmessungen unter wolkenlosen Bedingungen zu erkennen, sowie die wolkenlose Strahlung in bewölkten Situationen zu schätzen. Eine Kombination der synoptischen Augenbeobachtungen und der BSRN Strahlungsdaten ermöglicht die Bestimmung des Effekts von allen Bewölkungssituationen auf die einfallende kurz- und langwellige Strahlung. Für den Zeitraum von 1998 bis 2003 führen Wolken am Messstandort Payerne zu einer mittleren Reduktion der totalen einfallenden Strahlung um 36 Wm^{-2} . Ausserdem hängt der Effekt der Wolken auf die Strahlung vom Wolkentyp ab.

Basierend auf die zuvor genannten Ergebnisse wird schliesslich eine Methode entwickelt um die Absorption und Reflexion der Sonnenstrahlung innerhalb einer einzelnen Wolken-schicht mit Hilfe von MODTRANTM zu berechnen. Das Clouds and the Earth's Radiant Energy System Experiment liefert einen globalen Datensatz mit Messungen der an der Atmosphärenobergrenze gemessenen reflektierten Strahlung. Die Daten die über der Station Payerne gemessen wurden ermöglichen die Simulation des Strahlungstransfers durch eine einzelne Wolkenschicht, so dass gleichzeitig eine annehmbare Übereinstimmung der modellierten und gemessenen Strahlungsflüsse an der Erdoberfläche und an der Atmosphärenobergrenze erreicht wird. Der Median der Differenzen zwischen dem Modell und den Messungen liegt bei 9% (n=18) an der Atmosphärenobergrenze, der Median für die entsprechenden Differenzen an der Erdoberfläche unter 1%. Der Median des Absorptionsvermögens zwischen der Wolkenunter- und Obergrenze ist 0.22, und die absorbierte Strahlung beträgt ungefähr 28 Wm^{-2} .

Contents

Abstract	iii
Zusammenfassung	v
Abbreviations and Acronyms	xi
1. Introduction	1
1.1 Motivation	1
1.2 Objective and Outline	1
2. Background information	5
2.1 Radiation	5
2.2 Clouds	7
2.3 Observational data	7
2.3.a Radiation observation at PAY BSRN	8
2.3.b Synop Observations	10
2.3.c ANETZ	11
2.3.d Radiosounding	11
2.3.e Ceilometer	12
2.3.f FMCW Cloud radar	12
2.3.g Wind profiler	13
2.3.h Ozone	13
2.3.i Satellite observations	13
2.4 Methods	14
2.4.a MODTRAN TM	14
2.4.b SWFA	14
3. Detection of fog and low cloud boundaries with ground-based remote sensing systems	15
3.1 Introduction	17
3.2 Instrumentation and method	18
3.3 Automatic detection of cloud base and top	21
3.3.a Case studies	21
3.3.b Automatic detection of cloud-base and -top performances during the TUC experiment	25
3.4 Discussion	27
3.5 Summary	30

4. Solar irradiance computations compared with observations at the BSRN Payerne site	33
4.1 Introduction	35
4.2 Data and Instruments	36
4.2.a BSRN shortwave radiation measurements	36
4.2.b Aerosol optical depth	38
4.2.c Human eye observations	38
4.2.d Radiosounding	39
4.3 Clear sky detection	39
4.4 Model and input data	41
4.5 Results	42
4.6 Discussion	44
4.7 Conclusions	48
5. Empirical analysis of cloud effects on surface radiation	51
5.1 Effect of all clouds on surface incoming radiation	51
5.1.a Method	51
5.1.b Results and Discussion	52
5.2 Effect of selected cloud types on surface incoming radiation	54
5.2.a Selection of cloud types	54
5.2.b Results	55
5.3 Conclusion	58
6. Radiation transfer in stratus clouds at the BSRN Payerne site	59
6.1 Introduction	61
6.2 Observation techniques	62
6.2.a Synop	63
6.2.b Radiosounding	63
6.2.c Weather map	63
6.2.d Radiation	63
6.2.e Cloud radar	64
6.2.f Ceilometer	64
6.3 Case selection and cloud boundaries detection	64
6.4 Satellite observations	65
6.5 Radiation Transfer model MODTRAN TM	66
6.6 Results	67
6.6.a Surface radiation	67
6.6.b Top of atmosphere reflected radiation	69
6.6.c Cloud absorbance, transmittance and reflectance	71
6.7 Discussion	74
6.8 Conclusions and Outlook	76
7. Conclusion and Outlook	79
7.1 Summary and conclusions	79
7.1.a Cloud detection	79
7.1.b Clear sky model simulations	80
7.1.c Effect of clouds on incoming radiation	80

7.1.d	Absorbance and radiative transfer in stratus clouds	80
7.2	Outlook	81
A.	Instrumental Details	83
A.1	Ceilometer	83
A.2	FMCW cloud radar	83
B.	Details on the SWFA	85
	References	93
	Acknowledgements	101
	Curriculum Vitae	103

Abbreviations and Acronyms

Abbr./Acro.	Definition
ANETZ	MeteoSwiss automatic network
ARESE	Atmospheric Radiation Measurement Enhanced Shortwave Experiment
ARO	Arosa
AOD	Aerosol Optical Depth
ARBEX	Arctic Radiation Budget Experiment
ARM	Atmospheric Radiation Measurement
asl	Above sea level
ASTEX	Atlantic Stratocumulus Transition Experiment
BSRN	Baseline Surface Radiation Network
CAA	Cloud Absorption Anomaly
CDF	La Chaux-de-Fonds
CERES	Clouds and the Earth's Radiant Energy System
CHARM	Swiss Atmospheric Radiation Monitoring
CLARA	Cloud and Radiation experiment
CRS	Clouds and Radiation Swath
DARR	Delft Atmospheric Research Radar
EOS	Earth Observation System
FMCW	Frequency-Modulated Continuous-Wave
FOV	Field of View
GAW	Global Atmosphere Watch
GCM	Global Circulation Model
BERB	Geostationary Earth Radiation Budget
GMS-5	Geostationary Meteorological Satellite
JFJ	Jungfrauoch
<i>LDR</i>	Longwave Downward Radiation
LOM	Locarno-Monti
<i>LUR</i>	Longwave Upward Radiation
MERIS	Medium-spectral Resolution Imaging Spectrometer
MeteoSwiss	Federal Office of Meteorology and Climatology, Switzerland
MMCR	Millimeter Wave Cloud Radar
MODIS	Moderate Resolution Imaging Spectroradiometer
MODTRAN	MODerate TRANsfer model
MSG	Meteosat Second Generation
NASA	National Aeronautics and Space Administration
NIP	Normal Incidence Pyrheliometer

Abbr./Acro.	Definition
NSA	North Slope Alaska
PAY	Payerne
PFR	Precision Filter Radiometers
PMOD	Physikalisch-Meteorologisches Observatorium Davos
RMSE	Root Mean Squared Error
RTM	Radiative Transfer Model
<i>SDR</i>	Shortwave Downward Radiation
<i>SDR_{diff}^{new}</i>	diffuse <i>SDR</i> observations with new shading system
<i>SDR_{diff}^{old}</i>	diffuse <i>SDR</i> observations with old shading system
SEVIRI	Spinning Enhanced Visible and Infrared Imager
SGP	Southern Great Plains
SIRTA	Site Instrumental de Recherche par Télédétection Atmosphérique
<i>SNR</i>	Shortwave Net Radiation
<i>SUR</i>	Shortwave Upward Radiation (reflected)
<i>SUR_{toa}</i>	Shortwave Upward Radiation at Top of Atmosphere
SWFA	Shortwave Flux Analysis
Synop	Human eye observations
SZA	Solar Zenith Angle
TOA	Top of Atmosphere
TUC	Temperature, hUmidity and Cloud
WCRP	World Climate Research Program
WMO	World Meteorological Organisation
WPR	Wind Profiler
WRC	World Radiation Centre

Chapter 1

Introduction

1.1 Motivation

Earth, seen from space, is a blue planet marked by stark white cloud structures that distinguish it from other planets. Clouds have an enormous impact on Earth's weather and climate. They reflect sunlight, block outgoing longwave radiation, and produce precipitation. Clouds act as strong modulator on the radiative energy exchange at the upper and lower boundaries of the atmosphere. They represent the most important variable in determining the amount of solar energy absorbed in the atmosphere as well as the amount of infrared energy radiated to space.

Effects of clouds remain a major source of uncertainty in the simulation of climate changes (e.g., aerosol indirect effect, cloud lifetime effect, response of cloud cover to increasing greenhouse gases, Trenberth et al., 2007). Therefore an important question is raised: What will be the effect of clouds in a future climate change? In a global average, clouds tend to have a cooling effect on climate (Somerville et al., 2007). Many efforts have been made to figure out the effects of clouds on the global radiation (e.g., Arking, 1991 and Cess et al., 1995). This thesis presents methods, studies and results that help improving the knowledge of the effect of stratiform clouds on the radiation transfer in the atmosphere.

1.2 Objective and Outline

At the Federal Office of Meteorology and Climatology (MeteoSwiss) at Payerne, Switzerland, numerous climate observations are performed operationally. Longterm cloud observations and radiation measurements, as well as radiosoundings allow detailed studies of the radiation budget under different weather conditions.

Improving the knowledge of the effects of clouds on radiation requires several types of information on the state of the atmosphere, as well as radiative transfer modeling. Our strategy for fulfilling our general goal of improving knowledge of the cloud effect on radiation is:

1. to simulate simple and well-defined cases involving full cloud coverage with stratified clouds
2. to match radiation observation at the ground and top of atmosphere, and

3. to deduce the cloud optical properties from it.

The simulation input should be inferred from measurements as much as possible. Particularly, the different atmospheric profiles are obtained from radiosounding. Similarly, the exact location of the cloud must be known and, if available, additional microphysical information on the cloud. In this study we used a large variety of the observations performed at MeteoSwiss Payerne. Besides operational observations and measurements, data from experimental campaign studies were available. However, some important information on cloud microphysical properties were still not measured. Therefore, one challenge of this study was to define and test methods to detect and precisely define cloud situations and cloud properties with the observations available. The goals of the thesis presented here are:

- Determine cloud boundaries using operational measurements
- Determine cloud boundaries for well-defined cloud situations with the help of an experimental intensive campaign study data set, and verify cloud boundaries determined with operational measurements
- Test the capabilities of the radiation transfer model (RTM) MODTRANTM for clear sky situations
- Calculate the effect of different stratiform clouds on the incoming surface radiation using an empirical method
- Simulate the radiation interaction with cloud using the RTM MODTRANTM for the cloud situations described previously
- Deduce information such as the absorbance and transmittance of stratiform clouds from the model calculations

In the next chapter, background information is provided about the earth's radiation budget, and clouds. The Payerne site and the data used in this thesis are also described therein. Each type of measurements used for this study is briefly explained, and some details on the methods are given.

Chapter 3 presents a method for detecting and defining cloud boundaries of low clouds. During the Temperature humidity and Cloud (TUC) experiment, which took place in Payerne during winter 2003/2004, several profiling instruments including a ceilometer and cloud radar were operated at the Payerne site. Within 3 months of observation several cases of low clouds and fog could be detected and analyzed with help of synoptic observations and radiosounding profiles (temperature, humidity). The reliability and performance of the presented methods are tested.

Before performing radiative transfer model simulations for stratus cloud situations, clear sky situations were simulated in order to verify the performance of the model in this simpler situation. Model calculations for cloud free conditions are presented in Chapter 4. The aim of these analyses is to evaluate the capability of reproducing cloud free radiation observations using MODTRANTM for well-defined clear sky cases. Ancillary atmospheric

data from the aerological station is used as model input and the results are tested against high quality radiation observations at the surface.

The net surface cloud effect was estimated for different types of clouds using an empirical analysis (Chapter 5). The effect on longwave and shortwave downward radiation is calculated using human eye observations, radiation observations and an algorithm to estimate clear sky radiation (Long and Ackerman, 2000). This allows determining the cloud effect on incoming radiation with a more detailed analysis depending on the cloud type. It also facilitates the choice of the cloud type which is analyzed with RTM MODTRANTM for its effect on shortwave downward radiation in the following chapter.

After the empirical analysis of the previous chapter, a theoretically-based method is applied to determine cloud effects on solar radiation. MODTRANTM being set up for the site of Payerne, solar irradiance at the surface for well-defined stratus cloud cases can be simulated. The aim of the analyses presented in Chapter 6 is to estimate the absorption and transmittance of solar radiation in single layered stratiform clouds at the Payerne site.

Chapter 2

Background information

The aim of this Chapter is to give a limited theoretical introduction to radiation and clouds, and brief information on the observation techniques used for the study. Finally, a short introduction to the two most used methods in this study is given.

2.1 Radiation

The energy budget at the surface is defined by the following equation:

$$SDR - SUR + LDR - LUR - SH - LH - GF = 0 \quad (2.1)$$

where SDR represents the shortwave downward radiation, SUR is the reflected shortwave radiation at the surface, LDR the longwave downward radiation and LUR the emitted longwave upward radiation. SH and LH stand for sensible and latent heat respectively, and GF is the ground flux. Equation 2.1 defines an equilibrium, therefore at the top of atmosphere (TOA), an equilibrium should also be present, and the same amount of energy is reflected (SUR_{TOA}) and emitted (LUR_{TOA}) by the earth-atmosphere system as is received at the top of atmosphere (SDR_{TOA}):

$$SDR_{toa} - SUR_{toa} - LUR_{toa} = 0 \quad (2.2)$$

In Figure 2.1 this equilibrium is represented including the global mean radiation fluxes as found by Kiehl and Trenberth (1997). A part (about 31%) of the incoming mean global solar radiation is reflected by clouds, aerosol, and atmospheric gases, the other part is emitted as outgoing terrestrial (longwave) radiation.

In this study we focus on shortwave fluxes (broadband solar radiation ranging from 0.3 - 4.0 μm). This also corresponds to the bandwidth covered by the instruments at the Baseline Surface Radiation Network (BSRN) to measure direct, diffuse and global SDR .

On its path through the atmosphere, SDR is scattered, reflected and absorbed by molecules (e.g., H_2O , NO_2 , O_3) and particles (aerosols). Rayleigh scattering includes only scattering by the permanent atmospheric gases, and excludes the effects of water vapor, clouds, and aerosols. The scattering by aerosols and clouds is best described by the theory of Mie and geometrical scattering depending on their size.

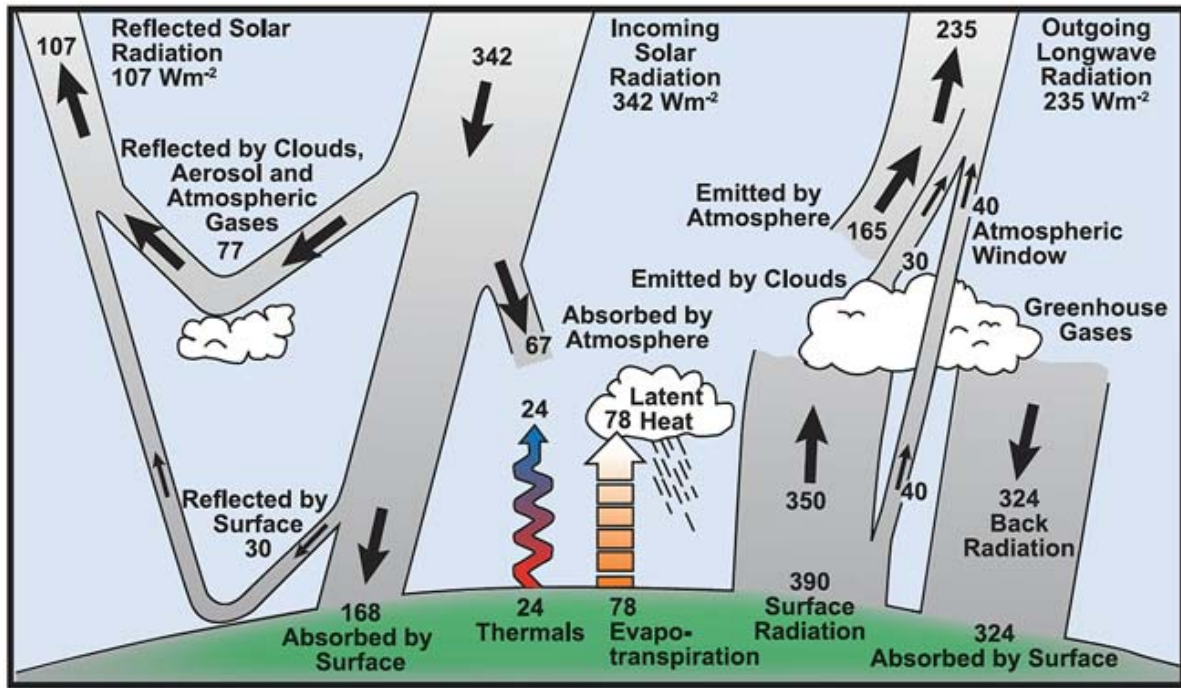


FIG. 2.1: The earth's annual global mean energy budget based on Kiehl and Trenberth (1997).

A part of the *SDR* is absorbed by atmospheric gas, molecules and aerosols. The amount of solar irradiance absorbed depends on the solar elevation and the atmospheric composition. Most of the absorption of the solar irradiance in the range analyzed in this study is due to water vapor. Here special regard is given to absorption in clouds. The *SDR* amount absorbed in clouds depends on the cloud extent, droplet size and number distribution, and the cloud water or ice content. Absorption within the cloud is mainly due to molecular absorption between the cloud particles, the cloud particles however enhance absorption by increasing the optical path lengths of radiation due to scattering.

Finally, an important part of the incident solar irradiance is reflected back to space. The ratio between the light reaching the surface or cloud top and the light reflected back to space is specified as albedo. Lowest albedo can be found on water surface (~ 0.1), highest albedo is observed on clouds and fresh snow (~ 0.9).

Cloud absorption has caused numerous studies and long discussions with emphasis on a specific issue. Many studies indicated that clouds absorb about three times (25 to 35 Wm^{-2}) as much solar radiation as theory and radiative transfer models (RTM) predict (Quante, 2004). The so called cloud absorption anomaly (CAA, Li et al., 1999) is the origin of intensive measurement campaigns such as ARESE (Atmospheric Radiation Measurement Enhanced Shortwave Experiment) with the aim on determining the reasons for the systematic underestimation of the cloud absorption by the models (Valero et al., 2000). Finally, Li (2004) demonstrated that CAA was largely an artifact (see also Chapter 6).

2.2 Clouds

Clouds cover large part of the globe ($\sim 60\%$, Heymsfield, 1993) and strongly influence the evolution of climate.

TABLE 2.1: Classification of clouds corresponding to their height and latitude. According to WMO International Cloud Atlas, 1956. For low clouds the height indicated is valid above the ground, for middle and high clouds above the mean sea level.

Cloud level	Cloud types	Polar regions	Midlatitudes	Tropical regions
High	Ci, Cc, Cs	3 - 8 km	5 - 13 km	6 - 18 km
Middle	As, Sc, Ns	2 - 4 km	2 - 7 km	2 - 8 km
Low	Cu, St, Sc, Cb	0 - 2 km agl	0 - 2 km agl	0 - 2 km agl

Three cloud levels (low, middle, and high) and 10 main cloud types are distinguished (see Table 2.1) depending on their location (e.g., altitude) and characteristics (e.g., shape). The two low-level clouds stratus (St), and stratocumulus (Sc) contain water droplets only (water clouds) and have an upper boundary below approximately 2 km above ground level (agl). If the cloud base touches the ground and visibility is < 1 km we speak of fog. The cloud-top height of cumulus (Cu) and cumulonimbus (Cb) can overlap into the middle and high level and may contain water droplets and ice particles (mixed-phase clouds). Middle level clouds altostratus (As), altocumulus (Ac) and nimbostratus (Ns) are often mixed phase clouds as well. High level clouds contain ice particles only and are called cirrus (Ci), cirrocumulus (Cc), and cirrostratus (Cs).

Clouds cover approximately 60% of the earth's surface (Heymsfield, 1993). They have a strong influence on the global energy budget: They affect the amount of solar radiation absorbed by the earth and partition this energy between the atmosphere and the earth's surface. They affect the energy loss of infrared radiation to space by re-emitting it to the surface.

In this study the stratiform single layered low cloud type stratus nebulosus is selected for analyses of the cloud boundary detection and the effect of clouds on radiation. Figure 2.2 shows the upper boundary of a stratus nebulosus over the Swiss Plateau. Stratus is a water cloud, containing no ice particles and often observed in combination with high pressure situation over Switzerland (Hack, 2006; Schüepf, 1979).

2.3 Observational data

The research performed within the framework of this thesis needed various observations and measurements. The contents of Chapters 3, 4, and 6 are taken from two manuscripts published in refereed journals and one submitted manuscript. Therefore some of the data and techniques are described redundantly in the different chapters. When this is the case, it will be mentioned in this chapter by referring to the corresponding chapter. The author does apologize for such repetitions, which may annoy the reader.



FIG. 2.2: A stratus nebulosus seen from the top of Gurnigel in the Bernese foothills of the Alps. The well-defined cloud top and clear sky above the stratus are typical weather features for high pressure conditions during winter (Photo: D. Nowak, 2006)

The aerological station of the Federal Office of Meteorology and Climatology (MeteoSwiss), at Payerne (PAY, 46.812°N, 6.942°E, 491 m asl) is located in the Swiss Plateau, a relatively flat region between the Jura Mountains to the north-northwest (1000–1600 m asl) and the Alps to the south-southeast (2000–4500 m asl). Most of the data and observations used in this study are retrieved at the PAY station. However some measurements from other stations were used for cloud cover and other information. The surface observations made at the Jungfrauoch (JFJ, 46.547°N, 7.985°E, 3580 m asl) and La Chaux-de-Fonds (CDF, 47.083°N, 6.792°E, 1019 m asl) were used for the detection of stratus situations, and ozone measurements from Arosa (ARO, 46.779°N, 9.675°E, 1840 m asl) as a model input. The location of these stations is showed in Figure 2.3. These stations and their location will be mentioned again in Chapters 3, 4, and 6.

2.3.a Radiation observation at PAY BSRN

The Swiss Atmospheric Radiation Monitoring program (CHARM) has been established to provide measurements allowing the monitoring of atmospheric radiation transfer in Switzerland. It is part of the Swiss contribution to international efforts coordinated by the World Meteorological Organization (WMO). Such efforts include the Global Atmosphere Watch (GAW) that monitors longterm evolution of the atmosphere on global and regional scale to assess contributions to climate change, and the BSRN, a project of the World Climate Research Programme (WCRP) aimed at detecting changes in the earth's radiation balance, which may cause climate changes.

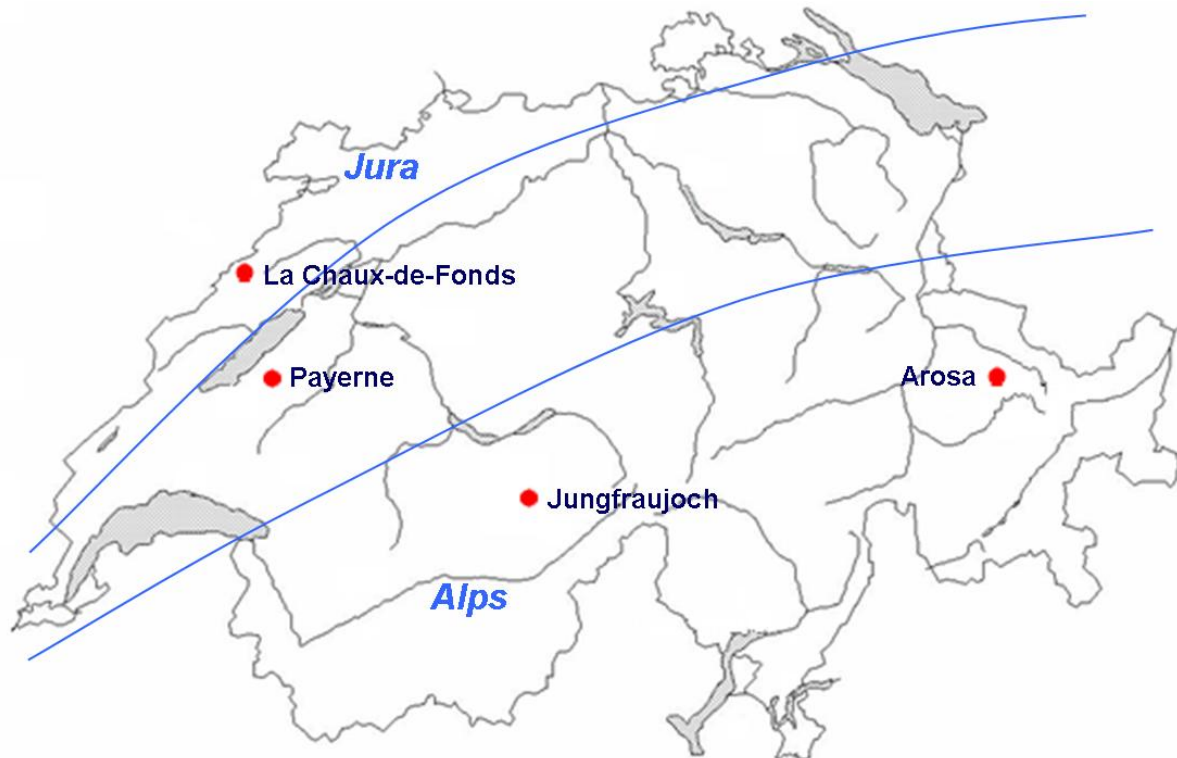


FIG. 2.3: Map of Switzerland with the meteorological station Payerne, and the three auxiliary stations Jungfrauoch, La Chaux-de-Fonds, and Arosa.

The objective of the BSRN (Ohmura et al., 1998) is to provide observations of short and longwave surface radiation fluxes of the best possible quality, using a high sampling rate. More details about BSRN can be found in Chapter 4. MeteoSwiss operates four CHARM stations monitoring radiation at the ground from the ultraviolet (UV) to the visible and infrared (IR) part of the spectrum. Two stations are located in the Swiss Alps and two stations are located in the plains, one of which is also the PAY BSRN station.

Shortwave downward radiation

High accuracy radiation measurements are available at the PAY BSRN station. The direct SDR measurements are performed with a Kipp & Zonen pyrliometer CH1 NIP (Normal Incidence Pyrliometer) since 1 January 1995. The instrument mounted on a sun tracker points to the sun (Figure 2.4). The solar spectrum is measured from 0.2 to 4.0 μm with a narrow viewing angle. The diffuse and global SDR are measured with a shaded and unshaded Kipp & Zonen CM21 pyranometer respectively. The bench with the shaded instruments for the diffuse SDR and the LDR observations performed at BSRN PAY site is shown in Figure 2.5. This shading system will be designed in later chapter (4.2.a) as $SDR_{dif_{old}}$. A new shading system has been introduced in July 2002 (Figure 2.6) which permits better sun tracking and has shading disks adjusted to the size of the sensors. See also Chapter 4 for further information.

The CM21 pyranometers integrate hemispherically over a horizontal receiver surface, and



FIG. 2.4: PFR, CH1 NIP and shaded Kipp & Zonen CM21 Pyranometer mounted on a BRUSAG sun tracking instrument

cover a spectral band from 0.305 to 2.8 μm (50% points) or 0.335 to 2.20 μm (95% points). The measurements of direct, diffuse and global *SDR* are performed at 1 Hz interval, however only 1-minute mean values are stored in the database, as well as the minimum, maximum value and the standard deviation. The pyranometers for the diffuse and global *SDR* measurements are ventilated and heated. See Chapter 4.2.a for more details and the accuracy estimation of these observations.

Aerosol optical depth

Aerosol optical depth (AOD) is related to the turbidity of the atmosphere and observed within the Swiss Atmospheric Radiation Monitoring (CHARM) network at 4 stations (PAY, Locarno Monti, Davos and JFJ). Measurements of the AOD are performed with Precision Filter Radiometers (PFR - Wehrli, 2000) at different wavelengths. At PAY, the measurements started in October 2000 at 4 wavelengths (368 - 862 nm). Since July 2002 the PFR data set includes measurements at 16 wavelengths (305 - 1024 nm) enabling the determination of the AOD at 9 wavelengths and of the integrated water vapor (IWV). The field of view is 2.5° and has a slope of 0.7° . More details are given in Chapter 4.

2.3.b Synop Observations

Observation of cloud cover, type and base height are reported for the three main cloud levels (low, middle, high clouds) as well as the ground visibility (Müller, 1982). These synoptic observations are performed every 3 hours, starting at 0 UTC. Despite their subjective character and variations from one observer to another these observations are very important for climatologists and meteorologists (Dai et al., 2006). For this study



FIG. 2.5: BSRN PAY bench with diffuse *SDR* and *LDR* observation system (operative since October 1992).

they are used for verifying the presence or absence of low clouds or fog (chapter 3), and to detect situations with specific cloud types (chapters 5 and 6). See especially chapter 3.2 for details.

2.3.c ANETZ

The aerological station of PAY also includes an ANETZ (automatic weather observation network) station. Meteorological parameters (defined by WMO) are measured (e.g., wind speed and direction, sunshine duration). In this study, air temperature, relative humidity, and atmospheric pressure are used from this station e.g. for the model input files (Chapters 4 and 6).

2.3.d Radiosounding

At the PAY station balloon-borne meteorological radiosoundings including pressure, temperature and humidity profiling are performed twice a day at 12 and 00 UTC. They are launched at 11 and 23 UTC respectively. Radiosondes are launched an hour before the officially reported time, in order to account for the balloon ascent. The temperature and humidity profiles are used to determine the cloud-top height (Chapter 3), and the profiles are implemented in the radiation transfer model (RTM) MODTRANTM input files for the radiation simulation (Chapter 4). See also these chapters for more instrument details.



FIG. 2.6: New diffuse *SDR* and *LDR* observation system at the BSRN PAY site (operative since July 2002).

2.3.e Ceilometer

A Vaisala ceilometer CT25K was operated from 15 November 2003 until 31 August 2004 at PAY. It can detect up to three cloud layers simultaneously and retrieve cloud heights every 30 s with a vertical resolution of 15 m up to 7.5 km above the ground. It was used to determine the cloud-base height using the measured vertical visibility. See Chapter 3 and Table 3.1 for further information on the ceilometer CT25K, and also Appendix A.1 for some technical details. After the ceilometer operated at the PAY station was moved to another observation site, ceilometer information from the same type of instrument could be obtained from the nearby military airport.

2.3.f FMCW Cloud radar

A 78-GHz FMCW cloud radar, designed at the Rutherford Appleton Laboratory, was operated at PAY during three winter months (2003/2004) in the context of the Temperature hUmidity and Clouds (TUC, Chapter 3) experiment to detect cloud boundaries. For the present study, it was used to detect the cloud-top height for low clouds and fog. Backscatter information is retrieved at a time interval of 30 s. It is sensitive to clouds and precipitation and was set up to measure up to 8 km above the ground with a vertical resolution of about 15 m. Again, further information can be found in Chapter 3, Table 3.1 and in Appendix A.2

An example for the use of the FMCW cloud radar and the ceilometer CT25K is given in Figure 2.7. It shows the time series of both instruments for day with alternating low cloud cover and fog on a winter day at PAY.

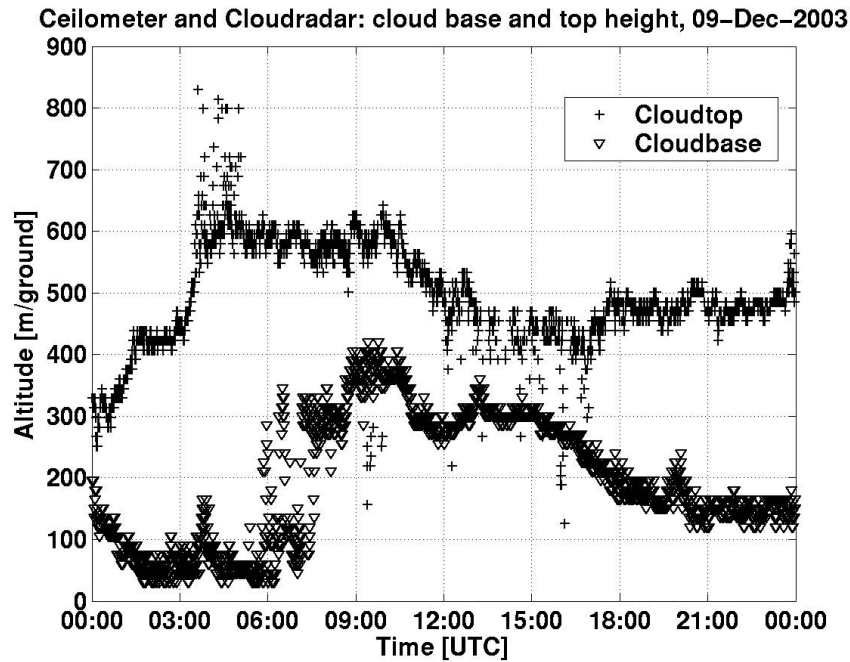


FIG. 2.7: Cloud base and cloud top retrieved with ceilometer and cloud radar 9 December 2003 at the PAY site. Example of an overcast day with low stratus nebulosus and fog alternating.

2.3.g Wind profiler

The wind profiler (WPR) is used to observe the vertical profile of wind direction and velocity. It sends a signal at 1290 MHz when operated at low mode, the vertical resolution is 42 m, the first layer of detection is at 158 m and the maximum height range is 1489 m. In this study the WPR is used to retrieve information on the cloud upper boundaries. See Chapter 3 for further information about the information retrieved for this study and for Figures.

2.3.h Ozone

Total ozone column is measured at Arosa with a Dobson spectrophotometer (Stähelin et al., 1998). Data from PAY (radiosondes) are then used to add the difference of the ozone column between the altitude of PAY (lower) and ARO. When data is missing, a linear interpolation in time is made to estimate the total ozone column. In this study, ozone values are implemented in the RTM MODTRANTM input files used for the studies described in Chapters 4 and 6.

2.3.i Satellite observations

For the top of atmosphere (TOA) shortwave flux comparisons and cloud situation verifications different satellite products were used and are described later (Chapter 6.4).

The Clouds and the Earth's Radiant Energy System (CERES) products including reflected shortwave and emitted longwave radiation are available for the period of December

2000 to December 2005 (Wielicki et al., 1996). Cloud properties (cloud fraction, type etc) given by the CERES data set are from the Moderate Resolution Imaging Spectroradiometer (MODIS).

Since February 2004 data is available from the Geostationary Earth Radiation Budget (GERB) project (Harries et al., 2005). GERB is a highly accurate, visible-infrared broadband radiometer and measures the reflected solar and emitted thermal radiation from the earth. For few cases in this study, GERB data are used for additional information.

Some of the cloud situations presented in Chapter 5 coincide with observations of the medium-spectral resolution imaging spectrometer (MERIS), which were available for verification of the cloud type and cloud albedo (Fischer et al., 2000a,b).

2.4 Methods

In the following paragraphs two algorithms are briefly introduced. They are presented in more detail in later Chapters including the content of paper manuscripts.

2.4.a MODTRANTM

The MODerate resolution TRANsmittance (MODTRANTM) code calculates atmospheric transmittance and radiance. MODTRANTM is a state of the art 1-dimensional RTM to calculate radiation transfer for shortwave global, direct, diffuse and longwave radiation at the Earth's surface or any other point in the atmosphere from the UV (0.2 μm) to the thermal infrared ($>100 \mu\text{m}$) spectra. See chapter 4 and 6 for details about the input data used to run the model for clear and cloudy sky situations. The MODTRAN4v3r1TM used for the calculations presented in chapter 4 was later replaced with a more recent version, MODTRAN5v2r11TM, which was used in Chapter 6 for the simulation of the well-defined stratus cloud situations. Some important improvements in the latter MODTRAN5v2r11TM version concern aerosol details (Ångström law, aerosol properties) and model simulations for thick cloud situations. For our studies the change to a newer MODTRANTM version was decided during the revision of the paper presented in Chapter 4. It had no significant effect on the results presented in Chapter 4.

2.4.b SWFA

The shortwave flux analysis (SWFA) code of Long and Ackerman (2000) is an algorithm to identify periods of clear skies using 1-minute measurements of surface broadband total and diffuse *SDR*. The clear-sky detection algorithm uses a sequence of tests that eliminates almost all periods when clouds are present in the hemispheric field of view (FOV) of the instruments. These are described in detail by Long and Ackerman (2000) and a summary of the tests for clear sky detection described in the mentioned paper are given in appendix B.

Chapter 3

Detection of fog and low cloud boundaries with ground-based remote sensing systems

Daniela Nowak¹, Dominique Ruffieux², Judith L. Agnew³, and Laurent Vuilleumier²

Published in *Journal of Atmospheric and Oceanic Technologies*, 25 (8), 1357-1368, 2008, [doi:10.1175/2007JTECHA950.1]

This Chapter presents different techniques to detect clouds and select cloud situations. Multiple methods and instruments are combined to gain detailed information on the cloud cover and the cloud vertical extent. Some of these techniques were available only for a short period (experimental campaign) and some other for long term monitoring.

Data of a cloud radar and a ceilometer are used to define cloud base and top height for stratus and fog situations. Together with the analysis of radiosounding data and synop observations this chapter represents the basis for defining the appropriate methods for cloud boundaries detection for the later MODTRANTM simulations.

ABSTRACT

The performance of the boundary determination of fog and low stratiform cloud layers with data from a frequency modulated continuous-wave (FMCW) cloud radar and a Vaisala ceilometer is assessed. During wintertime stable episodes, fog and low stratiform cloud layers often occur in the Swiss Plateau, where the aerological station of Payerne,

¹Institute for Atmospheric and Climate Science, ETH Zurich, Switzerland

²Federal Office of Meteorology and Climatology MeteoSwiss, Payerne, Switzerland

³STFC Rutherford Appleton Laboratory, Chilton, Didcot, UK

Switzerland, is located. During the international COST 720 Temperature, hUmidity and Cloud (TUC) profiling experiment in winter 2003/04, both a cloud radar and a ceilometer were operated in parallel, among other profiling instruments. Human eye observations ("synops") and temperature and humidity profiles from radiosoundings were used as reference for the validation. In addition, two case studies were chosen to demonstrate the possibilities and limitations of such ground-based remote sensing systems in determining low clouds. In these case studies the cloud boundaries determined by ceilometer and cloud radar were furthermore compared with wind profiler signal-to-noise ratio time series. Under dry conditions, cloud-base and -top detection was possible in 59% and 69% of the cases for low stratus clouds and fog situations, respectively. When cases with any form of precipitation were included, performances were reduced with detection rates of 41% and 63%, respectively. The combination of ceilometer and cloud radar has the potential for providing the base and top of a cloud layer with optimal efficiency in the continuous operational mode. The cloud-top height determination by the cloud radar was compared with cloud-top heights detected using radiosounding humidity profiles. The average height difference between the radiosounding and cloud radar determination of the cloud upper boundary is 53 ± 32 m.

3.1 Introduction

Precise forecasting of the formation, evolution, and erosion of fog and low stratus is a major challenge for meteorology, especially in complex topography. One of the goals of the COST 720 Temperature, hUmidity and Cloud (TUC) winter experiment undertaken in Switzerland in 2003/04 (Ruffieux et al., 2006) was to provide a dataset for determining the base and top of low clouds using a simple combination of ground-based remote sensing instruments.

Frequent and detailed information about the meteorological conditions are important for weather forecasters, climate studies, and aviation control. One of the high priority duties of observers is the description of the evolution of clouds, especially within the planetary boundary layer. However, automatic weather reports are becoming important because human observations are becoming more difficult to organize, especially during nighttime (Aviolat et al., 1998). The cloud amount (sky coverage in octas) can be automatically estimated using for example incoming longwave radiation and surface parameters (Dürr and Philipona, 2004). However, this method does not include information on cloud-base and -top height, and such measurements are crucial for a variety of applications. Cloud-base and -top heights are important in order to describe the impact of clouds in a changing climate (Ramanathan et al., 1989), and there is a general need for improvement of automatic cloud observation at weather stations and continuous cloud description for climatological issues. For aviation and traffic, such systems improve the detection of fog and low stratus, but the prediction of their appearance and dispersion is still an ongoing challenge. High-resolution observations of the cloud and fog boundaries can help modelers verify and improve local fog prediction models, numerical weather prediction models or climate models (e.g., the Baltex Bridge Campaign: Crewell and co authors, 2004). In response to such demands, longterm and high-resolution cloud-base and -top height measurements are performed at some meteorological stations [e.g., at Chilbolton Observatory (United Kingdom), at the Site Instrumental de Recherche par Télédétection Atmosphérique (SIRTA) in Palaiseau (France), and in Cabauw (Netherlands), where longterm cloud measurement schemes were developed as part of the Cloudnet project (Illingworth et al., 2007)].

During wintertime stable episodes, fog and low stratiform cloud layers often occur over the Swiss Plateau, a relatively flat region between the Jura Mountains to the north-northwest (1000–1500 m asl) and the Alps to the south-southeast (2000–2400 m asl). The aerological station of Payerne, Switzerland, is located in this area, and was the site of the international COST 720 TUC profiling experiment (Ruffieux et al., 2006). This experiment, which took place during three months in winter 2003/04, was mainly designed to test ground-based temperature and humidity profiling systems and cloud detection instruments. Among other instruments, a Vaisala CT25K ceilometer and a 78-GHz frequencymodulated continuous-wave (FMCW) cloud radar were installed and operated at the measurement site from mid-November 2003 to mid-February 2004.

In this paper a method to determine fog and low stratiform cloud layers from cloud radar and ceilometer data is described. The efficacy of the combination of the two systems during the winter 3-month period is assessed. In section 3.2 the instruments and the method of the determination of cloud or fog base and top are described as well as

the data used for validation of the results (human eye observations, radiosoundings, and, as an additional confirmation, wind profiler data). In section 3.3, the performance of the method is assessed first with the help of two selected cases and then over the entire campaign. Section 3.4 presents a discussion of the performance of the studied remote sensing instruments for low cloud and fog detection and compares our results with previous studies. Our concluding remarks are given in section 3.5.

3.2 Instrumentation and method

The aerological station of Payerne is an official World Meteorological Organization (WMO) site for synoptic weather observations, including cloud information, which are performed every 3 h, starting at 00 UTC. It is also a site for balloon-borne meteorological radiosoundings including pressure, temperature and humidity profiling twice a day at 12 and 00 UTC (launched at 11 and 23 UTC respectively). (Radiosondes are launched an hour before the officially reported time, in order to account for the balloon ascent. In the rest of the paper the official time will be reported, but comparison will be made with the data measured at launching time.) In addition, a wind profiler is operated continuously. During the TUC campaign, several additional radiosoundings were performed with different types of radiosonde. A large set of additional remote sensing instruments were operated, including a ceilometer, a cloud radar, as well as microwave radiometers profiling temperature and humidity, and other instruments. The ceilometer and cloud radar were used in combination for the detection of fog and stratiform low clouds, and for determining their lower and upper boundaries. To estimate the detection efficiency, human eye observations were used as a reference. The determination of the upper boundary by the cloud radar was compared with a determination using radiosounding humidity profiles according to Wang et al. (1999). Technical details of the observation techniques used for this study are listed in Table 3.1 and described more precisely below.

Cloud-base height was determined with a commercially available Vaisala ceilometer CT25K, using the measured vertical visibility. This light detection and ranging (lidar) system sends out short, powerful laser pulses (905 nm) in the vertical direction. The reflection of light (backscatter) caused by aerosol, fog, mist, clouds, or precipitation is measured as the laser pulses traverse the atmosphere. The resulting backscatter profile (signal strength versus height) is processed to detect cloud-base height. The ceilometer can detect up to three cloud layers simultaneously and retrieve cloud heights every 30 s with a vertical resolution of 15 m up to 7.5 km above the ground. The minimum vertical visibility that can be measured is 15 m (e.g., in case of fog). A disadvantage of this system is that high cirrus clouds can hardly be detected because they often occur above 7.5 km. This kind of system is widely used to detect cloud-base heights and cloud cover (e.g., at airports or within climate studies such as stratocumulus research in the southeast Pacific: Kollias et al., 2004).

The 78-GHz FMCW cloud radar, designed at the Rutherford Appleton Laboratory, retrieves backscatter information at a time interval of 30 s. It is sensitive to clouds and precipitation and was set up to measure up to 8 km above the ground with a vertical resolution of about 15 m. The FMCW radar has a transmitter power of approximately

TABLE 3.1: Observation techniques and instruments used for the study, operational at the meteorological station in Payerne, Switzerland (synop, radiosondes, wind profiler) and experimental for the TUC campaign (ceilometer, cloud radar).

Observation technique	Parameter	Time		Height	Lower limit	Upper limit	FOV	Manufacturer
		Res.	Res.					
Synop	Cloud amount type, height visibility	3 h	30 m for low level clouds	30 m for ground limit	21 km	180°	Müller (1982)	
FMCW cloud radar	Cloud top height	30 s	15 m	50 m	8 km	0.8°	Rutherford Appleton Laboratory; UK	
CT25K Ceilometer	Cloud base height	30 s	15 m	15 m	7.57 km	~0.6 mrad	Vaisala Finland	
Radiosondes SRS 400, Snow White, RS80 A	Temperature humidity, pressure	12 h	~15 m	20-30 m	34-35 km	Vertical profile	Meteoloabor AG, Switzerland	
LAP3000 1290MHz wind profiler	Signal to noise ratio	30 s	42 m	158 m	1489 m	6°	Vaisala, Finland Vaisala, Finland Neff (1990)	

120 mW. It transmits at a frequency of 78.2 GHz with a frequency modulation of approximately 10 MHz over a period of approximately 770 μ s. In general cloud radars use two basic types of transmission: pulsed or FMCW. The most important benefit of the FMCW system in this application is that it can make measurements at a shorter range than pulsed systems, which are typically only measuring above 150 m. For the system operated in Payerne during TUC campaign, the lowest detected cloud-top height is 65 m and the minimum range for the detection of mist or fog is about 50 m above the radar. The radar was calibrated at the Chilbolton Observatory, United Kingdom, alongside the pulsed 35-GHz Copernicus cloud radar. The results from this calibration indicate that the sensitivity of the 78-GHz FMCW cloud radar is comparable to that of a modern pulsed cloud radar (Nash et al., 2005). It is still better to use a ceilometer to detect the cloud base of fog and low clouds, because such instruments are more efficient and precise for this task (Clothiaux et al., 2000). With a FMCW system, the vertical resolution is controlled by the quality of the system phase noise, the continuous-wave slew rate, and the sampling speed of the detected signal, while fast Fourier transform effects tend to place a limit on the minimum detection height. For a pulsed system the minimum height is predominantly determined by the length of the transmitted pulse, with no measurements possible below a height equivalent to the pulse duration. FMCW radars are also simpler and cheaper than pulsed cloud radars, the cost of a pulsed system being partly driven by the magnetron which needs replacement after few thousand hours of operation.

A simple empirical method was applied to retrieve cloud-top height from the cloud radar (Ruffieux et al., 2006). An automatic search for the cloud-top signal level within a specified range was performed on each vertical profile recorded by the FMCW cloud radar. Provided the maximum signal in a profile was higher than a threshold value (indicating the presence of cloud), the height of the maximum radar reflectivity was registered. A second threshold value was specified for determining the cloud top. The height at which the reflectivity decreased below this second threshold value was taken as the cloud top. The current configuration allowed the detection of the upper boundary for one cloud layer only.

Human eye observations ("synop") were used to estimate the efficiency of cloud detection by the ceilometer and cloud radar combination. Cloud cover, type, and base height are reported for the three main cloud levels (low, middle, and high clouds) as well as the ground visibility (Müller, 1982). These human eye observations are generally of excellent quality and give regular and important information to meteorologists about the state of the sky, the meteorological conditions (fog, snow, rain, etc.), and the visibility. A known limitation is the restriction to the lowest cloud layer in the case of multilayer clouds with full sky coverage of the lowest layer. In addition, observations are difficult to perform during nighttime; they remain subjective and may vary from one observer to another. However, such observations are extremely reliable for verifying the presence or absence of low clouds or fog.

For our study, fog situations were defined as either fog being reported or mist with a code 9 for the parameter "total cloud cover" (sky not visible because of fog, snow, or other meteorological phenomenon). Situations with fog or stratus clouds in combination with other clouds or more than one cloud layer were discarded and just low-level stratus and fog situations with total sky coverage (8 octas) were selected. This allowed testing of

the automatic detection of fog or stratus boundaries with the ceilometer and cloud radar in simple and clearly identified cases.

Three different radiosondes were used for humidity and temperature profiling during the TUC campaign. Operational radiosoundings were performed with the SRS 400 (Richner, 1999; Ruffieux et al., 2006). In addition, radiosoundings with the Snow White hygrometer (Miloshevic et al., 2006) were available for some of the studied cloudy situations, and one case was detected concurrently with a sounding using the Vaisala RS80A (Verver et al., 2006). The radiosoundings include measurements of the temperature and relative humidity from the ground to about 35 km (relative humidity profiles up to 12 km). The vertical resolution in the lower atmosphere is about 15 m (Table 3.1). Cloud layers were identified as regions with a relative humidity above a given threshold. Cloud upper boundaries were determined by finding sudden negative relative humidity jumps (hydrolapse; Wang et al. 1999). The thresholds chosen for this study depend on the radiosondes used for the profile, the minimum being 93% for the SRS 400.

Studies on specific cases also used information from wind profiler signal-to-noise ratio (Gossard et al., 1982) time series measured concurrently. The wind profiler is used to observe the vertical profile of wind direction and velocity. It sends a signal at 1290 MHz when operated at low mode, the vertical resolution is 42 m, the first layer of detection is at 158 m, and the maximum height range is 1489 m AGL. Information on the cloud upper boundaries can be derived from the wind profiler signal because of the strong gradients at the cloud top: the backscattered signal from the wind profilers is directly proportional to the refractive-index structure function parameter C_n^2 , and there is a close relationship between refractive-index gradient with height and the distribution of Bragg backscatter power (Gossard et al., 1999). The refractive-index structure function parameter C_n^2 profile depends mainly on temperature and humidity gradients in the atmosphere as well as turbulence. At the top of a well-defined stratus layer, the strong change in humidity and temperature with height as well as a possible increase of turbulence initiated by wind shear between the two distinct layers can be used as information to detect it. In the presence of precipitation, however, this layer is often masked by the strong return from large falling particles.

3.3 Automatic detection of cloud base and top

3.3.a Case studies

Two single-day case studies are chosen to demonstrate the possibilities and limitations of such ground-based remote sensing systems in determining low clouds. The first case is typical of a day with low stratus changing with time but remaining present the entire day. The second case represents a more complex situation with a thick fog layer developing during the afternoon. The first example illustrates a day with an excellent determination of the stratus (Figure 3.1). On 9 December 2003, a low-level stratus cloud layer was reported in the synops at 00, 09, 12, 15, 18, and 21 UTC and at 00 UTC the following day. At 03 and 06 UTC, fog with visibility below 1 km was observed. In this situation a good determination of the fog and low stratiform cloud situation was possible over 24 h. A few measurement points of the cloud radar (cloud top) retrieval are detected crossing or going

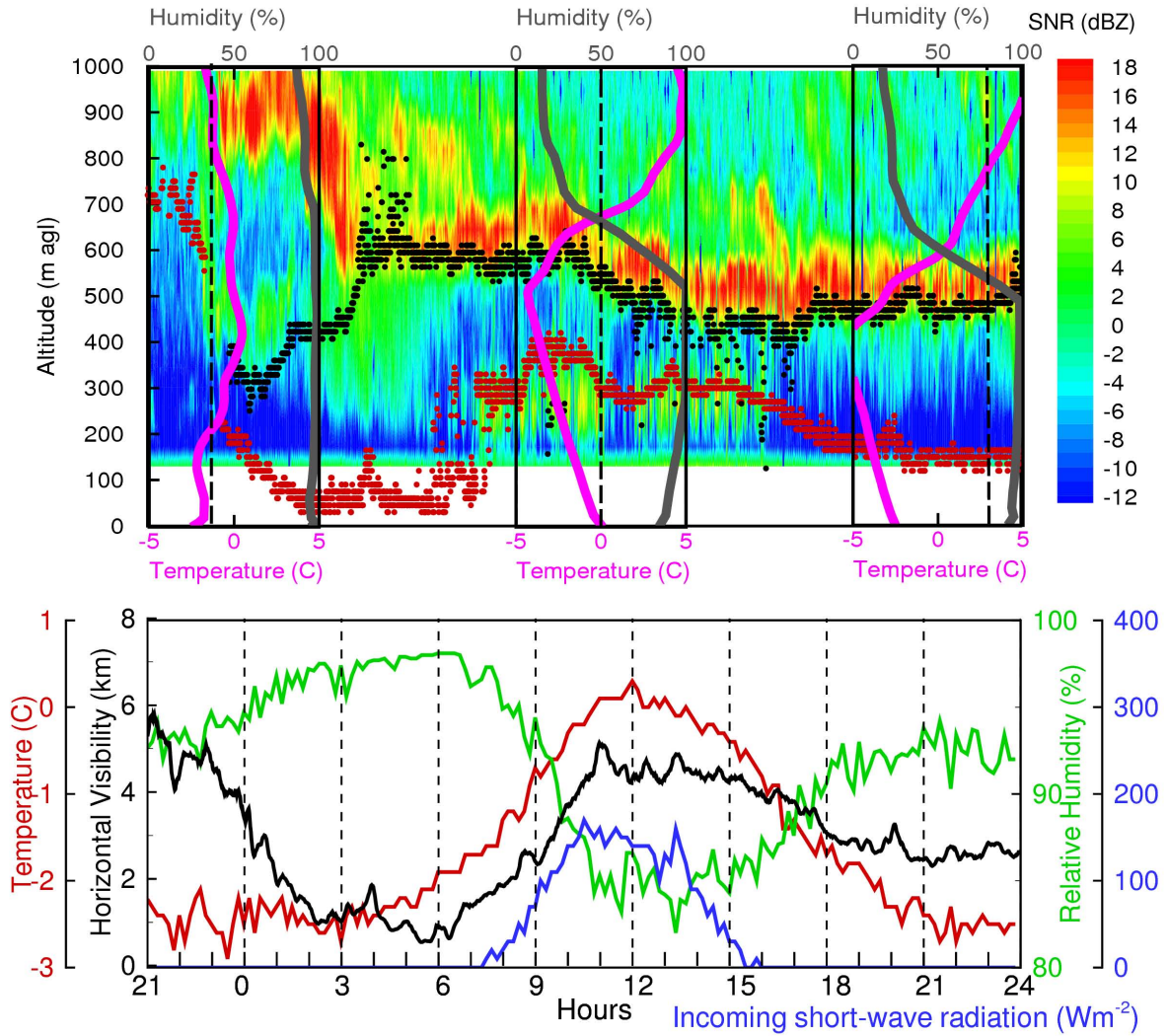


FIG. 3.1: Upper panel: time series of cloud base (ceilometer, red dots), cloud top (cloud radar, black dots), and 2-D color time series of wind profiler signal-to-noise ratio, 9 December 2003, starting at 21 UTC of the previous day. The three rectangles with grey and purple lines correspond to the profiles measured with the radiosounding at 11 and 23 UTC (dashed line = time of sounding, purple line = temperature with a horizontal scale of 10 K, green line = humidity with a horizontal scale of 100%). Lower panel: time series of surface relative humidity (green), temperature (red), incoming short-wave radiation (blue), and horizontal visibility (black).

below the ceilometer (cloud base) signal (after 09 UTC and between 12 and 18 UTC). This may be explained either by the instruments pointing in slightly different directions, or by a height measurement error in one or both instruments.

The determination of cloud base and top was compared with the temperature and humidity profiles measured with radiosoundings from Payerne at 00 UTC, at 12 UTC with a Snow White sensor, and at 00 UTC 8 December 2003 (see the three boxes in Figure 3.1 top panel). At 12 UTC and 00 UTC 9 December there is an excellent agreement between the top of the cloud as detected with the cloud radar and the bottom of the thermal inversion,

indicated by a sharp decrease of the humidity (gray line), and temperature (magenta line) starting to increase with altitude. Confirmation of the cloud-top determination is also obtained by overlaying the data with the Payerne wind profiler signal-to-noise ratio profiles (colored background in Figure 3.1): the intensity of the returned signal depends mainly on humidity gradients and turbulence, producing an intensity maximum just above the cloud layer (Dibbern et al., 2003). On the other hand, when comparing with the first radiosonde profile (00 UTC 8 December 2003), or with the wind profiler SNR between 21 and 03 UTC, the cloud radar seems to give an erroneous cloud top height. Close inspection of the information provided in the top panel of Figure 3.1 reveals the reason for this discrepancy. First, between 00 and 03 UTC, the wind profiler shows higher SNR at two altitudes separated by one region of lower SNR. This may indicate multiple layers in the first 1000 m, of which the cloud radar would have picked the lowest one. Second, the temperature inversion was at 1500 m AGL (not shown), which is out of the limit chosen for the cloud radar top height detection algorithm (1200 m, the study focuses on fog and low clouds). Finally, the ceilometer shows a transition period from a higher cloud layer to well detected low stratus cloud between 21 and 00 UTC. Thus, it can be assumed that there was a transition period until 04 UTC from a multilayer cloud situation in the lower troposphere to a well-defined low stratus cloud situation for the rest of the day.

Surface information (Figure 3.1 bottom) is consistent with a day constantly overcast with a low cloud layer or fog. The relative humidity (green) was high all day long ($> 80\%$), the temperature (red) shows only a modest increase during daytime, and the incoming shortwave radiation (global radiation, blue) is very low even at noon. Similarly, the horizontal visibility was low all day corresponding well with the low visibilities reported in the synops, even though the correspondence is not perfect (synops indicate > 10 km of visibility at 00 UTC, then visibility < 2 km until 15 UTC, then again > 10 km).

The case of 19 November 2003 is an example where the determination of the fog base and top was not possible for the whole day with the two systems running in parallel. During this day, fog and cloudy conditions alternated. Fog was reported in the synops at 06, 15, 18 and 21 UTC, as well as 00 UTC. Figure 3.2 displays the data retrieved from ceilometer and cloud radar for that day. The cloud radar was unable to detect the fog top corresponding to observations at 18, 21, and 00 UTC, but the fog base was well detected with the ceilometer. At 06 UTC the cloud top was not detected, but the cloud base and top of a layer of fog was detected during the previous hour, while at noon, the base and top of a cloud layer was detected by the ceilometer and cloud radar, even though the observation at that time did not report fog. In the period between 10 and 15 UTC conditions were unstable with fog setting and clearing, which explains the apparently contradictory results. Radiosounding temperature and humidity profiles recorded at 00, 12, and 00 UTC the next day are consistent with the reported intermittent fog situations. The two radiosoundings at 00 UTC show a high relative humidity (gray line) with a sudden decrease between 200 and 400 m AGL. At 12 UTC, the humidity is high but not as much as expected in a foggy situation, and the drop at around 300 m is less marked. The humidity at this time may have been too low for a dense fog to set up, and fog and mist episodes alternated. This explains the fog detection by the ceilometer and cloud radar while the observation at noon did not report fog, and the relative humidity from the profile being below the selected threshold. Wind profiler signal-to-noise ratio profiles also show patchy

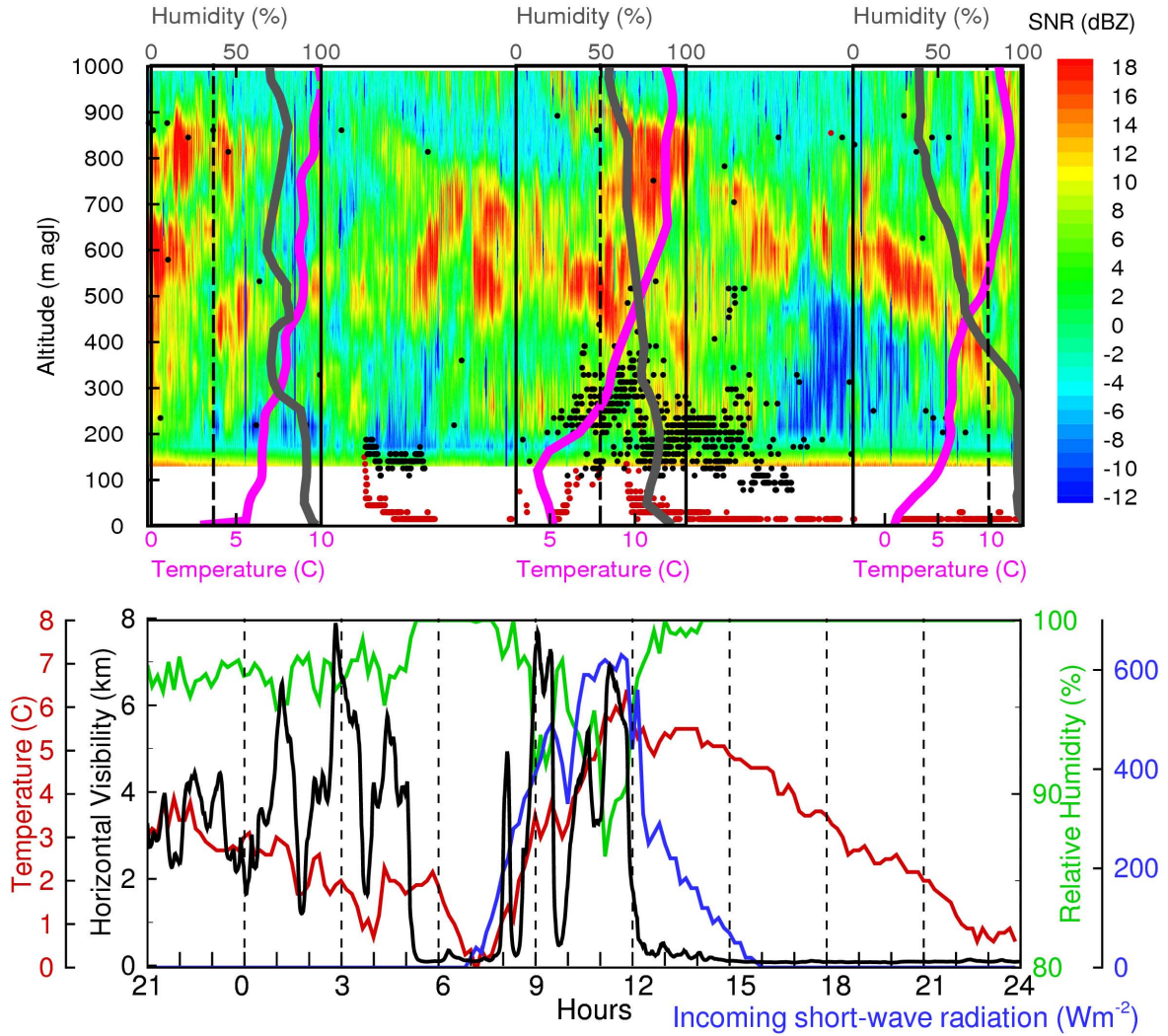


FIG. 3.2: Same as FIG. 3.1, but for 19 November 2003.

layers that indicate variable hydrolapse and temperature inversion height and strength. This is likely to be associated with alternate presence and absence of fog or cloud. The surface information (Figure 3.2 bottom) is consistent with such a situation, as well. The relative humidity (green) was above 80% all day and 100% when fog was reported. The horizontal visibility varied between 0 and 8 km. The very low visibility observed at 18, 21, and 00 UTC also confirms the presence of fog. Temperature (red) and shortwave radiation (global radiation, blue) are as expected for such conditions.

The alternated fog and cloud conditions are confirmed by multiple observations and can explain the relatively poor performance of the cloud radar particularly when fog was present. Possible explanations are the droplets being too small to be detected by the radar or the presence of water on the reception dish of the system (the dish which was not heated, and the relative humidity being 100% during that period, it is highly probable that water condensed on the instrument). Finally, it is possible that in some cases, the top of the fog layer was below the lower detection height of the cloud radar.

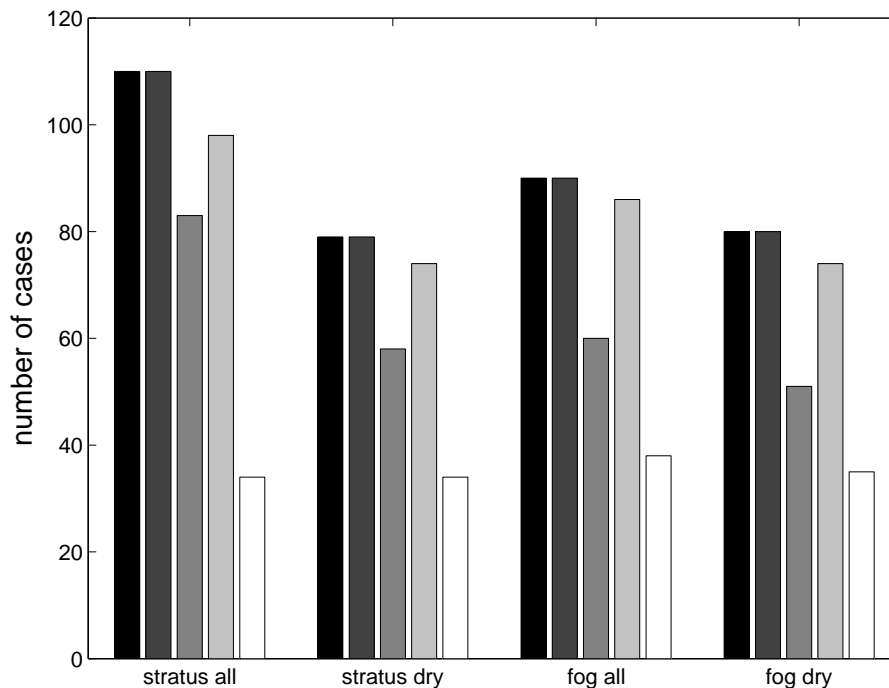


FIG. 3.3: Number of stratus cloud and fog cases detected at time of synop observations during the TUC campaign. Four groups describe all stratus cases, stratus cases without precipitation, all fog cases and fog cases without precipitation. Shaded bars from left to right: all cases detected by synop observation (black), ceilometer operative (dark grey), cloud radar operative (grey), ceilometer retrieval successful (light grey) and, cloud radar retrieval successful (white)

3.3.b Automatic detection of cloud-base and -top performances during the TUC experiment

During the TUC campaign, human eye reports stated 200 stratus cloud or fog situations, divided into 110 stratus cloud and 90 fog observations (Table 3.2). The efficiency of the automatic cloud detection with the ceilometer and cloud radar was evaluated using only the measurements performed concurrently with the operational synops. Since synop are performed every 3 h and cloud situations can evolve significantly in a much shorter duration, the cases can be considered independent of each other. The ceilometer was operational for all cases and the FMCW radar for 143 of them. For the rest of this section only cases where both remote sensing systems were in operation (143 cases) are analyzed. This consists of 83 cases of low stratus clouds, including 25 cases with precipitation, and 60 fog cases including 9 cases with precipitation.

For the stratus situations, the ceilometer retrieved cloud bases in 89% of the situations (74 of 83 cases, see Table 3.2 and Figure 3.3), while the cloud radar retrieved the cloud top in 41% of the cases (34 out of 83). All the 34 latter cases were also in the 74 cases when cloud base was retrieved by the ceilometer. Furthermore, it was not possible to retrieve cloud top with the FMCW radar in the low stratus cloud situations with precipitation, and consequently all 34 cases were dry low stratus situations. Considering only dry situations, the ceilometer retrieved the cloud base in 97% of the cases (56 out of 58),

and the cloud radar also detected the cloud top in 59% of the cases.

In 59 of the 60 fog situations, the vertical visibility could be retrieved by the ceilometer (98%), leading to the detection of a lower boundary, while the cloud radar detected the cloud top in 63% of the situations (38 of 60 cases). In fog situations also, precipitation again made cloud-top detection with the cloud radar more difficult. Three situations with drizzle were detected by the cloud radar out of nine fog situations with precipitation. When cases with any form of precipitation are disregarded, the fog detection with both systems worked for 69% of the observed fog situations (35 of 51 cases).

TABLE 3.2: Rate of cloud base and top detection, relative to the total observed situations for both systems operative during TUC in Payerne, Switzerland

	Total Observations	CR&CM operative	CR (cloud top)	CM (cloud base)	CR&CM simultaneous detection
Stratus all	110	83	34 (41%)	74 (89%)	34 (41%)
Stratus dry	79	58	34 (59%)	56 (97%)	34 (59%)
Fog all	90	60	38 (63%)	59 (98%)	38 (63%)
Fog dry	80	51	35 (69%)	50 (98%)	35 (69%)

In addition to assessing the detection efficiency, the height of the upper boundary determined by the cloud radar was also compared with the height of this boundary determined using humidity radiosounding profiles. During the TUC campaign humidity and temperature profiling radiosoundings were performed in some cases at 03, 06, 09, 15, 18, and 21 UTC in addition to the regular 00 and 12 UTC radiosoundings. Among the cases analyzed earlier for cloud detection efficiency, 25 radiosounding humidity profiles were measured concurrently with cases when the fog or low cloud upper boundary was detected by the cloud radar. For these cases, we compared the determination of the cloud radar at the time of sonde launching with the height determined using the humidity profile. Figure 3.4 shows the extent of the cloud as determined by the ceilometer and cloud radar for the 25 selected cases. It also shows the cloud-top determination using the information from the sounding humidity profile. The average difference between the radiosounding and cloud radar determination of the cloud upper boundary is 53 m (radiosounding – cloud radar). The standard deviation of the sample is 77 m, which leads to an estimate of a 95% confidence interval on the average of 32 m, using a Student’s t test with 24 degrees of freedom (small sample test). Consequently, a positive bias of 53 ± 32 m exists between the radiosounding and cloud radar determination of the upper cloud boundary. Among the 25 selected cases, the cloud extent (cloud top from cloud radar and cloud bottom from ceilometer) varied from 50 to 585 m, while the cloud top as determined by the cloud radar varied from 110 to 1020 m (see Figure 3.4).

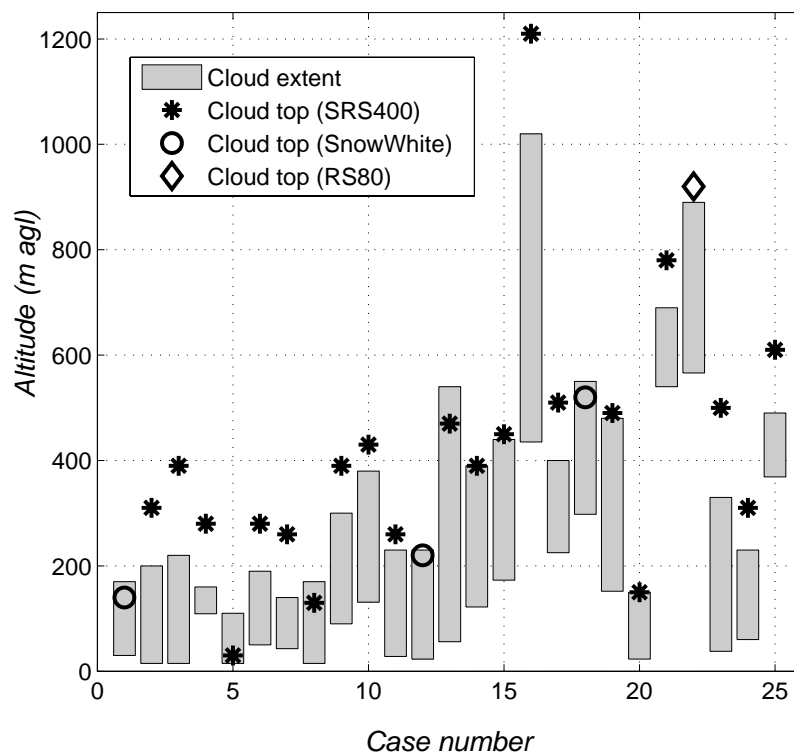


FIG. 3.4: Comparison of cloud extent (cloud base from ceilometer to cloud top from cloud radar) with determination of cloud top from radiosounding humidity profile (radiosoundings include 3 types of sondes: SRS400, SnowWhite and RS80).

3.4 Discussion

We first discuss the reasons limiting the efficiency of fog and low cloud detection by the ceilometer and cloud radar, and then the quality of the cloud upper boundary determination by the cloud radar. Finally, the case studies are looked into, and our results are compared to other studies. Concerning the detection efficiency, the main limiting factor of the experiment was the availability of cloud radar data. The cloud radar used during the campaign was not an operational system, but a prototype, and was affected by problems typical of prototypes, limiting the data availability. Therefore some loss of data due to communication failure, changes of settings according to local conditions and other problems was inevitable. Considerable availability and performance improvements are expected with a new system currently under construction. These include improvement in sensitivity, a reduction in the occurrence of data artifacts, particularly when there are strong returns (e.g., in presence of precipitation), and a general improvement in the stability and reliability of operation. In other systems of comparable complexity (e.g., wind profilers or stratospheric ozone monitoring radiometer) operational mode data availability better than 95% is achieved (Engelbart et al., 2008). In the following discussion, the 143 situations with both remote sensing system operatives are considered.

The ceilometer showed excellent efficiency as 98% of the fog situations and 89% of the low stratus situations could be determined. Restricting the stratus cases to situations

without precipitation allows an overall detection efficiency $> 95\%$. The lower efficiency in case of precipitation is explained by the laser light of the instrument being scattered back by the hydrometeors.

In the case of the FMCW radar, precipitation (snow and rain) produces artifacts in the reflectivity signal. It was thus not possible to determine the cloud top when precipitations occurred, using the algorithm for cloud-top detection. However, under fog conditions with drizzle, the determination of the top of the cloud was still possible. Boers et al. (2000) mention similar limitations with precipitation for the Delft Atmospheric Research Radar (DARR), which is an FMCW radar operating at 3.315 GHz with a range of 15 m. In the current study, about 60% of the stratus cloud tops and 70% of the fog tops could be determined under dry (without precipitation) conditions. In the remaining cases, the cloud top may sometimes have been outside the detection range of our algorithm, which was set to 1200 m AGL. Another possibility for cases when the FMCW cloud radar did not detect the cloud top in dry situations may be its lack of sensitivity to small droplets, or to saturation in the first range gates in the presence of very thin fog layers. Finally, further improvement of the cloud-top retrieval algorithm would probably result in better scores (e.g., in the case of multilayer clouds).

Comparison of the stratus cloud or fog upper boundary determination by the cloud radar with that using the radiosonde profile revealed a statistically significant bias of about 50 m. Ruffieux et al. (2006) mentioned that the SRS400 (used in 21 of the 25 studied cases) is affected by a bias of about 100 m in the determination of the hydrolapse above fog or low stratus cloud layers, compared to other radiosondes. Our comparison shows a similar but smaller bias. In addition, it should be noted that for the three cases using a Snow-White sensor and the case using a RS80 sensor all differences are within ± 30 m. Ruffieux et al. (2006) attributed the bias of the SRS400 to a combination of droplets contaminating the protective duct of the carbon hygistor and lower ventilation early in flight, while the balloon is still accelerating. Taking into consideration that the determination of the fog or stratus cloud upper-boundary determination by the SRS400 is affected by a positive bias, the 95% confidence interval of about ± 30 m shows a good agreement, given that both the radiosonde and the cloud radar height resolution is about 15 m. Finally, comparison with the wind profiler SNR confirmed that the highest SNR is normally found just above the cloud radar-determined upper boundary, as expected.

The case study of 9 December (Figure 3.1) further demonstrates that the capabilities of the ceilometer and cloud radar combination to determine cloud boundaries are good for well delimited clouds. In this case, the location of the cloud top as determined by the cloud radar is confirmed during the day by the high signal-to-noise ratio of the wind profiler and the inversions detected by the radiosoundings (section 3.3.a). This excellent result was helped by good conditions such as the absence of precipitation, well-defined low stratus cloud and a marked inversion at the top of the cloud. The cloud top detected with the radiosoundings at 00 and 12 UTC 9 December and 00 UTC 10 December 2003 (2 SRS 400 and 1 Snow White sounding) also agrees within 10–110 m with the cloud-top observation of the cloud radar.

The case of 19 November 2003 shows that such detection is more complex when the

boundaries themselves are not well defined as inferred from the sounding profiles and the wind profiler signal-to-noise ratio time series. Note that the stratus cloud situations are reported by ground-based observations. The clouds may be multilayered and/or nonhomogeneous, which is difficult to assess since the first cloud layer hides potential higher cloud layers. This hypothesis is given weight by the wind profiler SNR that at some times shows multiple maxima at different altitudes, and also exhibits a large and rapid variability with respect to time. In such cases, the retrieval of the cloud top seems to be hampered by the nature of the cloud itself (inhomogeneous, rapidly changing, etc.). In addition, the ceilometer detected a very low base after 12 UTC and the visibility was below 1 km indicating the presence of ground fog. Therefore, it is also possible that the fog top was below the lower detection limit of the cloud radar.

For situations without precipitation the combination of cloud radar and ceilometer is promising for the detection of fog and low stratus clouds. Despite its prototype nature, the cloud radar already displayed satisfactory performances, and its cloud-top height detection efficiency will be further enhanced by improvements in its algorithm and design. The two systems running in parallel deliver information at a very high temporal resolution with a reasonable cost, which would allow deployment at additional meteorological stations in Europe or over the world. They can give valuable information for the understanding of the development of clouds, help establishing cloud climatology, and improve the analysis of cloud–radiation interaction. Protat et al. (2006) showed that in order to evaluate the representation of clouds in operational models, the use of both a cloud radar and a lidar is imperative. The sampling should be regular but not necessarily continuous, and should not be driven by meteorological conditions. In comparison, the setup of the systems used for the TUC campaign was limited in altitude. For high cloud detection, the cloud radar should be used with a different setup and a ceilometer with a longer range should be used.

As mentioned in section 3.2, it is better to use a ceilometer for detecting the base of clouds, rather than using the cloud radar for determining both boundaries. The cloud radar is more sensitive to precipitation and the detection of the cloud base is attenuated (O’Connor et al., 2005). The radar reflectivity is dependent on the drop concentration and on the sixth power of the droplet diameter so the larger precipitation droplets in and below a cloud dominate the radar return. Therefore, the radar is able to detect the large droplets but clear distinction between precipitation and cloud is not possible. The ceilometer is efficient for measuring the cloud base; its dependency to the concentration of the droplets is only affected by the square of the drop size. However it cannot normally detect the cloud top due to attenuation of the beam in the cloud. The cloud radar can penetrate the cloud and detect the cloud top. Further advantages of this FMCW radar system are the low costs compared to other cloud radars and the simplicity to operate them in a continuous way. The estimated cost of the prototype was at least a factor of 2 below that of a commercially available pulsed system, and even a combination of a Vaisala ceilometer and FMCW cloud radar would remain significantly less expensive than a pulsed system.

Other studies attempted to assess the potential for detecting the cloud boundaries by different means. Wang et al. (1999) analyzed cloud radar and ceilometer data to deter-

mine cloud vertical structure during the Atlantic Stratocumulus Transition Experiment (ASTEX) in June 1992 and compared the results with satellite and radiosonde data. They also used radiosoundings for determining low cloud base and top for a 20-yr dataset in the ASTEX region. They conclude that a combination of cloud radar, ceilometers, and lidar is needed to provide the most accurate and complete information on cloud vertical structure. Using radiosoundings severely limits the number of locations and the time resolution.

The temporal resolution (30 s) of the wind profiler is well suited for this task, but its cost is the main limiting factor for an operational network. Further studies are under way to combine wind profiler information with other systems to improve unambiguous determination of cloud levels (Engelbart et al., 2008).

The collocation of cloud radar and ceilometer was also tested during the Cloud and Radiation experiment (CLARA) in 1996. Hollars et al. (2004) presented comparisons of data from a vertically pointing 35-GHz Millimeter Wave Cloud Radar (MMCR) and the Geostationary Meteorological Satellite (GMS-5). Retrievals of both single-layer and multilayer clouds as seen by radar were compared, but only for satellite-detected clouds with 100% coverage of one cloud type within a $0.3^\circ \times 0.3^\circ$ domain centered at the Atmospheric Radiation Measurement (ARM) site on Manus Island in the tropical West Pacific. Good agreement of the cloud-top heights was found between MMCR and GMS-5 retrievals. For convective clouds with heavy precipitation, MMCR retrievals underestimated the cloud-top heights significantly.

Ground fog detection has been shown to be possible from space using data from the Moderate Resolution Imaging Spectroradiometer (MODIS) during daytime (Bendix et al., 2005) and from the Spinning Enhanced Visible and Infrared Imager (SEVIRI) aboard Meteorological Satellite (Meteosat) Second Generation (Cermak et al., 2006). Encouraging performance was found for the discrimination between low stratus and ground fog, but the method of Bendix et al. does not yet allow indisputable distinction.

3.5 Summary

A combination of both ceilometer and cloud radar has the potential for providing the height of a cloud layer with optimal efficiency in continuous operational mode (by optimal we mean satisfactory capabilities at a reasonable cost). These instruments complement each other: the ceilometer is very efficient at detecting clouds and can locate the bottom of a cloud layer precisely, but cannot usually detect the cloud top due to attenuation of the beam in the cloud. On the other hand, the cloud radar is able to detect the cloud top, although signal artifacts can cause difficulties during precipitation. It could eventually detect higher layers in case of multilayered clouds. Furthermore, the cloud radar used in this study was a prototype system and considerable performance improvements are expected with a new system. Once set up and adjusted to the local conditions, the systems operate autonomously and require little maintenance. The costs of both systems are low compared to other types of radar. This makes these systems in combination with another system to estimate the cloud cover amount a good alternative when human observations

are not available for monitoring low cloud evolution.

Comparison of the cloud-top height determination by the cloud radar and using radiosounding humidity profile showed a bias of about 50 m. A previous study mentioned that the determination using radiosounding humidity profile with the type of sonde operated during the campaign suffered from a bias of even larger magnitude (about 100 m). Once a 50-m bias is taken into account, the agreement between both determinations is good. Comparison with wind profiler data confirmed the quality of the cloud-top height determination by the cloud radar. To improve information on the accuracy of the cloud boundary retrievals with the ceilometer and cloud radar, systematic comparisons should be made in future studies with 94-GHz cloud radar, which have a higher sensitivity to small droplets compared to the FMCW radar. Additionally, cloud-top height could also be compared with satellite data.

In this study, the information from two systems was combined in order to provide a better description of a cloud layer. It was possible to achieve this in a simple and straightforward manner because both systems deliver the same type of information (elevation of a layer). When information from more systems is integrated, this task becomes more difficult, especially when the information provided cannot be easily combined. In this study, it would have been relatively difficult to also integrate the information from the wind profiler and the radiosounding. While the information from these systems is clearly related to the information from the ceilometer and the cloud radar, their relationship is not straightforward. A promising direction to explore for more ambitious multisystem integration is the Bayesian model-based inversion technique such as explored by Löhnert et al. (2004).

Chapter 4

Solar irradiance computations compared with observations at the BSRN Payerne site

Daniela Nowak¹, Laurent Vuilleumier², Charles N. Long³, and Atsumu Ohmura¹

Published in *Journal of Geophysical Research – Atmospheres*, 113, D14206, 2008,
[doi:10.129/2007JD009441]

In this Chapter, the capability of a radiation transfer model (MODTRANTM) to simulate atmospheric radiation transfer in clear sky situations is tested. Cloud free cases are carefully selected to perform clear sky radiation fluxes simulations. These are then compared to BSRN radiation observations. This Chapter represents an important stage before undertaking simulations including stratus cloud situations. It helps identifying the requested observations for the model input and determining the performance of the model for the PAY site. Additionally, the methods developed for these clear sky simulations considerably facilitate later model simulations with clouds.

ABSTRACT

Radiative transfer model calculations of solar fluxes during cloud free periods often show considerable discrepancies with surface radiation observations. Many efforts have been undertaken to explain the differences between modeled and observed shortwave downward radiation (*SDR*). In this study, MODTRAN4v3r1TM (designed later simply as MODTRANTM) was used for model simulations and compared with high quality radi-

¹Institute for Atmospheric and Climate Science, ETH Zurich, Switzerland

²Federal Office of Meteorology and Climatology MeteoSwiss, Payerne, Switzerland

³Pacific Northwest National Laboratory, USA

ation observations of the Baseline Surface Radiation Network (BSRN) site at Payerne, Switzerland. Results are presented for cloud free shortwave downward radiation calculations. The median differences of modeled minus observed global *SDR* are small ($< 1\%$) and within the instrumental error. The differences of modeled and observed direct and diffuse *SDR* show larger discrepancies of -1.8% and 5.2% respectively. The diffuse *SDR* is generally overestimated by the model and more important, the model to observation linear regression slope and zero-intercept differ significantly from their ideal values of 1 and 0. Possible reasons for the discrepancies are presented and discussed, and some modifications are investigated for decreasing such differences between modeled and observed diffuse *SDR*. However, we could not resolve all the discrepancies. The best agreement is obtained when comparing model simulations whose 550-nm aerosol optical depth input is inferred from observations using nine spectral channels, and using BSRN observations performed with a new and more precise shading disk and sun tracker system. In this case, the median bias between model simulations and observed diffuse *SDR* is -0.4 Wm^{-2} ($< 1\%$).

4.1 Introduction

Solar energy in the shortwave range between 0.3 and 4 μm is the principal source of energy for the global earth-atmosphere system. Detailed knowledge of the solar radiation transfer through clear and cloudy atmosphere is crucial to determine any potential change of the earth's radiation budget in a changing climate. Yet radiative transfer model calculations of solar fluxes often show significant discrepancies with observed diffuse shortwave downward radiation at the surface.

Numerous efforts have been attempted to resolve these differences. Disagreements between modeled and observed downward broadband fluxes under clear-sky conditions have been reported by many authors. Kinne et al. (1998) showed that model predictions of solar broadband downward hemispheric fluxes at the surface under cloud free conditions during four selected days of the FIRE 1991 experiment were up to 10% larger than corresponding measurements. An error up to 5% could be attributed to underestimates of near-infrared absorption in solar radiative transfer models. An error of about 4% in solar broadband fluxes was related to disagreements in diffuse solar fluxes.

An intercomparison performed with 15 different radiative transfer models (RTM) and one global circulation model (GCM) (Halthore et al., 2005) showed that model computations generally exceed measured values of the diffuse shortwave downward radiation (*SDR*) by a margin that cannot be accounted for by measurement uncertainties. In a comparable study, Henzing et al. (2004) found that model calculations exceed diffuse irradiance measurements by 7 - 44 Wm^{-2} (average: 25 Wm^{-2}). There has been speculation as to whether an unknown gaseous absorber in the atmosphere could be responsible for the missing observed *SDR* compared to the models (Kato et al., 1997). Part of the problem of the "excessive" absorption can be explained when global and diffuse *SDR* measurement underestimations due to pyranometer thermal offset are taken into account (Philipona, 2002). Additionally it should be noted that greater discrepancies are observed in low-altitude and midlatitude regions but are less pronounced in the Arctic as was shown in a study by Barnard and Powell (2001). For cloud free days at the North Slope Alaska (NSA) sites of Barrow and Atqasuk (part of the Atmospheric Radiation Measurement - ARM - program) the direct normal irradiance is underestimated by about 1%, but the diffuse irradiance is well predicted (about 0.4 Wm^{-2} when averaged over 12 cases considered). Barnard and Powell (2001) also compared their results with calculations of clear sky cases at the Southern Great Plains (SGP), a midlatitude site of the ARM program. At SGP the model clearly overestimates the diffuse irradiance (13 Wm^{-2}) as observed by Halthore and Schwartz (2000). In an experiment focusing on resolving disagreements between models and measurements of the diffuse horizontal broadband shortwave irradiance, Michalsky et al. (2006) obtained a good agreement with measurement to model differences between -0.6% and +1.9% (for more details see section 4.7).

An ongoing project at the Payerne BSRN station is aimed at the determination of the effect of clouds on radiation. However before attempting to study radiative transfer through cloudy atmospheres, the performance of the radiative transfer model MODTRANTM must be tested for cloud free situations at the midlatitude and low-altitude site of Payerne, Switzerland. This research is based on a sample of about 60 well-defined noontime clear

sky situations selected from the available 2001–2005 data screened using human eye observations (Müller, 1982), and the algorithm of Long and Ackerman (2000). A set of observed atmospheric data are used to represent the modeled atmosphere over Payerne as precisely as possible. This dataset includes the measured atmospheric profile of pressure, temperature, and humidity, the aerosol optical depth (AOD), the total ozone and an interpolation of the CO₂ concentration. The aim of this paper is to evaluate the capability of reproducing cloud free radiation observations using MODTRANTM for well-defined clear sky cases, using ancillary atmospheric data and tested against high quality radiation observations at the surface.

4.2 Data and Instruments

4.2.a BSRN shortwave radiation measurements

High accuracy radiation measurements are available at the Baseline Surface Radiation Network (BSRN) station at Payerne (46.812°N, 6.942°E, 491 m asl). The station at Payerne is one of 39 operative BSRN radiation observation sites spanning over the globe. The objective of the BSRN is to provide observations of shortwave and longwave surface radiation fluxes of the best possible quality, using a high (1 Hz) sampling rate. These measurements are taken from a small number of selected stations, in contrasting climatic zones, together with collocated surface and upper air meteorological data and other supporting observations (Ohmura et al., 1998).

In Payerne *SDR* components are measured with different types of instruments. The direct *SDR* measurements are made with a Kipp & Zonen CH1 pyrhelimeter operated since 1 January 1995. The CH1 is mounted on a sun tracker with a tracking accuracy of 0.1°. The solar spectrum from 0.2 to 4.0 μm is measured with a full viewing angle of 5°. The direct solar radiation measurement systematically includes some diffuse *SDR* due to its field-of-view. The CH1 is frequently compared at Payerne with a PMO6 absolute open cavity radiometer designed at the Physikalisch-Meteorologisches Observatorium Davos. The diffuse and global *SDR* are measured with shaded and unshaded Kipp & Zonen CM21 pyranometers, respectively. The pyranometers integrate hemispherically over a horizontal receiver surface, and cover a spectral range from 0.305 to 2.8 μm . The measurements of direct, diffuse and global *SDR* are sampled at 1 Hz, and 1-minute mean values are recorded, as well as the sample minimum and maximum values, and the sample standard deviation. The pyranometers for the diffuse and global *SDR* measurements are ventilated and heated. In addition, the instruments are calibrated at the World Radiation Center (WRC) at Davos, Switzerland and are regularly compared with reference instruments with recent calibration from the WRC.

Since 18 July 2002 diffuse *SDR* has been measured with two different shading systems running in parallel at the BSRN Payerne station. The original shading system (operating since October 1992) includes an axis that is parallel to the Earth rotation axis and is only automated for the solar azimuth apparent motion. The day-to-day changes in maximum sun elevation must be adjusted manually, which is performed at noon when there is direct sun producing a shadow surrounding the sensor. Because of the uncertainties generated by the shading disk location, the shading disk is larger than optimum and thus blocks

an enlarged part of the diffuse irradiance measurement (corresponding to an opening angle on the order of $\sim 15^\circ$). The optimum disk size is one shading a portion of the sky corresponding to the field-of-view of instruments measuring direct irradiance, thus the sum of the direct plus diffuse measurements give an accurate total (global) downwelling SW amount. A new shading system on a fully automated sun tracker was introduced in July 2002. This new system includes a shading sphere that is of the desired size (corresponding to an opening angle of $\sim 4^\circ$). Erroneous measurements caused by improper shading or alignment are avoided by the precise sun tracking system. This study uses data from 1 January 2001 to 31 December 2005. From July 2002, two diffuse shortwave datasets are available: from the old ($SDRdif_{old}$) and new shading system ($SDRdif_{new}$). When the whole period is studied, only the measurements from the old system are used to ensure consistency of the dataset. But for some of the more detailed comparisons, the period from July 2002 only is studied, using the diffuse data from the new shading system.

The stated accuracy requirements of the BSRN for the global and diffuse irradiance are 5 Wm^{-2} , and 2 Wm^{-2} for the direct irradiance (Ohmura et al., 1998) when using absolute cavity radiometers. These are accuracy targets that have been shown to be reachable for calibration precision, though with no available means to determine total calibration absolute accuracy except for the absolute cavity derived direct component. Additional uncertainty in actual field measurements also includes uncertainty with short-term variability (statistical) from a variety of causes including thermal effects, non-ideal shading of the instruments, cleanliness of the sensor, etc. Recently the errors of the CM21 pyranometers and the CH1 pyrhelimeter have been estimated for the Payerne site for a one year measuring period (October 2004 – October 2005) (Ruckstuhl, 2008). Such studies allow estimating the components of the uncertainties, mean biases being mostly related to calibration uncertainty and root mean squared error (RMSE) being mostly related to statistical uncertainty. Our observations were compared with observations of instruments of the Arctic Radiation Budget Experiment (ARBEX, installed at Payerne for a period of one year) designed at the PMOD. The monthly mean error (RMSE) of the global SDR measured with an unshaded CM21 is about 1.6% (2.3 Wm^{-2}) with a bias of about -2.3 Wm^{-2} . If the global SDR is taken from the sum of the shaded CM21 and the CH1 pyrhelimeter the monthly RMSE is 3.7% (5.4 Wm^{-2}) and the bias is -5 Wm^{-2} . However, when using the $SDRdif_{new}$ observations with the new suntracking system and more accurate shading disk for this comparison, the result is significantly better. In this case, the monthly RMSE is on the order of 2 Wm^{-2} (1.3%) and the bias is -1.9 Wm^{-2} . Furthermore, the accuracy of the direct irradiance measurement (CH1) was not analyzed separately. Ideally, a comparison would be made with separately measured direct and diffuse SDR observations, which was not possible with ARBEX, because it includes only the global SDR . Using ARBEX for comparison should therefore underestimate the uncertainty of our global SDR measurement with respect to the sum of direct plus diffuse, because both the ARBEX and our global measurement share many technical characteristics, and thus potential systematic uncertainties, particularly those linked to non-ideal angular response.

Another source of uncertainty of the pyranometer measurements is the thermal offset, or infrared energy loss. It is caused by the temperature difference between the heat sink of the instrument and the radiatively colder sky producing differential radiative cooling of the instrument. The radiative cooling is transmitted from the outer to the inner dome,

and induces thermal negative offsets due to thermal emission of the sensing element to the dome (Philipona, 2002). The magnitude of the night offset for the global and diffuse *SDR* at Payerne with the instruments used is on average on the order of 1.5 Wm^{-2} , though as Philipona (2002) notes the IR loss during daylight is likely somewhat larger.

4.2.b Aerosol optical depth

Aerosol optical depth (AOD) is measured within the Swiss Atmospheric Radiation Monitoring (CHARM) network at 4 stations (Payerne, Locarno-Monti, Davos and Jungfraujoch). Measurements of the AOD are performed with Precision Filter Radiometers (PFR) (Wehrli, 2000) at different wavelengths. At Payerne, the measurements started in October 2000 at 4 wavelengths (368, 412, 500 and 862 nm). Since July 2002 the PFR dataset includes measurements at 16 wavelengths enabling the determination of the AOD at 9 wavelengths (368, 412, 450, 500, 610, 675, 778, 862 and 1024 nm). The full opening angle is 2.5° and the slope angle 0.7° . Since measurements are not performed at 550 nm (which is required for the model input), Ångström exponents α and β obtained by fitting the measurements were used to derive AOD at 550 nm (Ångström, 1930):

$$\tau_\lambda = \beta\lambda^{-\alpha}, \quad (4.1)$$

where τ_λ is the approximated aerosol optical depth at wavelength λ (in μm), exponent α gives information of the aerosol particle size and β is the Ångström's turbidity coefficient. The setting with 9 wavelengths adds three wavelengths between 550 and 862 nm. The addition of measurements at wavelengths close to 550 nm, particularly the 610 nm observation, should improve the quality of the interpolation at 550 nm. Therefore it is expected that fit-derived AODs at 550 nm are more accurate after July 2002, when measurements at 9 wavelengths are available.

4.2.c Human eye observations

The aerological station of Payerne is an official site for synoptic weather observations, including cloud information, which are performed eight times per day. Cloud cover, type and base height are reported for the three main cloud levels (low, middle and high clouds) as well as the ground visibility (Müller, 1982). The human eye observations are generally of excellent quality and give regular and important information to meteorologists concerning the state of the sky, the meteorological conditions (fog, snow, rain etc.), and the horizontal visibility. The observer must declare a sky not clear (one octa clouds) if the tiniest cloud is visible in the hemisphere (for example the contrail of an airplane). Thus one can be almost sure that a synoptic observation with 0 octas cloud reported was a cloudless moment (as there remains the possibility of the presence of very thin – subvisual – cirrus clouds which are difficult to detect by the observer). However the exact moment of the observation is not known as the observer has a range of approximately half an hour before the designated synoptic observation time. For this study observations around noon were considered in a first selection when 0 or 1 octa of clouds were reported and the horizontal visibility was larger than 10 Km. Situations with 1 octa of clouds were also considered because there is in such case a relatively good probability of finding cloud free measurements between 11 and 12 UTC with the clear sky radiation detection algorithm used as a second selection step (Long and Ackerman (2000), see section 4.3).

4.2.d Radiosounding

Balloon-borne meteorological radiosoundings including pressure, temperature and humidity profiling are performed twice a day at 12 and 00 UTC at Payerne. The sondes are launched at 11 and 23 UTC respectively, an hour before the officially reported time in order to account for the balloon ascent time. Operational radiosoundings are made with SRS 400 sondes (Richner, 1999; Ruffieux et al., 2006). In addition, radiosoundings with the Snow White mirror dew point hygrometer (Miloshevic et al., 2006) are available at irregular time intervals and especially for nighttime ascents. The radiosounding profiles include measurements of the temperature and relative humidity from the ground to about 35 km (relative humidity profiles up to 12 km). The vertical resolution in the lower atmosphere is about 15 m.

4.3 Clear sky detection

The shortwave flux analysis (SWFA) code of Long and Ackerman (2000) includes a method for identifying periods of clear skies for an effective 160° field of view using 1-minute broadband measurements of surface total and diffuse *SDR*. Then an empirical fitting algorithm is applied, using a minimum absolute deviation technique to estimate both the clear-sky global shortwave irradiance and the ratio of diffuse to global irradiance (diffuse ratio) as a function of solar zenith angle. These cloud free *SDR* estimations can then be used to calculate the cloud effect at the surface or to detect cloud free periods for analyses as presented here. The SWFA code was applied to the radiation dataset used in this study for the determination of clear-sky times by objective criteria. A two-step process is applied to select a set of clear-sky cases. First, we select all cases when cloud free sky (0 or 1 octa, 12 UTC observation as explained in section 4.2.c) and a visibility superior to 10 km are reported by the synoptic observations at noon (human eye observation at timestamp 11:40 UTC is chosen to ensure a concurrent radiosounding). Second, the clear sky algorithm output data is checked for cloud free moments within the selected period of time (11 to 12 UTC). The cloud free radiation observation that is closest to noon is selected for the simulation. The difference between observed and the SWFA-estimated cloud free radiation must be smaller than 2 Wm^{-2} to select the case for our MODTRANTM calculations and comparisons. The upper panel of Figure 4.1 shows the diffuse observed and cloud free SWFA-estimated *SDR* between 10 and 12:30 UTC of 4 January 2005. The solid line represents the observed diffuse *SDR*, the dashed line the SWFA-estimated clear sky diffuse irradiance, and the crosses indicate the moments detected as clear sky observations. The lower panel shows the same comparison but for the direct *SDR* (direct irradiance on a horizontal surface). This example is one of the clear sky cases (selected between 11 and 12 UTC) used in the comparisons of modeled and observed *SDR* (see section 4.5). Perfect clear sky situations almost never occur at Payerne. The evolution of the observed direct *SDR* in this example is very smooth, especially between 11 and 12 UTC. The absence of rapid *SDR* variations shows that no clouds, even thin clouds or haze, were present in the line of the direct solar beam. It is thus likely that no clouds were present at low zenith angle, and the somewhat larger variability seen in the diffuse *SDR* is probably due to clouds low on the horizon.

TABLE 4.1: Statistical indicators of the agreement between model simulation and observations for the three analyzed datasets: a) 2001–2005 original dataset with old diffuse shortwave downward radiation *SDR* measurement, b) 2002–2005 with old and new diffuse observation method and aerosol optical depth (AOD) measured at 9 wavelengths, c) 2001–2002 data with old shading system and AOD measured at 4 wavelengths. For each dataset: number of cases, correlation (R^2), median bias in Wm^{-2} and % (the 2.5 and 97.5 percentiles are indicated in brackets), RMSE in Wm^{-2} and %, slope and zero-intercept of model to observation linear regression (95% confidence intervals for the slope and zero-intercept are indicated in brackets).

Data set	Nr. of cases	R^2	Median bias	Median bias	RMSE	RMSE	Slope	Zero-	
			Wm^{-2}	%	Wm^{-2}	%		Intercept	
Global	2001-2005 ^a	61	1.00	-4.5 [-35.5, 10.8]	-0.5 [-3.8, 2.2]	12.0	1.6	0.99 [0.98, 1.00]	2.1 [-7.5, 11.6]
	2002-2005 ^b	41	0.99	-1.3 [-25.3, 14.3]	-0.3 [-3.0, 2.3]	9.7	1.3	0.99 [0.98, 1.00]	3.6 [-6.8, 14.0]
	2001-2002 ^c	20	1.00	-8.2 [-41.0, 8.2]	-1.5 [-4.6, 0.9]	15.6	2.0	0.98 [0.96, 1.01]	1.3 [-16.9, 19.6]
Direct	2001-2005 ^a	61	0.99	-11.2 [-40.4, 2.0]	-1.8 [-5.3, 0.3]	15.5	2.5	0.98 [0.97, 0.99]	-1.3 [-8.8, 6.3]
	2002-2005 ^b	41	0.99	-6.9 [-30.1, 3.1]	-1.2 [-5.0, 0.7]	12.2	1.9	0.98 [0.97, 0.99]	0.7 [-7.3, 8.7]
	2001-2002 ^c	20	0.99	-16.8 [-40.5, -2.3]	-2.8 [-6.3, -0.6]	20.7	3.4	0.97 [0.95, 0.99]	-1.8 [-13.7, 10.1]
Diffuse	2001-2005 ^a	61	0.98	4.5 [-15.1, 15.5]	5.2 [-10.4, 22.0]	7.5	9.1	0.82 [0.77, 0.87]	19.2 [14.6, 23.8]
	2002-2005 ^b	41	0.97	4.5 [-14.5, 10.5]	5.2 [-10.6, 14.0]	6.8	7.8	0.80 [0.74, 0.86]	20.2 [14.6, 25.7]
	2002-2005 ^b	41	0.97	-0.4 [-22.2, 8.3]	-0.4 [-15.1, 10.6]	7.9	6.9	0.77 [0.70, 0.83]	20.2 [13.7, 26.6]
new	2001-2002 ^c	20	0.98	4.4 [-15.2, 16.4]	4.8 [-8.5, 22.6]	8.8	11.3	0.84 [0.76, 0.92]	20.3 [12.3, 28.2]

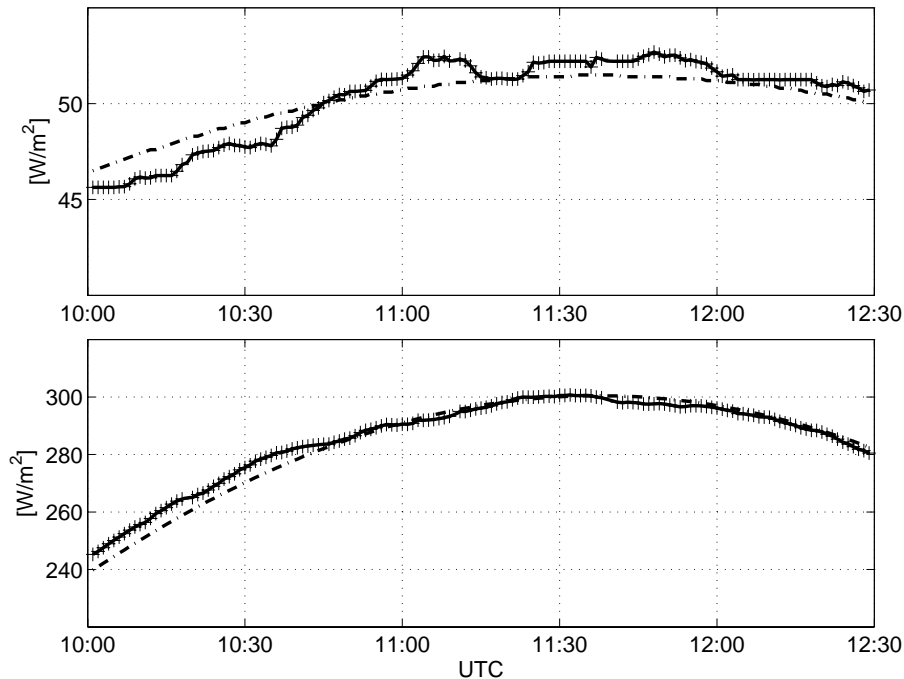


FIG. 4.1: Upper panel: Observed (BSRN) diffuse SDR (solid line) with cloud free detected moments marked as crosses on the solid line, SWFA estimated clear sky SDR (dashed line). Lower panel: same as for the upper panel but for the direct SDR .

4.4 Model and input data

MODTRANTM is a state of the art column radiative transfer model to calculate shortwave (including direct and diffuse components) and longwave radiation fluxes at the Earth's surface or at any other point in the atmosphere from the UV ($0.2 \mu\text{m}$) to the thermal infrared ($>100 \mu\text{m}$). For detailed information about MODTRANTM and the range of applications see Berk et al. (1998, 2003). For this study, MODTRANTM band model calculations were made for a spectral range of 0.294 to $4.0 \mu\text{m}$ with a resolution of $0.005 \mu\text{m}$ using a discrete ordinate (DISORT) multiple-scattering algorithm with 8 streams. Model default profiles of the atmospheric gases O_2 , NO , SO_2 , NO_2 , NH_3 , and HNO_3 were applied. Temperature, water vapor and pressure profiles were taken from 12 UTC radiosoundings (see section 4.2.d) for every case. In addition to the measured atmospheric profiles, default atmospheric model profiles were generated for CH_4 , N_2O and CO corresponding to the season and latitude of the measurement site. Local albedo derived from the ratio of measured reflected shortwave radiation to global shortwave downward radiation was used for the albedo input in the model.

The 550-nm AOD calculated with equation 4.1 was included as AOD model input. However, during clear sky winter days (e.g., in December 2003) the aerosol loads were very small. In some cases the 550-nm AOD was lower than 0.04, which is the lowest limit accepted by MODTRAN4v3r1TM and therefore the AOD model input had to be increased to this minimum value. The CO_2 mixing ratio was derived according to Dürr et al. (2005). A CO_2 mixing ratio of 364 ppm is used as the starting point on January 1, 1996. Then, a simplified yearly cycle of 10 ppm CO_2 with a minimum in mid-August and a trend

of $+2 \text{ ppm}(\text{yr})^{-1}$ was applied. This was derived from CO_2 values of the Climate Monitoring & Diagnostics Laboratory (CMDL) station Schauinsland in southern Germany (Dürr et al., 2005). Total ozone was derived at Arosa using measurements from a Dobson spectrophotometer. Data from Payerne radiosondes were then used to compensate for the ozone difference between the altitude of Payerne (lower) and Arosa. When data were missing, a linear interpolation was used to estimate the total ozone. Atmospheric profiles of the temperature [K], atmospheric pressure [hPa] and absolute humidity [g/m^3] were implemented from radiosoundings up to a height of 10 km above sea level. From 10 to 100 km two default profiles for the Payerne site were used representing climatological means of the aforementioned parameters for the summer half year (April – September) and the winter half year (October – March).

4.5 Results

Cloud free situations at the meteorological station Payerne are rare. Even if human observers report a clear sky situation, *SDR* might be attenuated by dry haze, higher aerosol concentrations in the lowest atmospheric layer or very thin cirrus clouds not considered to be clouds by the observer (subvisual cirrus). Therefore only a limited number of clear-sky situations were found in the radiation measurements dataset from 2001 to 2005. The modeled situations represent the radiation fluxes at a precise time of observation (one minute) and are compared with a 5-minute mean of the measurements around this simulated time t . The mean is calculated from the minute-averaged observed radiation from t minus 2 minutes to t plus two minutes. A total of 61 clear sky situations were selected between 11 and 12 UTC and were used for the comparisons in this study. For the analysis of the differences between model results and observations we always calculate modeled minus observed values.

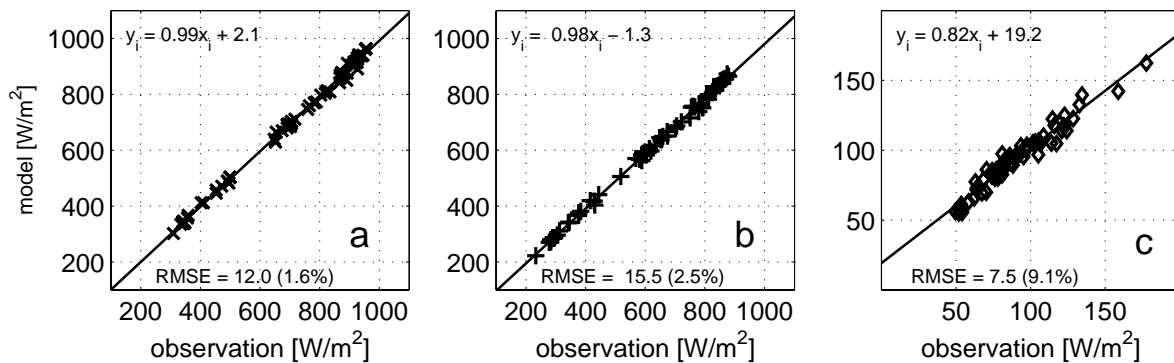


FIG. 4.2: Modeled versus observed global (a), direct (b), and diffuse (c) *SDR*. The correlation is 1 for the global, 0.99 for the direct *SDR*, and 0.98 for the diffuse *SDR*.

Figure 4.2 represents the model simulation results versus observations for the global, direct and diffuse *SDR*, while Table 4.1 provides different statistical indicators of the agreement between model simulations and observations. These indicators include the linear regression, correlation, slope and zero-intercept, as well as median bias, and RMSE. In addition, the 95% confidence interval is indicated for the slope and zero-intercept, as well as the 2.5 and 97.5 percentile of the bias. There is a good agreement between the

simulations and observations for the global *SDR*, with a correlation of 1 and a slope and zero-intercept of nearly 1 and 0, respectively. The median bias is less than 1%, and the RMSE is 12 Wm^{-2} or 1.6%. The direct *SDR* also demonstrates reasonable agreement between simulation and observation. The correlation is 0.99, while the slope is very close to 1, although the confidence interval does not include it, and the zero-intercept is compatible with zero. The median bias is somewhat larger with -1.8%. Similarly, the relative RMSE is also higher than for global *SDR* (2.5%). In the case of diffuse *SDR*, the agreement is poorer. While the correlation is still high (0.98), the slope and zero-intercept are significantly different from 1 and 0, respectively. Furthermore, the median bias is on the order of 5%, and the RMSE is 7.5 Wm^{-2} , which represents more than 9%, because diffuse *SDR* ranges only from 50 to a little over 150 Wm^{-2} when the sky is cloudless.

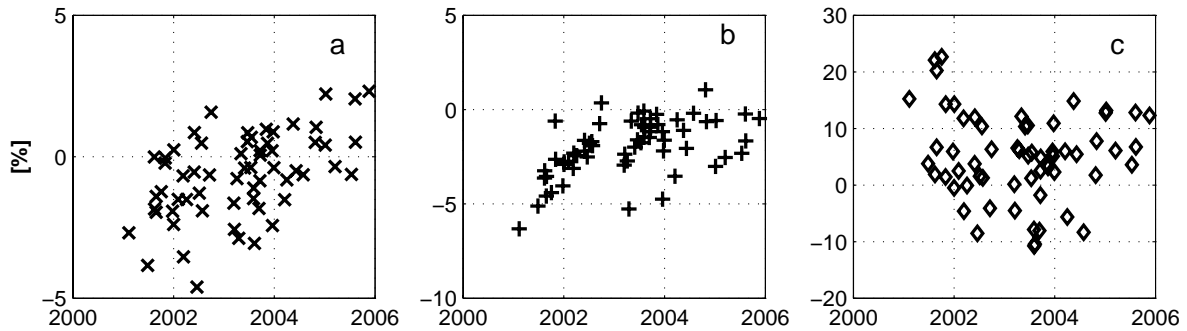


FIG. 4.3: Relative differences (%) of modeled minus observed global (a), direct (b), and diffuse (c) *SDR*.

Figure 4.3 shows the bias (in %) of modeled minus observed irradiances as a function of time. This figure demonstrates that the direct *SDR* differences are almost always negative, meaning that the model systematically underestimates direct *SDR*. On the other hand, diffuse *SDR* differences are mostly (although less systematically) positive, i.e., overestimated by the model. In many cases, this under- and overestimation compensate, and the agreement is better for global *SDR* than for its components. Finally, there does not seem to be an obvious temporal pattern for the differences between model and observations, except that the largest differences in direct and diffuse *SDR* seem to occur before mid-2002. This may be related to the change in the determination of AOD, for which the increase in number of wavelengths resulted in a better quality of the fit used to determine the Ångström parameters.

In the absence of clouds, one of the most influential parameters (other than solar zenith angle) for shortwave radiation transfer is the atmospheric turbidity, for which the main measured parameter in our case is AOD. Therefore it is interesting to check whether the differences between model and observations are correlated with AOD. Figure 4.4 shows these differences as a function of AOD for global, direct and diffuse *SDR*. For global and diffuse *SDR* (Figure 4.4a and c) a negative correlation is clearly visible between modeled minus observed *SDR* and the 550-nm AOD input of the model. For global *SDR*, the model does not underestimate when the 550-nm AOD is below 0.1, and the strongest underestimation occurs for AOD values larger than 0.2. The model also underestimates diffuse *SDR* at larger AOD, while it is significantly overestimating at smaller AOD. Direct *SDR* is generally underestimated (Figure 4.4b), but the underestimation is not obviously

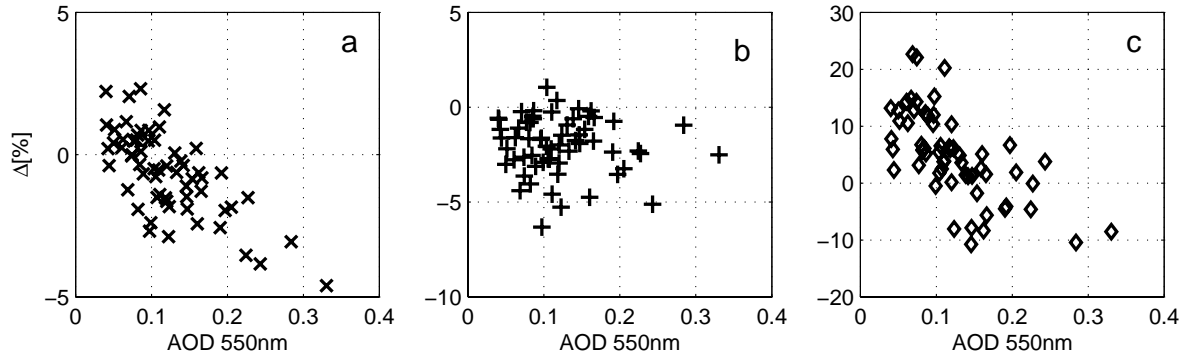


FIG. 4.4: Relative differences (%) of modeled minus observed *SDR* versus the aerosol optical depth (AOD) used in the model calculation, for the global (a), direct (b), and diffuse (c) *SDR*.

correlated to increasing AOD. Thus the negative correlation for the global *SDR*, which includes both the direct and diffuse SW, is primarily related to the negative correlation between the diffuse *SDR* and AOD.

4.6 Discussion

Model simulation results for cloud free cases are reasonably good for the global and direct irradiances. In the following discussion, some hypotheses are put forth for explaining the discrepancies especially for diffuse *SDR*, and different tests are carried out to verify these hypotheses. We first note that diffuse and direct irradiance do not mean the same thing for model results and observations, a difference that is related to the instrument viewing angle and shading disk size as explained in more details below. Two different types of diffuse irradiance observation methods are compared for testing whether such a difference can have a significant effect on the observed discrepancies. Then, we test whether it is possible to compensate for discrepancies in the direct and diffuse *SDR* by adjusting the aerosol model input. We also examine what can be the influence of uncertainties in the surface albedo description. In addition, we evaluate the effect of outliers by removing them from the dataset. Finally, the effect of potential errors of the model input parameters is discussed.

The direct and diffuse components of *SDR* have a different meaning for simulation and observation because the model considers only the theoretical direct beam, i.e., what remains from the extraterrestrial solar beam after extinction by the atmosphere, and the totality of the light diffused by the atmosphere in the downward direction. On the other hand, the measured direct beam is in reality the sum of the direct beam and the radiation diffused within the instrument viewing angle. Similarly, the measured diffuse radiation is in reality all the radiation diffused downward minus the diffuse radiation coming from the direction obscured by the shading disk. Such a difference in meaning may explain some of the discrepancies between model results and observations. It also would explain why on average the diffuse radiation is overestimated by the model, and the direct radiation underestimated by the model.

As mentioned previously, two significant changes in the measurement methods occurred in summer 2002. A more accurate shading system mounted on a sun tracker was installed for the diffuse *SDR* observation. This resulted in an additional dataset available in parallel to the original *SDR* observation (section 4.2.a). Furthermore, the number of wavelengths used to derive AOD was increased from 4 to 9 wavelengths, which led to more precise AOD estimations at 550 nm (section 4.2.b). Therefore, the time period for the study (2001–2005) was divided into two parts to allow separate analyses of the datasets. One dataset contains 20 cases from 2001 to the end of June 2002 (old shading system and AOD derived from four wavelengths), and the other dataset contains 41 cases from July 2002 to December 2005 (with both old and new shading systems that can be compared and AOD derived from nine wavelengths). Table 4.1 also provides statistical indicators of the agreement between model results and observations for the different datasets.

Concerning the global *SDR* and its direct component, restricting the analysis to the July 2002 – December 2005 dataset results in smaller median biases (-1.3 Wm^{-2} or -0.3% and -6.9 Wm^{-2} or -1.2% for global and direct, respectively). The 2.5 percentile of the bias distributions shows a decrease in magnitude of the negative differences. On the other hand, there are no significant changes in the slope and zero-intercept of the linear regression, and very little change in the RMSE. As expected, the other part of the dataset (2001–2002) shows larger median biases, some of the individual differences being in excess of 40 Wm^{-2} . The RMSE is also larger for this period. This supports the assumption that AOD derived using nine wavelengths enable a more precise calculation of the exponents and thus a more accurate estimation of the 550-nm AOD input of the model. However, there is still a negative correlation between the AOD and the relative differences between modeled and observed diffuse *SDR* (not shown).

The diffuse *SDR* is the SW radiation component for which the model - observation agreement is the poorest. We pointed out above that a part of the diffuse radiation was not included in what is called the diffuse measurement, but in the direct measurement. Since at noon in clear-sky cases the *SDR* direct component is much higher than the diffuse one, it is natural that this discrepancy has a greater relative effect on the model - observation agreement in the diffuse case. Because the two shading systems used for the July 2002 – December 2005 dataset cover different viewing angles, comparing $SDRdif_{old}$ and $SDRdif_{new}$ provides information on the effect of excluding more or less circumsolar diffuse light and allow us to estimate how much improvement is brought by using $SDRdif_{new}$. The median bias (model minus observation) for $SDRdif_{new}$ is 0.4 Wm^{-2} (0.4%). This is significantly smaller than the median bias using $SDRdif_{old}$ and looking at the same events (4.5 Wm^{-2} or 5.2%). The 2.5 and 97.5 percentiles of the bias distribution indicate a general shift of the distribution. This shift is in the expected direction, and is significant. It is actually larger than anticipated since a positive bias is expected even with the new shading system. On the other hand, there is no improvement from $SDRdif_{old}$ to $SDRdif_{new}$ in the slope and zero-intercept of the linear regression (see Table 4.1), nor any significant difference in the RMSE.

While diffuse observations using a more accurate shading system did not improve the model to observation agreement for the linear regression, it is also possible to adjust the model inputs. Diffusion and absorption by aerosol are the factors whose uncertainty may

affect the most the precision of the model diffuse and direct *SDR* computations. This is described in the model by three parameters: aerosol optical depth, single scattering albedo and asymmetry factor. The first parameter is determined by observations, but the single scattering albedo and asymmetry factor are not measured at Payerne, and default model settings are used for these. Tests were performed to estimate the influence of these parameters.

We first decreased the AOD in the model input, to artificially increase the model *SDR* direct component and decrease the diffuse component. This can mimic the effect of the circumsolar diffuse light included in the direct measurement and excluded from the diffuse measurement. Different values were tested and best agreement for the *SDR* direct component was achieved with an AOD reduction on the order of 20%. In this case, the median biases of the global, direct and diffuse *SDR* were reduced. However, the AOD-decreased model simulations did not really improve the model to observation agreement for diffuse *SDR*. Although the bias is reduced in comparison to the original setting, the correlation is diminished and the RMSE is increased to 9.6 Wm^{-2} . Furthermore, the linear regression between model and observed diffuse *SDR* is worse, the slope and zero-intercept being further from 1 and 0, respectively, than with the original model input.

We also performed tests of the sensitivity of the modeled diffuse *SDR* on changes of the single scattering albedo and the asymmetry parameter. As mentioned above, we used the model defaults (MODTRANTM tropospheric aerosol type) for these aerosol optical properties. The default single scattering albedo is on the order of 0.96 for the boundary layer aerosol, while the default asymmetry parameter is 0 (isotropic scattering, spectrally independent Henyey-Greenstein aerosol phase function). As expected, both parameters had an influence on diffuse *SDR*, while the direct component was independent of them. Decreasing the single scattering albedo leads in a decrease of the modeled diffuse *SDR*. Augmenting the asymmetry parameter generates smaller diffuse *SDR* values as well.

Such parameters may vary from case to case, and it would be possible to almost always adjust them to obtain good agreement in the diffuse *SDR* without changing the agreement in the direct component. Since there are two parameters on which we can act, the value of such an exercise is limited and we prefer to indicate the agreement obtained using the model default for the parameters we could not determine from observation. Still, based on a restricted sub-sample of events (including events yielding diffuse *SDR* in the low, middle and high range of our set of observations), the best agreement between modeled and observed diffuse *SDR* were obtained with asymmetry parameter of 0.6, and single scattering albedo values between 0.7 and 0.9.

These tests showed how valuable a determination of aerosol single scattering albedo and asymmetry parameter are for thoroughly testing radiative transfer models in such kind of studies (Michalsky et al., 2006). It also showed that the incomplete knowledge of the aerosol optical properties is a possible source of the differences between our diffuse *SDR* simulated values and the corresponding observations. Our tests showed that lower values of the single scattering albedo and higher values of the asymmetry parameter than the default ones may yield better agreement.

The impact of extreme values (outliers) is analyzed by removing events with residuals to the linear regression larger than would be expected at a 95% significance level. However, this did not improve the model to observation agreement in the diffuse case, except for a small decrease in RMSE, as expected. The diffuse *SDR* measurement is performed with a ventilated and heated pyranometer. Most of the so-called thermal offset is compensated this way (Philipona, 2002), but a small night-time offset on the order of -1.5 Wm^{-2} is still measured. Compensating such an offset would mainly change the bias, reducing it to about 3 Wm^{-2} , when using the whole 2001–2005 dataset and increasing it to about -2 Wm^{-2} , when using *SDRdiff_{new}*. The problem for the linear regression being that the observation are significantly higher than model results for high values of diffuse *SDR*, the thermal offset cannot be the source of such an effect.

We also selected cases with high humidity (relative humidity $> 80\%$ in the lower atmosphere), using the radiosounding profiles. However, the results indicate that the cases with high humidity do not show larger model to observation differences than cases with lower humidity.

For each case, we used a flat spectral albedo corresponding to the observations of the upward and downward shortwave radiation fluxes measured at the time of the studied case. In a study by Manninen et al. (2004), integrated spectral albedo values measured by AVHRR were compared to albedo values calculated with the upward and downward shortwave radiation fluxes observed at the BSRN Payerne site. Two algorithms were used to derive the satellite integrated value. One gave a value lower, and one gave a value higher than the measured broadband value at Payerne. The algorithm giving the lower value was estimated being better and the agreement was on the order of 3%.

The spectral albedo at Payerne should reflect characteristics of a rural location varying with the season. Because we had no spectrally resolved measurements of the albedo, we tried model albedo defaults for various types of surfaces, and obtained large differences between the modeled and observed reflected solar radiation. In another trial, we scaled a model default spectral albedo to obtain an integrated value corresponding to the measured upward and downward shortwave radiation fluxes. As expected, this brought the simulated upward radiation flux in agreement with observations, but this did not improve the agreement between modeled and observed *SDR*. Consequently, we used a flat spectral albedo as described above for simplicity.

Another point susceptible to influence our results is the extraterrestrial solar input. We used the model default for total sky irradiance (TSI) at the top of atmosphere (1368 Wm^{-2}). In a recent study by Gueymard (2004), a mean TSI value of 1366.1 Wm^{-2} was derived. Since the difference with the value we used is small, we do not expect it to be influential. Nevertheless, we tested this value, and no significant difference was found between the results with the two settings, the model default even yielding slightly better agreement between model and observations.

Halthore et al. (2005) observed that the overestimation of the diffuse *SDR* by the models is larger for a cloud free case with a low aerosol optical thickness (0.08 at 550 nm), than for a cloud free case with a high AOT (0.24 at 550 nm). These findings agree to some

extent with those presented here, as we found a significant overestimation of the model at low AODs (Figure 4.4) and model underestimation at higher AOD values. Furthermore, both the results of Halthore et al. (2005) and our results imply that the slope of a model to observation linear regression is below 1 and the zero-intercept positive. When taking into account the results of the comparisons using the new shading system the correlation between the model minus observation differences and the AOD model input is diminished, but still present and of the same sign (not shown).

4.7 Conclusions

Our comparisons showed that the clear-sky global *SDR* is well simulated by a model such as MODTRANTM. The model results agree with the observations within the measurement uncertainty. When looking at the *SDR* components, the direct component generally agrees relatively well, but with the median bias at the limit of the expected measurement uncertainty. Similarly, the 95% confidence interval for the slope of the model to observation linear regression is just slightly less than 1. On the other hand, the diffuse *SDR* shows poorer model to observation agreement. The median bias is larger, especially in relative terms, and the model to observation linear regression slope and zero-intercept are significantly different from 1 and 0, respectively.

We point out that the direct and diffuse measurements are different from the theoretical direct and diffuse *SDR* components, in the sense that some circumsolar diffuse radiation is included in the direct measurement and excluded from the diffuse measurement. However, the comparisons we made using two shading system covering significantly different opening angle did not demonstrate significant differences. Particularly, when using diffuse *SDR* data from the new system covering a smaller and better-adjusted opening angle, the model to observation linear regression did not yield a slope and zero-intercept closer to their ideal values of 1 and 0 than when using data from the system with the larger opening angle.

Tests of the aerosol optical properties showed that consistently varying the known AOD did also not improve the agreement in the *SDR* diffuse data, when considering the model to observation linear regression. Other aerosol optical properties such as single scattering albedo and asymmetry parameter were not known, and model defaults were used. Sensitivity studies showed that a better agreement could be obtained in diffuse *SDR* by varying these parameters. However, the lack of information on these properties and their eventual temporal cycle at Payerne forbids inferring conclusion on their actual value from this study. Better knowledge of the aerosol single scattering albedo and asymmetry parameter is the improvement with the most potential to solve the remaining discrepancies between our model calculations and the observations. Michalsky et al. (2006) presented a study where six different models are used to assess the relative agreement among the calculations and corresponding measurements. The authors use detailed observations of the AOD, single scattering albedo and asymmetry parameter derived from ground based in-situ measurements and spectral surface albedo measured with a downward looking multifilter radiometer. The average difference of measured - observed direct and diffuse *SDR* are 0.4% and 0.6%, respectively, for the calculations made with MODTRANTM. These

results are better than those presented in this study. For further studies it is highly recommended that detailed information on single scattering albedo, asymmetry parameter and spectral albedo observations be included.

Chapter 5

Empirical analysis of cloud effects on surface radiation

Using a multiyear radiation data set and an algorithm to detect and estimate clear sky radiation, an empirical analysis is performed to deduce effect of clouds on the incoming radiation at the surface. In this Chapter methods of cloud detection are limited to synoptic observations. The less stringent selection offers a larger amount of cloud cases for each of the cloud types analyzed and interesting findings help further determine the methods to apply for more detailed determination of cloud radiative properties.

5.1 Effect of all clouds on surface incoming radiation

5.1.a Method

A six years data set from January 1998 to December 2003 of all sky (*as*, all cloud and weather conditions, nighttime and daytime) global and diffuse SDR_{as} , longwave radiation (LDR_{as}), and reflected short- and longwave radiation (SUR_{as} , LUR_{as}) observation from the BSRN PAY station was selected to perform analyses of the effects of clouds on incoming radiation. The Shortwave Flux Analysis (SWFA) code (Long and Ackerman, 2000) was applied on this data set and the resulting estimated clear sky (*cs*) radiation used for the calculation of the cloud effect (CE).

The SWFA code includes tests for each 1-minute radiation measurement in a day for the detection of *cs* radiation measurements. Besides the detection of *cs* moments (see Chapters 2.4.b and 4.3), the algorithm is also designed to estimate the corresponding *cs* radiation for measurements performed under cloudy conditions. For the estimation of *cs* radiation (SDR_{cs} and LDR_{cs}) during cloudy periods the number of clear sky measurements in a day is tested. If the number of cloud free observation data points is larger than 110, SDR_{cs} for entire day is calculated with a fit. In case the number is smaller than 110, SDR_{cs} is interpolated from the closest days when the fit could be done. The detection and estimation of LDR_{cs} is derived from Brutsaert (1975) formulation and a methodology proposed by Marty and Philipona (2000). A detailed description is given by Long (2004).

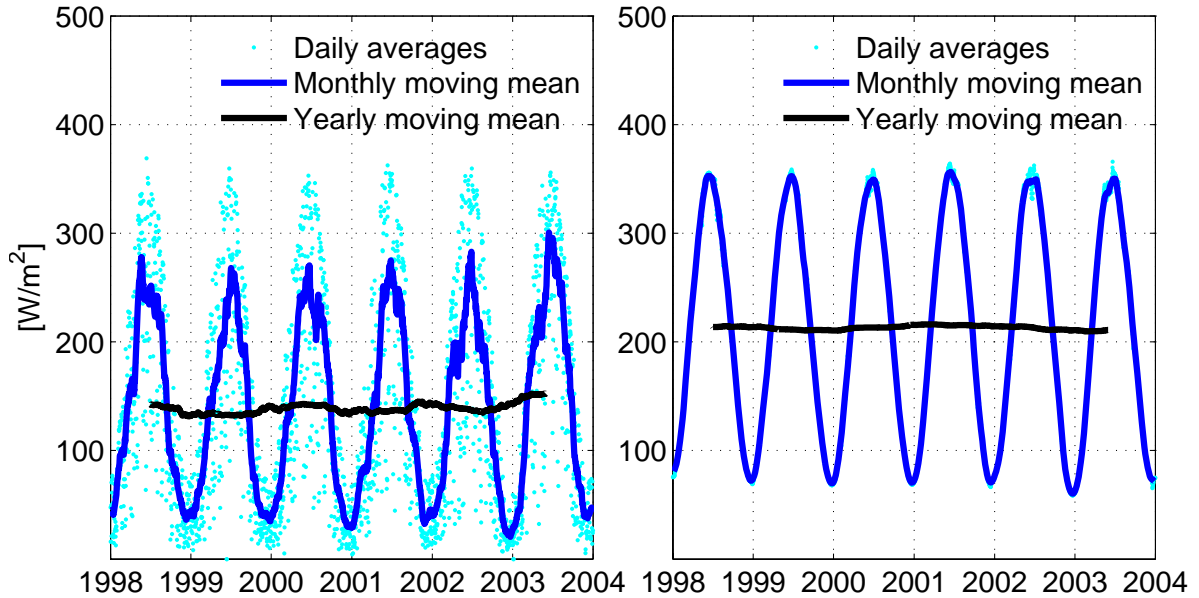


FIG. 5.1: Left side: global SDR_{as} observed at the BSRN station in Payerne, January 1998 to December 2003. Right side: clear sky estimation of the global SDR_{cs} calculated with the SWFA.

5.1.b Results and Discussion

The SDR_{as} and estimated SDR_{cs} for the data set of January 1998 to December 2003 are shown in Figure 5.1. The left panel displays daily, monthly and yearly moving average of incoming SDR_{as} , as observed at the BSRN PAY site. Daily averages of SDR_{as} exhibit considerable variations from one day to another. This is because SDR_{as} is strongly dependent on solar elevation angle and influenced by clouds. These have greatest effects during summer months. On a summer day with complete and opaque (e.g., Nimbostratus) cloud cover the daily mean SDR_{as} is very low ($< 100 \text{ Wm}^{-2}$). On the other hand, the mean SDR_{as} measured on a cloud free day in summer can rise to values on the order of 370 Wm^{-2} . In winter, maximum differences of the observed SDR_{as} between a cloudy and a clear sky day are much smaller due to the lower solar elevation.

The monthly moving average of SDR_{as} follows the solar elevation and clearly reproduces the seasonal (solar) cycle during the year. Variability is reduced by the averaging, and the highest peaks represent longer periods of fair weather with little cloudiness. An outstanding example for this can be seen during summer 2003. In this period a heat wave over Central Europe (Fischer et al., 2007) generated an exceptional fair weather period for several weeks, and therefore high SDR_{as} values. The yearly moving mean exhibits little variations, the strongest during the aforementioned summer heat wave, where many cloud free days influences the mean SDR_{as} .

The daily, monthly and yearly moving average of the clear sky estimated global SDR_{cs} is presented in the right panel of Figure 5.1. In this figure the result of the Long and Ackerman (2000) SWFA code is demonstrated. Daily variations of the SDR_{as} almost dis-

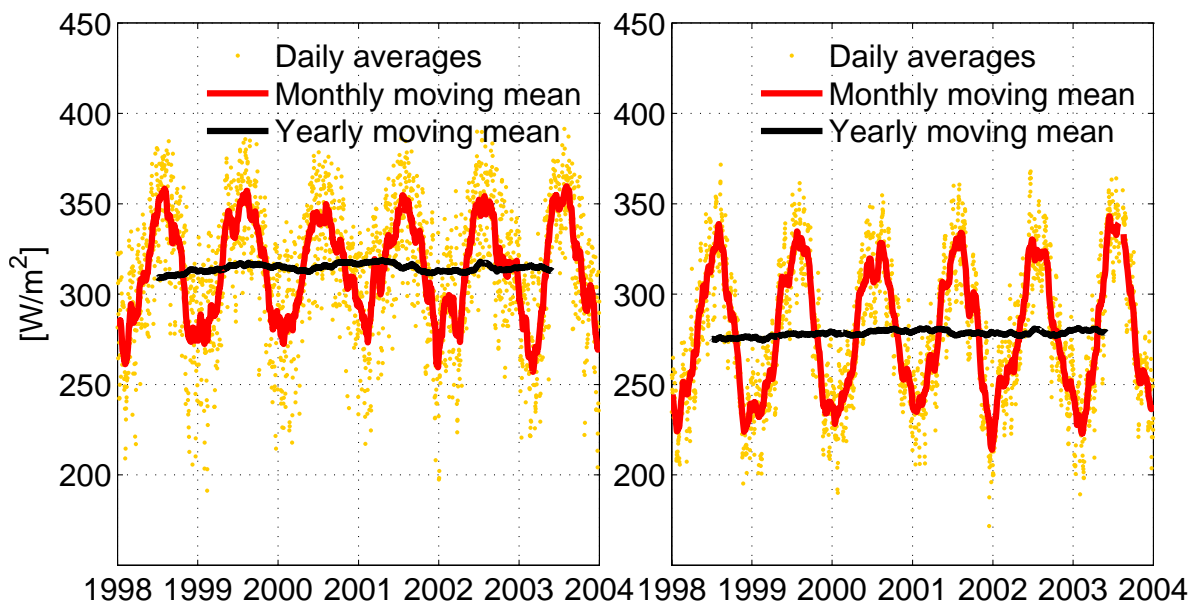


FIG. 5.2: Left side: LDR_{as} observed at the BSRN station in PAY, January 1998 to December 2003. Right side: clear sky estimation of the LDR_{cs} calculated with the SWFA.

appear and the course of the daily average of the SDR_{cs} follow the seasonal sun elevation together with the monthly moving average. Both daily and monthly averages represent a smooth line following the seasonal sun elevation cycle with little anomaly. Finally the yearly moving average is almost a straight line, indicating the longterm mean SDR_{cs} for the BSRN PAY site.

Longwave downward radiation (LDR_{as}) is the thermal radiation emitted back from the atmosphere. The left panel of Figure 5.2 shows daily means, monthly and yearly moving averages of observed LDR_{as} at the BSRN PAY site. The daily averages again show large variability, and generally higher values in summer than in winter. The variability of the daily means depend strongly on the day to day temperature, humidity and clouds variations. Furthermore, the largest part of LDR_{as} observed at surface, is emitted from the lower atmosphere, and re-emission of LDR_{as} towards surface is strongest with presence of clouds. For cloud-free situations, about 60% of LDR_{as} originate from the first 100 m, and about 90% come from the first 1000 m air column above the surface (Ohmura, 2001). Therefore, the largest daily mean values occur on summer days with high temperature and presence of low opaque clouds with high LDR emittance towards the surface. High variability is also visible in the monthly moving means. The obvious cycle with minimum in winter and maximum in summer is induced by the temperature variations which are linked to the seasonal cycle. The observed year to year variations (yearly moving mean) reflect yearly changes in temperature and cloudiness.

The estimated daily, monthly and yearly means of LDR_{cs} are shown in the right panel of Figure 5.2. Daily mean variations are again due to daily temperature changes. Also the moving monthly means of LDR_{cs} reflect well the yearly temperature cycle. The yearly

average LDR_{cs} is not as smooth as the SDR_{cs} yearly moving average and its variations can mostly be attributed to temperature influence.

The yearly amplitude of SDR_{cs} is larger compared to the amplitude of the observed SDR_{as} , meaning that maximum global SDR is occurring with clear sky situations. The mean observed SDR_{as} for the period analyzed is about 141 Wm^{-2} , the corresponding estimated mean SDR_{cs} is 213 Wm^{-2} . The cloud effect on the global SDR is calculated by subtracting the mean SDR_{cs} from the mean SDR_{as} . Thus, in PAY, clouds are responsible for a 72 Wm^{-2} average reduction of shortwave incoming radiation.

The yearly mean of LDR_{cs} is smaller than the yearly mean of the observed LDR_{as} . Removing the cloud effect results a decrease in LDR_{cs} . The mean observed LDR_{as} for the same period is 314 Wm^{-2} , the corresponding estimated mean LDR_{cs} is 278 Wm^{-2} . The cloud effect on the incoming LDR is calculated in the same way as for SDR . Therefore cloud are responsible for a 36 Wm^{-2} increase of longwave incoming radiation.

Finally, the all sky cloud effect (CE_{as}) on the incoming SDR and LDR could therefore be calculated as follows:

$$CE_{as} = (SDR_{as} - SDR_{cs}) + (LDR_{as} - LDR_{cs}) \quad (5.1)$$

Therefore, the average net effect of all cloud situations on the incoming net radiation is a 36 Wm^{-2} reduction for the BSRN PAY site.

5.2 Effect of selected cloud types on surface incoming radiation

To further determine the effect of single cloud types on the incoming radiation a cloud classification was made with the help of the synoptical observations made at PAY all three hours day and night (Chapter 2.3.b). Cases with 100% cloud coverage of a cloud type for the same data set of radiation observations as presented above were analyzed. The synop observation has to be reported in a time window covering 45 and 15 minutes before the time stamp in the synop report (e.g., the 12 UTC report is performed anytime between 11:15 and 11:45 UTC). Therefore these 30 minutes of radiation observations were selected to calculate the cloud effect for a chosen cloud type

5.2.a Selection of cloud types

Out of the 10 main cloud classes according to WMO, four stratiform low- and middle-level cloud types were selected for this study. These are stratus nebulosus, altostratus opaquus (the sun disk is not discernable), altostratus translucidus (the sun disk is distinguishable) and nimbostratus.

Nimbostratus is a dark cloud with high optical thickness and low- to middle-level cloud base. It is often seen in the center of low pressure situations, and often accompanied by precipitation. Cloud thickness reaches some km, often vertically covering large part of the troposphere. Normally, the sun is completely invisible through the nimbostratus (Müller, 1982).

Altostratus translucidus generally covers the entire hemisphere with a evenly gray layer (Müller, 1982). In the case of altostratus translucidus the sun appears through the cloud as through a depolished glass. The base varies between 3000 and 6000 m agl, therefore it is part of the middle level cloud classes (see Chapter 2). It can be observed in combination with an approaching warmfront. The altostratus opaquus is the thicker form of translucidus, the sun disc is not distinguishable any more. It covers also large parts of the hemisphere and is part of cloud systems occurring with warmfronts and occlusions.

Stratus is a low-level cloud, generally containing only water. The mostly uniform cloud base varies between 0 - 1000 m agl (when the base touches the ground, and visibility is lower than 1 km it is defined as fog), and is often observed in combination with high pressure situation over Switzerland (Müller, 1982). The geometrical thickness reaches few 100 m, the average cloud thickness found for the studies in Chapters 3 and 6 is on the order of 300 m, the maximum found is about 770 m. Drizzle, ice prisms or light snow may fall out of a stratus nebulosus.

5.2.b Results

The calculation of the cloud effect for the selected cloud types is done in two different manners. One is the use of equation 5.1 and looking separately at SDR and LDR effect. Another method is to normalize the cloud effect to avoid the confusing yearly cycle that is expected. Therefore the normalized $SDRn_{ce}$ and $LDRn_{ce}$ are calculated as follows:

$$SDRn_{ce} = (SDR_{as} - SDR_{cs})/SDR_{cs} \quad (5.2)$$

$$LDRn_{ce} = (LDR_{as} - LDR_{cs})/LDR_{cs} \quad (5.3)$$

The normalization of the absolute SDR_{ce} and LDR_{ce} by the corresponding SDR_{cs} and LDR_{cs} is performed to obtain comparable dimensionless numbers and to cancel the solar cycle. On the other hand, equations 5.4 and 5.5 represent a partition of equation 5.1 and give the cloud effect on SDR and LDR in Wm^{-2} :

$$SDRa_{ce} = (SDR_{as} - SDR_{cs}) \quad (5.4)$$

$$LDRa_{ce} = (LDR_{as} - LDR_{cs}) \quad (5.5)$$

Figure 5.3 shows the normalized $LDRn_{ce}$ (panel *a*) and $SDRn_{ce}$ (panel *b*) for stratus nebulosus calculated according to equation 5.2 and 5.3 respectively. The lower two panels *c* and *d* represent the absolute CE calculated according to equation 5.4 ($SDRa_{ce}$) and 5.5 ($LDRa_{ce}$). The large number of situations found in the data set is due to consideration of all synop observations (day and night), and no elimination of the multilayer situations. As mentioned before, surface observations with emphasis on 100% cloud cover, allow only detection of the lowest cloud layer. If the selected cloud type additionally is a low-level cloud type like stratus nebulosus, the probability is enhanced of including multilayer situations with undetected clouds above the stratus (e.g., cirrus, altocumulus).

As can be seen in Figure 5.3 most of the stratus nebulosus situations can be observed during autumn winter and early spring. The normalized effect on incoming LDR (panel *a*)

Figure 5.3) exhibits a seasonal cycle. It is influenced by the temperature cycle. The cases in summer exhibit a generally low relative CE (< 0.25) because the difference between the sky temperature under clear and cloudy conditions is significantly smaller than in winter. This effect is not canceled by the normalization. On the other hand, the cloud effect on incoming SDR shown in panel *b* of Figure 5.3 does not exhibit a yearly cycle in relative term. Case to case variations are due to cloud optical thickness, pressure (that influences Rayleigh scattering), and humidity (influences aerosol properties and cloud droplet size).

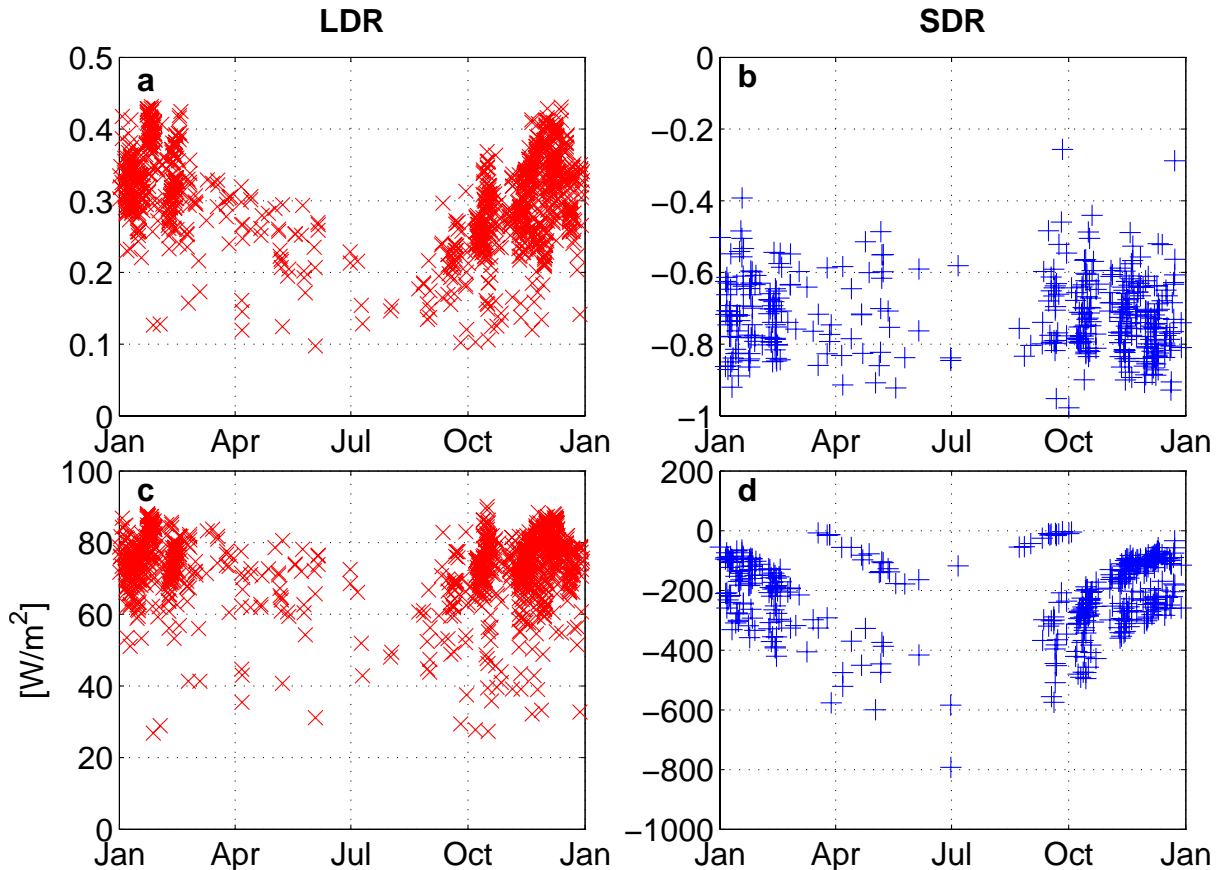


FIG. 5.3: Effect of stratus nebulosus on surface LDR (left side) and SDR (right side). In panels *a* and *b* the normalized cloud effects are displayed, in panels *c* and *d* the effect in Wm^{-2} . The night time cases for the SDR are not shown but are accounted in the calculation of the cloud effect.

For absolute CE , panels *c* and *d* in Figure 5.3 exhibit the inverse pattern: $LDRa_{ce}$ shows no distinct cycle whereas the $SDRa_{ce}$ shows a yearly cycle with largest differences corresponding to the period with highest solar elevation angle. Additionally SDR effects show clusters with changing solar elevation angle during the day. This is due to the regular time stamps when the sample are selected.

In the panels *b* and *d* of Figure 5.3 the night time cases are not shown for the SDR because they are zero by definition. They would show small differences to the 0-line because of the thermal offset described in detail by Philipona (2002), and mentioned in Chapter 4. Thermal offset is small when clouds are present and higher during clear sky conditions. However the cases left out in the plots are indeed considered in the calculation

of the net cloud effect on the incoming irradiance and a small bias is introduced.

Equation 5.1 was applied to the stratus nebulosus cases shown in Figure 5.3. This cloud type has a slight mean cooling effect on the incoming irradiance (Table 5.1). The warming effect on LDR is overcompensated by the cooling effect on the SDR .

Finally, we also computed the CE for the stratiform cloud types mentioned above. The reason only stratus nebulosus are shown on a Figure is that the other cloud types did not offer enough cases to analyze the yearly cycle. Especially when the cases are displayed for SDR , it is difficult to give details about a pattern. The results for stratus nebulosus, nimbostratus, altostratus opaques and altostratus translucidus are given in Table 5.1.

TABLE 5.1: Cloud effect [Wm^{-2}] on incoming SDR and LDR for different selected stratiform cloud types.

Cloud situation	effect on SDR	effect on LDR	net effect on $SDR + LDR$
Stratus nebulosus	− 76.2	+ 72.8	− 3.4
Nimbostratus	− 53.2	+ 72.9	+ 19.7
Altostratus opaques	− 55.2	+ 62.9	+ 7.7
Altostratus translucidus	− 59.7	+ 52.8	− 6.9

The results displayed in Table 5.1 show that different stratiform cloud types have a different net effect on the incoming radiation. The strongest warming effect comes from nimbostratus. Stratus nebulosus has the smallest negative effect. Altostratus opaques and translucidus tend to cancel each other, resulting in a slight warming effect ($< 1 \text{ Wm}^{-2}$). Taken all together, these four cloud types have a net warming effect (17 Wm^{-2}) on LDR and SDR when cases with 100% sky cover are considered. On the other hand, when all cloud situations are considered (CE_{as} , see section 5.1.b) a net cooling effect on the incoming radiation is found. But the four cloud types selected here represent a small subset of the entire cloud cases within the dataset. CE_{as} includes a large amount of scattered and multilayer cloud situations which have an important impact on the CE_{as} . In addition other cloud types such as cumulus and cirrus may have a different net effect. The net warming result of the CE of the four types can therefore not directly be compared to the CE_{as} net cooling effect.

The differences of CE of the different cloud types are due to diverse causes. The cloud types differ from each other by frequency of occurrence, cloud optical thickness, vertical extent, and altitude, to mention only the major distinctions. Nimbostratus and stratus nebulosus have a very similar increasing effect on LDR (both on the order of 73 Wm^{-2}). However the effect on SDR is not what we would expect (we would expect more SDR reduction by nimbostratus compared to the stratus nebulosus). The mean global SDR observed for the presented stratus nebulosus cases is 31.4 Wm^{-2} , the mean global SDR for the cases with nimbostratus is 9.4 Wm^{-2} . Also the cs estimation of the SDR for the two cloud types differ considerably, with 107.6 Wm^{-2} and 62.5 Wm^{-2} for stratus nebulo-

sus and nimbostratus respectively. These differences are due to the different frequencies, season and timing of occurrence. More cases were found for stratus nebulosus leaving more possibilities for high daytime SDR_{cs} values and low corresponding observed SDR , therefore provoking the larger difference for the SDR_{cs} .

The lower values for the effect of altostratus translucidus on LDR (Table 5.1) is more evident to explain. It is due to the cloud thickness, which is lower than for altostratus opaquus (as the sun disk is discernable), and therefore emitting less LDR towards the surface.

5.3 Conclusion

The study presented in this chapter, reveals that clouds have a mean cooling effect on the order of 36 Wm^{-2} on the incoming irradiance. The empirical analysis demonstrates that different stratiform cloud types have different effects on SDR and LDR , and it is sometime difficult to explain these differences.

Additionally this study was performed using only surface measurements and an algorithm to deduce information of these measurements. One of the weak points is that no information of the sky above the analyzed cloud layer was used. It must be assumed that in several cases of the separate cloud types analyses, multilayer clouds were present. Especially in case of stratus nebulosus it is highly probable that other clouds were present above the observed low cloud layer. Therefore it is difficult to make a precise analysis of the effect of a single cloud type.

The study gives an estimation of the effect of all clouds under all conditions (1 to 8 octas) on the incoming SDR and LDR for the PAY site. It is an interesting information, even though the influence of the clouds on the the longwave and shortwave upward radiation had to be omitted. This latter point is difficult to assess with an empirical algorithm.

The emphasis on different cloud types confirmed that CE is not on the same order for each of the selected stratiform cloud types. But it also revealed the difficulties and deficiencies of such empirical analyses. It helped focusing the work on specified studies with RTM MODTRANTM and single layered cloud situations. The following Chapter includes detailed studies about the radiative transfer and absorbance in stratus clouds.

Chapter 6

Radiation transfer in stratus clouds at the BSRN Payerne site

Daniela Nowak^{1, 2}, Laurent Vuilleumier¹, and Atsumu Ohmura²

Published in *Atmospheric Chemistry and Physics Discussion*, 8, 11453-11485, 2008

In this Chapter the results and findings of the previous Chapters are synthesized for achieving the main goal of the thesis. The methods for the definition and detection of stratus cloud situations are completed and additional data from satellite observations are introduced for the radiation transfer calculations.

MODTRANTM simulations allow matching of the modeled and observed surface and top of atmosphere solar radiation. The benefits of the findings about cloud detection, determination of the cloud extent and about the performance of RTM MODTRANTM are combined to infer cloud radiative properties such as absorbance and reflectance.

ABSTRACT

Clouds represent a major source of uncertainty in understanding climate change, because potential changes in the way they affect the atmospheric and surface energy budget are difficult to predict. It is therefore important to determine how clouds affect radiation. Stratiform clouds in particular have an important effect on climate as they cover large areas. This article presents results of radiation transfer calculations with MODTRANTM for well-defined stratus cloud cases detected at the meteorological station of Payerne, Switzerland. These stratus situations are selected in a data set covering the years from 2000 to 2005 with a method using data widely available at national meteorological observing stations. For 18 single layer stratus situations the shortwave radiation fluxes

¹Federal Office of Meteorology and Climatology MeteoSwiss, Payerne, Switzerland

²Institute for Atmospheric and Climate Science, ETH Zurich, Switzerland

calculated with MODTRANTM are compared to surface observations from the Baseline Surface Radiation Network (BSRN) site at Payerne and top of atmosphere (TOA) observations from the Clouds and the Earth's Radiant Energy System (CERES) experiment. A median bias on the order of 20 Wm^{-2} ($< 9\%$) was found for the differences between modeled and observed reflected solar radiation at TOA. At the surface, good agreement is obtained by adjusting the vertical extinction in the modeled cloud layer within reasonable limits for a stratus cloud: The median bias of modeled minus observed shortwave downward radiation is well within instrument precision ($< 1\%$). The simultaneous agreement of modeled and observed radiation fluxes at the surface and TOA confirmed that radiation transfer in the atmosphere including a single cloud layer can be well simulated with MODTRANTM. Based on the present results, the absorbance was calculated within the stratus cloud layer (cloud top to cloud base). For the 18 single stratus layer situations the median absorbance is 0.07 [minimum 0.04, maximum 0.1], the median transmittance is 0.29 [0.15 0.39], and the median cloud reflectance is 0.70 [0.63, 0.80].

6.1 Introduction

Clouds cover approximately 60% of the earth's surface (Heymsfield, 1993), and they play a major role in the evolution of climate. The properties of clouds most important for climate are those that affect radiation and precipitation, namely, cloud height, thickness, horizontal extent and horizontal variability, water content, cloud phase, as well as the size of droplets and ice crystals. Therefore it is important to determine how clouds affect the radiation, while distinguishing the different types of clouds (Warren and Hahn, 2002). Stratus, Stratocumulus, altostratus and cirrus clouds are thought to have the greatest effect on climate as they cover large areas. Stratus and stratocumulus cover an area of 34% over ocean surface and 18% of the land surface (Heymsfield, 1993). On average, clouds tend to have a cooling effect on climate (Somerville et al., 2007). But, effects of clouds remain a major source of uncertainty in the simulation of climate changes (e.g., aerosol indirect effect, cloud lifetime effect, response of cloud cover to increasing greenhouse gases, Trenberth et al., 2007).

Many studies were performed using detailed cloud observations and radiation measurements. Special emphasis was given to the so called cloud absorption anomaly (CAA, Li et al., 1999). Collocated satellite and surface measurements of solar radiation showed significantly higher solar absorption by clouds than anticipated, resulting in about 25 Wm^{-2} more absorption than predicted by theoretical models (global mean, Cess et al., 1995). Two experiments were performed (Atmospheric Radiation Measurement Enhanced Short-wave Experiment - ARESE - and ARESE II) in order to determine the reasons for the systematic underestimation of the cloud absorption by the models (Valero et al., 2000; Ackerman et al., 2003). With help of the ARESE II data sets, Li (2004) demonstrated that no significant CAA was observed when accounting for observation and modeling uncertainties, and that it was largely an artifact. Studies like ARESE and ARESE II often include few very well determined cloud cases over a short period of time. For studying the radiative effects of clouds it is difficult and expensive to obtain the requested datasets over long time periods. However, for single layered stratiform cloud types, methods can be developed for calculating their effect on radiation using standard meteorological observations combined with satellite observations.

This paper presents results of radiation transfer calculations with MODTRANTM for well-defined stratus cloud situations selected in a data set covering 2000 to 2005. These cloud situations are selected with a method using data widely available at national meteorological observing stations such as the MeteoSwiss Payerne aerological station (PAY). The data include surface weather observations (synops), radiosonde data and weather maps, as well as radiation observations from the PAY Baseline Surface Radiation Network (BSRN) station for model comparisons and validation. Our goal is achieving a sufficiently accurate description of the radiation transfer in the atmosphere (including a cloud layer) so that calculated radiation fluxes match both surface and top of the atmosphere observations. This study allows the determination of transmittance, absorbance and reflectance, while focusing on single layered stratiform clouds, more precisely on stratus nebulosus, which often occur during stable winter conditions at PAY.

TABLE 6.1: List of the used variables with their source information and time resolution, and a reference for further details. FMCW: Frequency Modulated Continuous Wave. Synop: human eye observations.

Observation	Source	Time resolution	Reference
Cloud-base height	Synop	3 h	Müller (1982)
	Vaisala CT25K ceilometer	30 s	Nowak et al. (2008a)
Cloud-top height	Radiosonde Meteolabor SRS 400	12h	Wang et al. (1999)
	FMCW Cloud radar	30 s	Nowak et al. (2008a)
Cloud cover	Synop	3 h	Müller (1982)
Temperature, humidity, and pressure profile	Radiosonde Meteolabor SRS 400	12 h	Miloshevic et al. (2006)
Synoptic situation	MeteoSwiss weather map	1 d low	MeteoSwiss
Surface <i>SDR</i>	Kipp & Zonen CM21 Pyranometer, BSRN	1 min	Ohmura et al. (1998)
Top of atmosphere <i>SUR</i> cloud information	CERES	~3 h	Wielicki et al. (1996)
	MERIS		Fischer et al. (2000a)

6.2 Observation techniques

The PAY aerological station (46.812°N, 6.942°E, 491 m asl), located in the Swiss Plateau between the Jura Mountains and the Alps, is operated by the Federal Office of Meteorology and Climatology (MeteoSwiss). Atmospheric observations are performed operationally following World Meteorological Organization (WMO) standards. For the selection of cloud cases, determination of cloud boundaries and for model to observation comparisons of surface radiation, official meteorological observations and BSRN radiations measurements from PAY were used. Additionally, the cloud case selection was confirmed with surface observations of La Chaux-de-Fonds (CDF, 47.083°N, 6.792°E) at 1060 m asl and Jungfraujoeh (JFJ, 46.547°N, 7.985°E), at 3580 m asl. Table 6.1 gives a list of the observations used in this study.

Because of the long time period considered, different sources of information were available at different time for specifying the status of the atmosphere. For a short time period (3 months during winter 2003 / 2004) an intensive measurement campaign including a cloud radar provided a dataset allowing comparison of the cloud-top detection used in this study with cloud radar defined cloud-top heights (Nowak et al., 2008a, and Chapter 3). Since November 2003 ceilometer data is available to define the cloud-base height, which can be compared to the heights determined by surface weather observers.

6.2.a Synop

Surface weather observations (synop), including cloud information are performed every 3 hours at PAY, starting at 00 UTC. Cloud cover, type and base height are reported for the three main cloud levels (low, middle, high clouds) as well as the horizontal visibility (Müller, 1982). Despite their subjective character and variations from one observer to another these observations (synop) are very important for climatologists and meteorologists (Dai et al., 2006). These human eye observations are generally of excellent quality and give regular and important information to meteorologists about the state of the sky, the meteorological conditions (fog, snow, rain etc.), and the horizontal visibility.

6.2.b Radiosounding

Balloon-borne meteorological radiosoundings including pressure, temperature and humidity profiles are measured twice a day at 12 and 00 UTC. They are launched at 11 and 23 UTC respectively, an hour before the designated time, in order to account for the balloon ascent. Operational radiosoundings are made with the SRS 400 (Richner, 1999; Ruffieux et al., 2006) sonde. In addition radiosoundings with the Snow White dew point hygrometer (Miloshevic et al., 2006) are available at irregular time intervals.

6.2.c Weather map

The daily synoptic weather situation for Switzerland and Europe is published on a weather map including the distribution of the atmospheric pressure, fronts and information on the cloud situation, wind, sunshine duration, relative humidity and precipitation at 12 UTC. The 500 hPa geopotential height is given including wind direction and strength. Additionally, meteorological observations of several observation stations of the measurements network from MeteoSwiss are included on these weather maps for 06, 12 and 18 UTC. A satellite image (Meteosat) is shown for 12 UTC, as well as the PAY radiosonde ascent for the 00 and 12 UTC temperature and humidity profiles. The satellite imagery, even if of low resolution, gives valuable additional information on the cloudiness seen from top of the clouds.

6.2.d Radiation

One of 39 operative BSRN radiation observation sites (Ohmura et al., 1998) spanning over the globe is located at PAY. High quality shortwave and longwave surface radiation flux measurements are performed at a high sampling rate. Diffuse and global shortwave downward radiation (*SDR*) are measured with shaded and unshaded Kipp & Zonen CM21 pyranometers, respectively, at a sampling rate of 1 Hz. One-minute mean values are recorded, as well as the sample minimum and maximum values, and the sample standard deviation. The pyranometers for the diffuse and global *SDR* measurements are ventilated and heated. In addition, the instruments are calibrated at the World Radiation Center (WRC) at Davos, Switzerland and are regularly compared with reference instruments using recent calibration from the WRC. The errors of the global and diffuse *SDR* have been estimated for BSRN PAY for a one year measuring period (October 2004 - October 2005) (Ruckstuhl, 2008). The monthly mean error (RMSE) of the global *SDR* measured

with an unshaded CM21 is about 1.6% (2.3 Wm^{-2}) with a bias of about -2.3 Wm^{-2} . More details on the radiation observations at BSRN PAY and the instruments settings are given by Nowak et al. (2008b) and in Chapter 4.

6.2.e Cloud radar

During the COST 720 Temperature, hUmidity and Cloud (TUC) experiment performed at PAY from 15 November 2003 to 15 February 2004 (Ruffieux et al., 2006), a Frequency Modulated Continuous Wave (FMCW) cloud radar was operated for determining cloud boundaries. In some stratus cloud cases used in this study, the cloud-top height was determined using cloud radar data. The height of the upper boundary determined by the cloud radar was compared with the height of this boundary determined using humidity radiosounding profiles. The method to determine the cloud upper boundary and results of the comparison are described in section 6.3. Further information on this method and its performance are provided by Nowak et al. (2008a) and in Chapter 3.

6.2.f Ceilometer

Since the beginning of the TUC experiment, in November 2003 cloud-base information inferred from ceilometer data is available for PAY. From November 2003 to August 2004, a Vaisala CT25K ceilometer was operational at PAY. Afterwards ceilometer data was retrieved from a nearby military airport (about 4 km from PAY), where the same type of ceilometer is operated at each end of the runway. When available, ceilometer data were used to provide cloud-base height. In the other cases, the information from the synop observations was used. Cloud-base detection with ceilometers is described by (Nowak et al., 2008a, and Chapter 3) and Kollias et al. (2004).

6.3 Case selection and cloud boundaries detection

Stratus nebulosus is a low-level cloud that is frequent at PAY, especially during the winter half year. It occurs either in combination with strong and stable high pressure conditions situated north of the Alps, together with easterly winds on the Plateau, or with the center of the high pressure being located over Switzerland and the Alps (Schüepp, 1979). In both cases, a distinct temperature inversion can be observed at the altitude where the cloud top is located. While the stratus layer over the Swiss Plateau hardly dissipates during the day, fair weather conditions dominate in the Jura Mountains and in the Alps (Hack, 2006). In such cases, it is possible to find single layered stratus cloud situations.

Surface observations (synops) are used for the primary selection of the cloud cases. Observations performed at 12 UTC were considered, including stratus nebulosus only at coverage of 8 octas (100%). A known limitation is the restriction to the lowest cloud layer in the case of multilayer clouds with full sky coverage of the lowest layer. As the focus of this study is on low-level single layered stratus clouds, the surface observations of CDF and JFJ were used for verifying the absence of clouds above the cloud layer detected at PAY. Only situations where CDF and JFJ observations include 0 or 1 octa of clouds were chosen. The daily synoptic weather map was verified with a focus on the atmospheric pressure distribution over Switzerland and Central Europe. The pressure distribution

at the surface was used for verification of the general weather situation. The emphasis was set on stable high pressure conditions over Switzerland and the Alps. Under these conditions single layered stratus nebulosus situations most commonly occur.

The radiosounding profile was used to determine the cloud-top height (Wang et al., 1999; Dong et al., 2000). Cloud layers were identified as regions with a relative humidity above a given threshold, and cloud upper boundaries were determined by finding sudden decrease in relative humidity (Nowak et al., 2008a, and Chapter 3). In two cases, data of the FMCW cloud radar could be used for the cloud-top height detection. The limitation to two cases is due to the restriction for the cloud type and definition (single layer, noon observation, coincidence with satellite observation) and to the short operational period of the cloud radar at the PAY site. However, Nowak et al. (2008a, see also Chapter 3) did not follow the above mentioned restrictions, and they could confirm on a larger data set (25 independent cases), the validity of the radiosounding profile method for determining the cloud upper boundary. In their study, they found an average difference between the radiosounding and cloud radar determination of the cloud upper boundary of 53 m (radiosounding – cloud radar).

In the majority of the cases, the cloud lower boundary was inferred from the synop observations. However, for cases after 15 October 2003, ceilometer data were available for cloud-base determination, and also allowed verification of the synop observation method. The agreement between the cloud-base height detected with ceilometer data and the height reported in the surface observations is on the order of 25 m (median difference for 39 stratus cases found for this study or the study presented by Nowak et al. (2008a, see also Chapter 3). Note that the altitude of the cloud base is measured by the ceilometer exactly above the instrument, but not for the surroundings; whereas the surface observations represent a mean altitude of the stratus covering the hemisphere. If the cloud base is not totally homogenous, large differences may occur between the local ceilometer data and the hemispherical synop observation.

6.4 Satellite observations

Clouds and the Earth's Radiant Energy System (CERES) experiment satellite instruments were developed for the National Aeronautics and Space Administration (NASA) Earth observation system (EOS). CERES represents an investigation to examine the role of cloud–radiation feedback in the earth's climate system (Wielicki et al., 1996). The instruments are flown aboard the Tropical Rainfall Measuring Mission (TRMM) and on the EOS Terra and Aqua satellites. The CERES instrument consists of a three channel scanning broadband radiometer, which uses precision thermistor bolometers to achieve radiometric measurements with high accuracy and stability. The instrument's field of view is of 20 km (about a factor 2 smaller than for the Earth Radiation Budget experiment). Three spectral channels measure the thermal radiation emitted from the earth's surface in the 8 - 12 μm window, the shortwave broadband 0.2 - 5 μm and total broadband 0.2 - 100 μm radiation. The CERES product used in this study is the Clouds and Radiation Swath (CRS) for the period of December 2000 to December 2005. This product includes CERES observed TOA fluxes, cloud properties derived by the CERES team from MODIS

pixels collocated within the larger CERES footprints, and the results of a fast radiation transfer code for each CERES footprint included in the file. More information on this product is given by Charlock et al. (1997) and Rutan et al. (2001). The reflected solar irradiance observed at the top of atmosphere (TOA) was used for comparison with our model results. Cloud properties given in the CRS include information on cloud fraction, cloud type and phase (water/ice). These variables were used for confirming that the CERES instrument observed conditions similar to single layered stratus cloud situations, which we assume in our model.

For a short time period, data from the Geostationary Earth Radiation Budget (GERB) project (Harries et al., 2005) were available. GERB is a highly accurate, visible-infrared broadband radiometer designed to operate on a spinning geostationary satellite to make measurements of the reflected solar and emitted thermal radiation from the Earth (Harries and Crommelynck, 1999). The GERB instrument is in operation on the first Meteosat Second Generation (MSG) satellite. Total broadband reflected radiation (0.32 - 100.0 μm), shortwave reflected radiation (0.32 - 4.0 μm), and longwave emitted radiation (4.0 - 100.0 μm by subtraction of SW from total) observations are available. The data used in this study is the High Resolution (HR) product provided over a grid size of 3 x 3 SEVIRI pixels (i.e. 9 x 9 km at nadir). Fine scale estimates of the broadband radiances from SEVIRI are combined with GERB observations (44.6 km x 39.3 km at nadir) to produce the GERB HR data. The HR values are provided each 15 minutes as an instantaneous value at the time of the SEVIRI observation. Observations collocated with the PAY station are available since February 2004. During the period from February 2004 to December 2005 four situations were found answering our requisites for model simulations and model to observation matching at surface and top of atmosphere.

For few stratus cases, observations of the medium-spectral resolution imaging spectrometer (MERIS) were available, and used for a verification of the cloud type (classified according their height and optical thickness) and cloud albedo (Fischer et al., 2000a,b). Especially the cloud type information was valuable for verifying that the selected case is a single cloud layer situation.

6.5 Radiation Transfer model MODTRANTM

MODTRANTM is a state of the art column radiative transfer model to calculate shortwave and longwave radiation fluxes at the Earth's surface or at any other point in the atmosphere from the UV (0.2 μm) to the thermal infrared (>100 μm). The version used for this study is MODTRAN5v2r11TM (called MODTRANTM in this paper for convenience). For detailed information about MODTRANTM and the range of applications see Berk et al. (1998, 2003).

The performance of a former MODTRAN4TM release for clear-sky radiation transfer at PAY has been tested in a previous study of cloud free situations at noon (Nowak et al., 2008b, and Chapter 4). In the study of the cloud free situations, the diffuse *SDR* was found to be generally overestimated by the model (median bias 4.5 Wm^{-2}), and the model to observation linear regression slope and zero-intercept were found to differ significantly

from their ideal values of 1 and 0. However, better agreement was obtained when restricting the data set to cases where model 550nm aerosol optical depth input is inferred from observations using nine spectral channels, and BSRN observations were performed with a new and more precise shading disk and sun tracker system. In this case, the median bias between model simulations and observed diffuse SDR was -0.4 Wm^{-2} ($< 1\%$).

Beside the introduction of a cloud layer, the description of the atmospheric state and the incoming radiation were developed similarly for this study and the previous one concerning clear-sky radiation. A detailed description of the model settings for SDR calculations is given by Nowak et al. (2008b, see also Chapter 4), including the method for calculating CO_2 and O_3 concentrations and the implementation of the temperature, pressure and absolute humidity profile.

With respect to the previous study of clear-sky radiation transfer, the main difference in the model setup is the introduction of a cloud layer. In the present study, a single uniform stratus cloud layer is used. Cloud-base height is determined using synop observation or ceilometer data as described in section 6.3. The cloud geometrical thickness is derived from the cloud-base height and determination of cloud-top height using radiosounding profiles or cloud radar data (see section 6.3). In the MODTRANTM framework, model properties determining the simulation of radiation transfer in cloud are the cloud liquid water droplet vertical extinction [km^{-1}] (hereafter called cloud vertical extinction), and the water droplet vertical column density [km g m^{-3}]. None of these parameters are routinely available at PAY. Consequently, the model default settings of these two parameters for stratus clouds were used for initial model simulations. Then, the vertical cloud extinction was adjusted within limits adequate for stratus cloud, in order to minimize the differences between modeled and observed surface diffuse SDR . Such an adjustment seemed legitimate since there were no measurements available to determine this parameter, and the agreement found between model and observation in our former study (Nowak et al., 2008b, and Chapter 4) demonstrated the good skill of the model at least for clear-sky radiation transfer.

6.6 Results

6.6.a Surface radiation

In our data set covering the years from 2000 to 2005, we found 32 independent cases where a single stratus cloud layer could be unequivocally identified at the time of the noon radiosonde launching (11 UTC) using the information described in sections 6.2 and 6.3. For these cases, we could simulate the transfer of radiation through the atmosphere (including the single cloud layer). As mentioned above, the first simulation was performed using the stratus clouds default model settings for describing the cloud layer between the lower and upper boundaries determined as described in section 6.2. The modeled diffuse SDR values are compared with a 5-minute mean of the measurements around this simulated time t (11 UTC in this case). The mean is calculated from the minute-averaged observed radiation from t minus 2 minutes to t plus two minutes. In 13 of the 32 cases, a difference on the order of, or less than 10 Wm^{-2} was found between the

TABLE 6.2: Statistical indicators of the agreement between model simulation and observations for the data sets at surface and top of atmosphere (TOA): a) surface diffuse shortwave downward radiation (*SDR*) measurements at 11 UTC, b) surface *SDR* measurements at the CERES observation time for possible CERES TOA observation matching, and c) TOA reflected shortwave radiation from CERES. For each data set: number of cases, correlation (R^2), median bias in Wm^{-2} and % (the 2.5 and 97.5 percentiles are indicated in brackets), RMSE in Wm^{-2} and %, slope and zero-intercept of model to observation linear regression (95% confidence intervals for the slope and zero-intercept are indicated in brackets).

Data set	Nr. of cases	R^2	Median [Wm^{-2}]	Median [%]	RMSE [Wm^{-2}]	RMSE [%]	Slope	Zero Intercept
a) Surface 11 UTC	32	0.97	0.6 [-15.9 16.3]	0.5 [-11.6 14.6]	7.2	6.2	0.93 [0.84, 1.02]	7.4 [-2.3, 17.0]
b) Surface CERES valid	18	0.96	-0.1 [-25.5 23.2]	-0.2 [-16.4 23.6]	12.5	10.1	0.84 [0.70, 0.97]	16.8 [0.6, 33.0]
c) TOA CERES	18	0.96	20.0 [-3.3 58.3]	8.9 [-1.4 21.4]	28.3	10.7	0.96 [0.82, 1.09]	35.3 [-4.5, 75.2]

simulated and observed values. In the remaining cases, we checked whether it was possible to obtain a better agreement in adjusting the vertical cloud extinction within a reasonable range for stratus clouds (40 to 80 km⁻¹). In a study presented by Lindberg et al. (1984) profiles of the extinction within stratus clouds were obtained with lidar returns from ground based measurements and spectrometers and a point visibility meter carried aloft by a tethered balloon. Their extinction values within the stratus cloud vary between the aforementioned limits with a maximum extinction on the order of 100 km⁻¹. Since we do not have measurements of the vertical extinction, it is reasonable to adjust this model parameter within the range observed by Lindberg et al. (1984), in order to obtain a good agreement between model results and observation at the ground. In case a subsequent reasonable agreement is obtained between model results and satellite observations at TOA, we can conclude that the MODTRANTM simulation of radiation transfer in the atmosphere including the cloud layer is satisfactory. Such adjustment of an unobserved cloud property for obtaining good agreement between simulated radiation fluxes and the corresponding observations was also applied in other studies (Dong et al., 2000; Ackerman et al., 2003). After such an adjustment, it was in all cases possible to reduce the difference to be on the order of, or less than 17 Wm⁻². Table 6.2 provides different statistical indicators of the agreement between model simulations and observations.

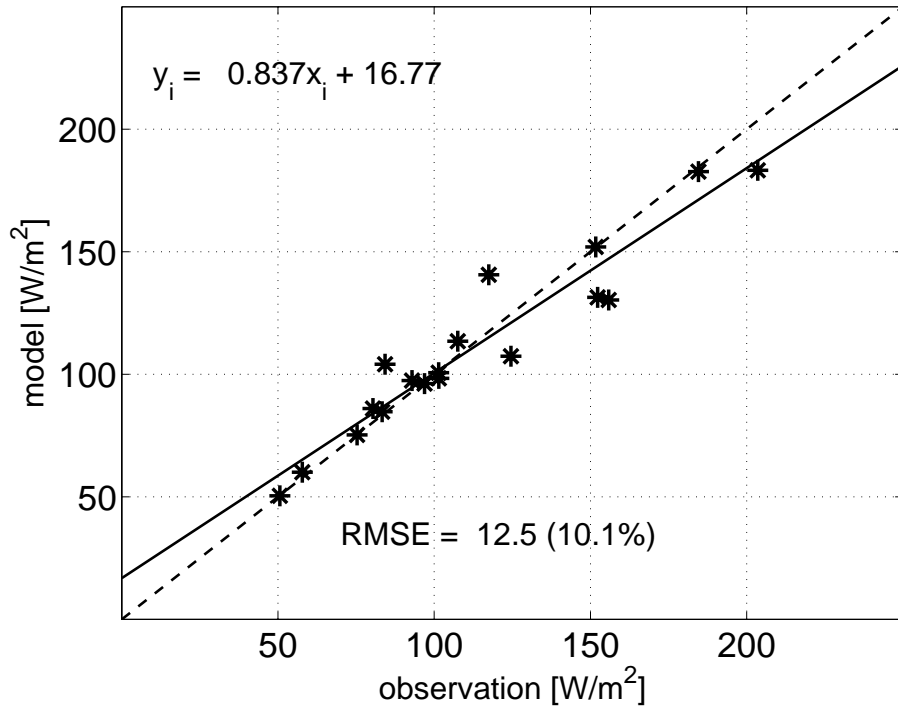


FIG. 6.1: Modeled versus observed surface *SDR*, 18 cases each calculated at the time of CERES satellite observation over Payerne. The correlation is on the order of 0.96.

6.6.b Top of atmosphere reflected radiation

As stated in the introduction, we aim at achieving a description of the radiation transfer in the atmosphere, including a single cloud layer, in a sufficiently accurate manner so that the calculated radiation fluxes match observed values both at the surface and at the top of

the atmosphere. For 31 of the 32 cases studied here, CERES observations of the reflected shortwave radiation at the top of atmosphere (later referred to as SUR_{toa}) were available within a ± 1 h window around the radiosonde launching time. However, the simulation results exhibited large discrepancies with the SUR_{toa} CERES observations (large positive bias in the modeled minus observed SUR_{toa}).

Two reasons were found that can explain such discrepancies. First, in some cases, the viewing zenith angle between the CERES instrument and the PAY station is large, which results in large uncertainties in SUR_{toa} . Restricting this angle to values below 40° further restricted the data set to 18 cases, which show a better agreement, but still have significant differences. Second, the CERES observation time is within a ± 1 h window with respect to the radiosonde launching time, but generally a time mismatch remains. The most important effects arising from this time mismatch are differences in solar zenith angle and in the characteristics of the cloud layer. In our stringent cloud selection, several criteria privileged stable situations. Thus, in most of the cases, the cloud layer should not evolve significantly between the time of radiosonde launching and the time of CERES observation, but changes in the location of the cloud upper and lower boundaries, as well as the cloud vertical extinction can occur.

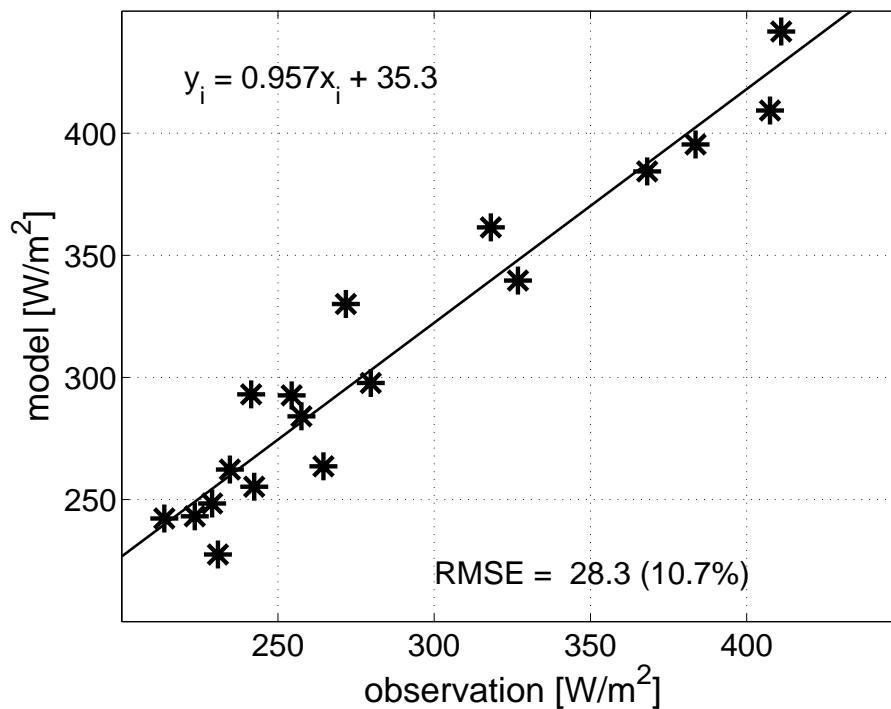


FIG. 6.2: Modeled versus observed top of atmosphere reflected shortwave radiation, 18 cases each calculated at the time of CERES satellite observation over Payerne. The correlation is on the order of 0.96.

We performed new simulation at the time of the CERES observation for the 18 cases where both the top of atmosphere and surface radiation flux simulation results could be compared with observation. These new results were compared with the 5-minute mean of surface observation around this time (similarly to section 6.6.a). In order to compen-

sate the possible evolution of the cloud layer between the time of radiosonde launching (determination of the cloud layer altitude) and the time of simulation, the cloud vertical extinction was adjusted within reasonable limits (30 to 85 km⁻¹) in order to obtain a good agreement between the surface *SDR* model calculation and observation. In 12 of the 18 cases an agreement better than ± 10 Wm⁻² was obtained, while in the other cases differences up to ± 25 Wm⁻² remained. As mentioned in section 6.6.a, this adjustment was performed within limits compatible with observations from Lindberg et al. (1984), and is reasonable given the absence of measurements of this parameter at PAY, and given the fact that we obtain a satisfactory agreement at TOA, while adjusting for agreement at the surface.

Figure 6.1 shows a comparison between modeled and observed surface *SDR* for the 18 cases described in the previous paragraph, using the CERES observation time. Again, Table 6.2 provides different statistical indicators of the agreement between model simulations and observations. It can be seen that the majority of the simulation results could be well adjusted to the observation, but some cases present relatively significant differences. The correlation (0.96) is high, and the median bias (-0.11 Wm⁻² or -0.22%) is well below the instrument precision, which is expected, because the simulation is adjusted to yield a good agreement in this quantity. However, the slope of the regression line and its zero-intercept are 0.84 and 16.8 Wm⁻², respectively, and are significantly different from their expected value of 1 and 0 (see Table 6.2). It is due to the fact that the majority of outliers are significant model underestimation for cases featuring high *SDR* observation: On Figure 6.1, four of the seven cases with *SDR* observation above 110 Wm⁻² are significantly below the X=Y line.

The model simulation values of the reflected shortwave radiation at the TOA (*SUR_{toa}*) for the 18 studied cases are compared to corresponding CERES observations in Figure 6.2, and the related statistical indicators are also listed in Table 6.2. The agreement between simulation values and CERES observation is relatively good. The correlation remained as high as for surface radiation fluxes (0.96), but a more significant positive median bias is present (20.0 Wm⁻² or 8.9%). Furthermore, the 5 to 95 percentile range of the model minus observation difference distribution just includes zero. Even though the sample is small, there seems to be a systematic positive bias between the model results and the CERES observation. On the other hand, the slope and zero-intercept of the regression line (0.96 and 35.3 Wm⁻², respectively) demonstrate the satisfactory agreement between model and observations, for they are compatible with their expected values of 1 and 0 at the 95% confidence level (see Table 6.2). In addition to the CERES observations, preliminary values for *SUR_{toa}* observations by the GERB HR product (see section 6.4) have been made available, but are not yet released for publication. In four cases, GERB observations could be compared with our simulations and differences less than 21 Wm⁻² were found for all these cases.

6.6.c Cloud absorbance, transmittance and reflectance

The results presented above show that radiation transfer in the atmosphere including a single cloud layer can be well simulated with MODTRANTM using our best knowledge of the atmospheric state derived from the data presented in sections 6.2 and 6.3, and reason-

able assumptions for the parameters that were not measured. In addition, we showed in a previous study (Nowak et al., 2008b, and Chapter 4) that the radiation transfer model we use also performed well in simulating transfer in a non-cloudy atmosphere.

Therefore the absorbance and reflectance of stratus cloud single layers can be inferred from our simulations using the calculated fluxes at the surface, the top of atmosphere and at the cloud boundaries. The shortwave absorbance and transmittance, as well as reflectance were calculated for the 18 cases where the matching with CERES observation at TOA was possible. Furthermore, the good performance of MODTRANTM for these 18 cases lead us to also compute absorbance and reflectance for all the 32 cases where single stratus cloud layers could be unequivocally identified, regardless of the availability of TOA observations. However, in the latter case, the time of radiosonde launching was used as simulation time, because it allowed a better cloud description.

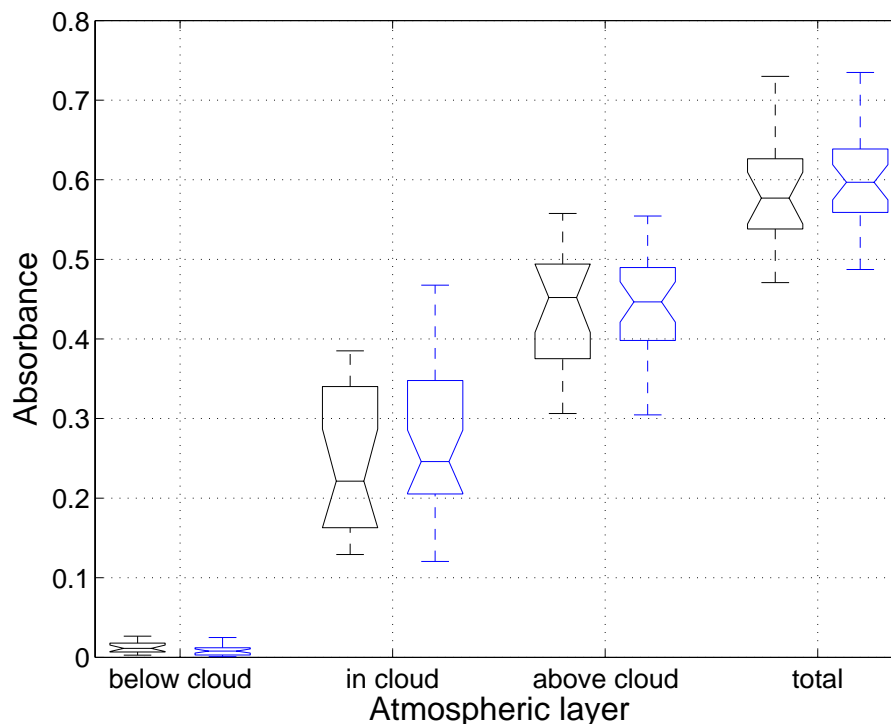


FIG. 6.3: Box plot for the shortwave absorbance in the atmospheric layer between surface and cloud base (below cloud), within the cloud (in cloud), between cloud top and top of the atmosphere (above cloud) and for the entire atmosphere (total). The black box plots represent absorbance for the 18 cases with CERES time of observation, and the blue box plots represent the absorbance for the 32 cases calculated for 11 UTC (radiosounding launch time).

For determining the absorbance A in an atmospheric layer, we first calculated the net shortwave radiation flux (SNR) at the layer boundaries by subtracting the shortwave upward radiation (SUR) from the shortwave downward radiation flux (direct + diffuse SDR): $SNR = SDR - SUR$. SNR is calculated from model simulated flux at the surface (sfc), cloud base (cba), cloud top (cto) and top of atmosphere (toa). We then calculated the absorbance A similarly to Valero et al. (2000). The absorbance of the cloud layer is therefore calculated as:

$$A_{cld} = \frac{SNR_{cto} - SNR_{cba}}{SDR_{cto}}. \quad (6.1)$$

The transmittance τ is then obtained as:

$$\tau = \frac{SDR_{cba}}{SDR_{cto}}, \quad (6.2)$$

therefore as the ratio of the incoming radiation at the lower and upper boundary of an atmospheric layer. These calculations were performed for the following layers: above cloud (acl, from toa to cto), cloud (cld, from cto to cba), below cloud (bcl, from cba to sfc), and for the whole atmosphere (all, from toa to sfc). The reflectance r of a layer is the ratio of outgoing flux and incoming flux at the top of the selected layer ($r = SUR/SDR$). In this study, r is calculated for the cloud top (cto) and for the whole atmosphere at TOA (all). The median, minimum and maximum values of absorbance, transmittance and reflectance are given in Table 6.3. Finally, besides the absorbance it is interesting to calculate the absorbed irradiance (absorption) in the cloud layer in Wm^{-2} . We calculated the absorption as Oreopoulos et al. (2003) by subtracting the net flux (SNR) at cloud base from SNR at cloud top.

Figure 6.3 presents box plots summarizing the distribution of absorbance for the 18 cases where matching with CERES observation was possible (black box plots), and for the whole 32 cases where the model runs were performed at radiosounding launching time (blue box plots). While the absorbance below the cloud layer is almost negligible, the median absorbance in the cloud is 0.07 varying between 0.04 and 0.1 for the 18 CERES cases. For the entire remaining atmosphere above the cloud, the absorbance is about 2 to 3 times higher with a median of 0.18, and minimum and maximum values of 0.13 and 0.23. Figure 6.4 presents box plots summarizing the distribution of transmittance for the 18 cases (CERES, black box plots), and for the 32 cases (11 UTC model runs, blue box plots). While the transmittance below the cloud layer is almost 1, and is on the order of 0.8 (0.72 to 0.86) above the cloud layer, it goes down to about 0.3 (0.15 to 0.39) for the cloud layer. Ideally, the absorbance, reflectance and transmittance of an atmospheric layer should add to 1 (ideal case with albedo being 0). When the median values of these parameters are added, the result for the layer below cloud (bcl) is significantly larger than for the ideal case ($A + r + \tau = 1.17$). However for the cloud layer (cld) and the entire atmosphere (all) the addition results in 1.06 and 1.04, respectively.

The absorption depends on the solar elevation, cloud geometrical thickness and cloud droplet characteristics, such as number concentration, and the size distribution. As mentioned before, no information about cloud droplet characteristics was available for this study, therefore model default were assumed for these characteristics, except that the vertical extinction was adjusted where necessary. The main absorption within the cloud is due to molecular absorption between the cloud particles, the cloud particles however promote absorption by increasing the optical path lengths of radiation due to scattering. For the 18 CERES cases the mean absorption is on the order of 28 Wm^{-2} varying between 13.7 and 51.7 Wm^{-2} . Below the cloud, approximately 1 Wm^{-2} is absorbed [minimum 0.2 Wm^{-2} , maximum 4 Wm^{-2}], and $91 [60, 111] \text{ Wm}^{-2}$ above the cloud top to the TOA.

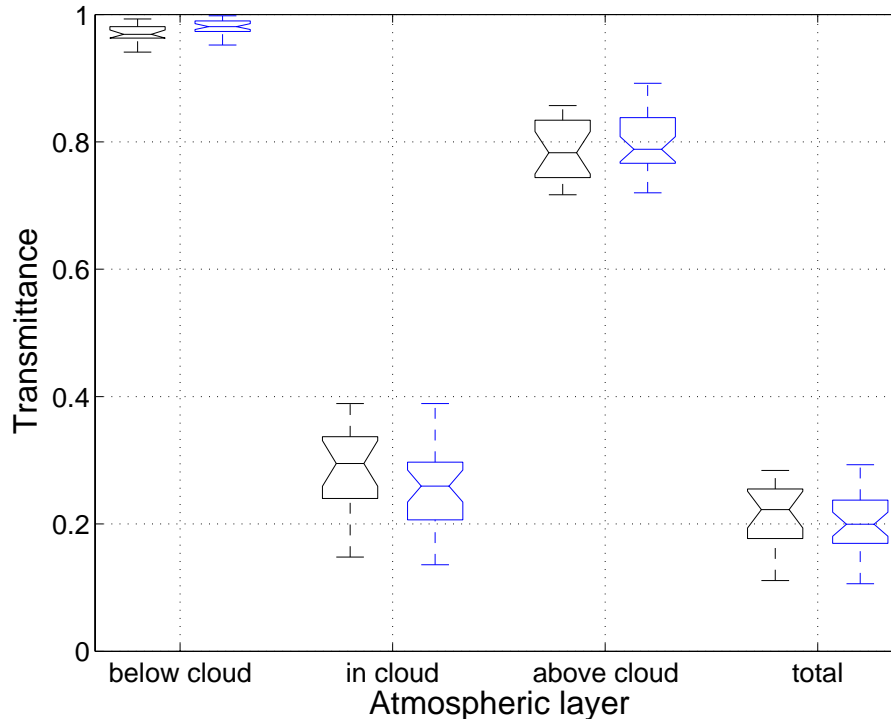


FIG. 6.4: Box plots for shortwave transmittance in the atmospheric layer between surface and cloud base (below cloud), within the cloud (in cloud), between cloud top and top of the atmosphere (above cloud) and for the entire atmosphere (total). The black box plots represent transmittance for the 18 cases with CERES time of observation, the blue box plots represent the transmittance for the 32 cases calculated for 11 UTC (radiosounding launch time).

6.7 Discussion

The performance of MODTRANTM in simulating radiation flux at the surface for an atmosphere including a single stratus cloud layer was satisfactory. The atmosphere was defined in large part using observations at the site as model input. Similarly, the cloud layer elevation and extent were derived from observations, but no information was available to define the other cloud optical properties. Nonetheless, it was possible to obtain an agreement between modeled and observed surface *SDR* within instrumental uncertainty in about a third of the 32 cases considered. For the rest of the cases, it was possible to obtain comparable agreement by adjusting the cloud vertical extinction within reasonable limits for a stratus cloud.

TOA radiation flux measurements by the CERES satellite instruments that were suitable for comparison with our model simulations were found in 18 of the 32 cases. However, for sensible comparison we had to use the CERES observation time for both our simulations and surface radiation observations. This resulted in an increased mismatch with the time of the observations used to derive the cloud layer elevation and extent. Consequently, additional uncertainty was introduced, and we had to adjust the cloud vertical extinction for a larger fraction of the cases. Nonetheless, a reasonably good agreement was obtained for the 18 CERES cases while keeping the adjusted cloud vertical extinction within limits reasonable for a stratus cloud. The slope of the linear regression between the simulated

TABLE 6.3: Median, minimum and maximum values of the 18 valid CERES cases for the absorbance A and transmittance τ in the atmospheric layers below cloud (bcl), in cloud (cld), above the cloud (acl) and the entire atmosphere from surface to toa (all). The same information is given for the reflectance r , at the surface (sfc) the top of the cloud (cto) and the top of the atmosphere (toa).

	A , median	min	max	τ , median	min	max	r , median	min	max
bcl	0.009	>0.00	0.02	0.97	0.94	0.99	sfc 0.19	0.16	0.27
cld	0.07	0.04	0.10	0.29	0.15	0.39	cto 0.70	0.63	0.80
acl	0.18	0.13	0.23	0.78	0.72	0.86	-	-	-
all	0.23	0.20	0.26	0.22	0.11	0.28	toa 0.59	0.53	0.66

and observed SUR_{toa} is compatible with 1.

On the other hand, we found a mean error (RMSE) of 10.7% and a bias on the order of 20 Wm^{-2} . Loeb et al. (2007) performed consistency tests comparing CERES TOA fluxes of the same scene from different viewing geometries. These TOA fluxes are not direct observations, but results from the application of angular distribution models on measurements. For overcast low clouds, they found a consistency of 8.5% that can be compared with our flux error. This seems lower than the RMSE and bias we found. But it should be emphasized that such error determination is difficult to compare with our results: We analyze 18 independent cases at a defined time, and the issue of the accuracy regarding a single CERES footprint is a problem difficult to address. Error can only be established for averages of views, and not for a single view. Our RMSE and the consistency found by Loeb et al. (2007) seem on the same order. On the other hand, the bias can be explained by the size of the CERES footprint and the geometry of our column model.

Using a column model forbids reproducing 3D effects of clouds. The footprint for the CERES products includes parts of the nearby Jura Mountains and foothills of the Alps. These regions exhibit strongly different topographies than the PAY station. Since our study focuses on situations where the cloud deck is generally low, it must be assumed that the Jura and the Alps foothills often stick out of the stratus cloud layer. When these regions are not snow-covered, this can have an important influence on the reflectance (albedo) and therefore on the SUR_{toa} satellite observations. Instead of the uniform cloud we assume in the model, the footprint also includes in such case the much darker ground surface, resulting in a model overestimation of SUR_{toa} satellite observations. However, the Jura and Alp foothills are relatively low (on the order of 1500 m asl), and we would expect such overestimation to be more important when the clouds are lower. But differences between the modeled and observed SUR_{toa} do not show any correlation with increasing cloud-top height or vertical extent as can be seen in Figure 6.5.

Stratus nebulosus is a cloud type that can exhibit large variations in cloud extent, cloud droplet concentrations, optical depth and liquid water path (Dong et al., 2000). In the 32 stratus cases presented in this study, the cloud extent varied between 130 and 600 m, with cloud bases between 55 and 660 m, and cloud tops between 310 and 1180 m above the ground. The absorbance values found in our study are comparable to those found in other

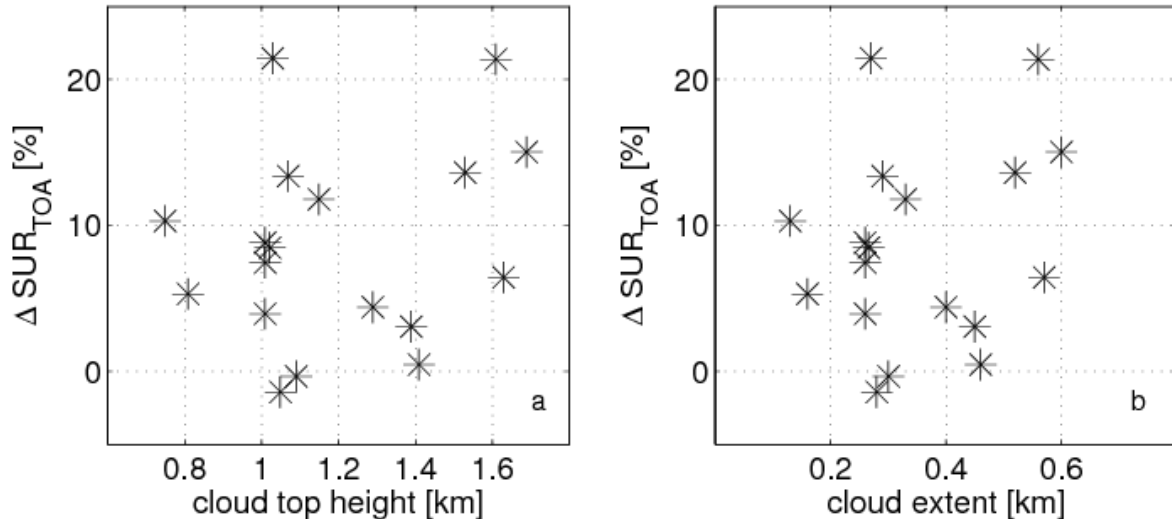


FIG. 6.5: The relative differences of modeled minus observed SUR_{toa} for the 18 CERES cases compared to the cloud-top height (a) and the cloud vertical extent (b).

studies (Oreopoulos et al., 2003; Ackerman et al., 2003), if we use the same layer limits than used in these studies. In order to compare our results to those obtained in other studies, comparisons were made with the model inferred absorbance and transmittance values for the same atmospheric layer as presented in these studies. In these two studies, the absorbance is inferred using surface measurements or measurements from an aircraft flying below the cloud and measurements from an aircraft flying above the cloud (7 and 13 km for ARESE and ARESE II, respectively). We infer the absorbance for the selected layer from our model calculations. The absorbance values observed between surface observations and aircraft measurements by Ackerman et al. (2003) vary between 0.178 and 0.217 (flight averages) for three selected days of measurements. The median absorbance for the corresponding atmospheric layer obtained with MODTRANTM calculations in this study is 0.177 and varies between 0.146 and 0.203.

CERES products include the TOA reflectance. However, this does not use the same SUR_{toa} that we use for our comparisons. The SUR_{toa} values we used were directly inferred from measured radiances. However, for its TOA reflectance products, CERES uses values of SUR_{toa} and SDR_{toa} that are both consistent with their model of the atmospheric radiation transfer. Nevertheless, the median CERES-derived reflectance for the 18 cases we studied is 0.59, therefore identical to the value we deduced from our simulations. The minimum CERES-deduced reflectance was lower (0.49), while the maximum was on the same order than our determination.

6.8 Conclusions and Outlook

This study presents methods to deduce absorption, absorbance, transmittance and reflectance of solar radiation in stratiform clouds, determined with a state of the art RTM and with widely available atmospheric observations. Such observations include radiosonde profiles, synop observations, cloud remote sensing information and radiation measurements. Solar radiation flux matching between model and observations at both surface

and top of atmosphere was obtained within reasonable agreement.

The results presented in this study offer a method for the monitoring of the effect of stratiform clouds on the solar radiation. Over the globe 38 operative BSRN stations monitor the radiation at high precision. Requirements for BSRN stations result in the other type of data used in this thesis being available at all BSRN stations. Therefore this research (or similar) could be reproduced at all BSRN stations. This would already constitute a global analysis. However, the world coverage by these stations is not uniform. Since satellite measurements are included in such an analysis, they could be used for verifying that the conclusion can be extrapolated globally. Especially in a changing climate, tracking changes in radiation budgets due to potential cloud changes becomes important (e.g., changes of the stratiform cloud cover have been reported over the United States over a period from 1940 to 2002 by Sun and Groisman, 2004). Additionally cloud radiative properties may not remain constant when climate changes (Slingo, 1989).

Detailed atmospheric observations are required for improving the knowledge of the absorbance and reflectance of different cloud types. Ample data sets such as for ARESE (Valero et al., 2000) and ARESE II (Oreopoulos et al., 2003) are rare and expensive to obtain. This study demonstrates a method using an alternative data set to obtain valuable information on cloud effects on solar radiation. Therefore we highly recommend carrying on similar future studies on longer time span for more cloud types (e.g., altostratus, nimbostratus), with the help of a growing set of data (e.g., additional satellite information), and for different locations over the globe (e.g., BSRN sites with radiosonde data and synop observations).

The value of this study would have been significantly enhanced if the cloud optical properties had been available. Some cloud continuous operational monitoring with remote sensing instruments would be the most valuable addition from the point of view of such studies. Similarly, the performance of the future GERB high resolution (Harries et al., 2005) products should be noted here, which will combine the excellent radiometric performances of the GERB instrument with the finer spatial resolution of the SEVIRI imager. Unfortunately, these products are still under validation, and we urge the GERB community to release as soon as possible these very valuable data sets for publication.

Chapter 7

Conclusion and Outlook

7.1 Summary and conclusions

This thesis presents analyses of solar radiation under clear sky and overcast conditions. The aim of the thesis is to improve knowledge of the effect of clouds on *SDR*. More precisely, it is to determine cloud physical properties such as absorbance and reflectance with help of a radiation transfer model and observations. The determination of cloud situations with multiple sets of instrument is presented. Different methods are combined to deduce the cloud type and cloud extent. In order to make simulations of cloud situations with RTM MODTRANTM, the performance of the model was first verified with clear sky situations. Radiation observations of the BSRN station were analyzed with an emphasis on finding clear sky situations at noon using an empirical analysis code and surface observations. A large data set of surface observations and BSRN radiation measurements was then used to define empirically the effect of all clouds on the incoming *LDR* and *SDR* at the PAY site. Finally the detailed analyses of stratus cloud situations with RTM MODTRANTM merge methods and findings of these studies for inferring cloud absorption, absorbance, transmittance and reflectance by deterministic calculations. The following paragraphs summarize the most important findings.

7.1.a Cloud detection

The combination of a FMCW cloud radar and a Vaisala ceilometer gives valuable and continuous information on the cloud-base and -top height. These instruments complement each other. The ceilometer detects the cloud-base height at a highly reliable level (overall detection efficiency > 95%), but is not designed to also detect cloud-top height. The cloud radar detects cloud-top height, but the instrument used in this study being a prototype revealed some difficulties and a weaker performance (overall detection efficiency < 60%). On the other hand it is capable to detect higher cloud layers in case of multilayer situations.

The cloud-top height detected with the radar was compared to the cloud-top height inferred from radiosonde data. For 25 of the analyzed situations, a radiosonde profile was available concurrently with cloud radar observations. The average difference between the radiosounding and cloud radar upper boundary is on the order of 50 m, which represents a satisfying result compared to larger differences reported in a previous study (Ruffieux

et al., 2006).

This demonstrates the validity of determining the cloud upper boundary with radiosonde profiles, as is done in this study for the long term data set. Similarly, the detection of cloud base by ceilometer allowed validating the determinations made by observers.

7.1.b Clear sky model simulations

Clear sky global SDR is well simulated with RTM MODTRANTM using atmospheric data observed mostly at the PAY station and model default settings. The median of the differences between modeled and observed global SDR is small ($< 1\%$) and well within the instrument uncertainty. The agreement for the direct SDR is relatively good, but at the limit of instrument accuracy. The diffuse SDR revealed larger differences between model and observation when using observations from a Kipp & Zonen CM21 pyranometer shaded with a large disk and an old sun tracking system.

Better agreement was obtained when the model simulations were compared with diffuse SDR observations using a new shading and sun tracking system. Then, the median bias of the differences was reduced to $< 1\%$. However, the model to observations linear regression slope and zero-intercept remained significantly different from 1 and 0, respectively. Further analyzes revealed alternatives for improving the agreement of modeled and observed diffuse SDR . Including AOD single scattering albedo and asymmetry parameter for refining the AOD description in the model inputs showed the best potential for improvement. As both scattering albedo and asymmetry parameter are not observed at the PAY station, this method could not be applied.

7.1.c Effect of clouds on incoming radiation

An algorithm to detect cloud free radiation measurements is applied to a six years data set of BSRN radiation observations. The products of this algorithm contain flagged clear sky measurements and an estimation of the clear sky radiation for measurements made under cloudy conditions. The estimated clear sky radiation (SDR_{cs} , LDR_{cs}) is used for inferring cloud effect by comparison to the observed all sky radiation (SDR_{as} , LDR_{as}). Clouds reduce the net surface incoming radiation ($SDR + LDR$) by 36 Wm^{-2} at the PAY BSRN site.

The same calculation is done for selected stratiform cloud types totally covering the sky. It is found that different stratiform clouds have a different influence on the incoming radiation. Furthermore the findings helped determining how to proceed for further analyzes of the cloud radiative properties.

7.1.d Absorbance and radiative transfer in stratus clouds

The methods developed, tested and applied in the aforementioned parts of the thesis were combined for detailed analysis of the radiation transfer in well-defined stratus nebulosus situations. With help of an additional satellite data set (CERES) including observations of SUR_{toa} , simultaneous matching of the modeled and observed solar radiation fluxes

was obtained within reasonable agreement for 18 well determined stratus cloud situations from 2000 to 2005.

Therefore the absorbance and absorption of solar radiation is calculated based on the model determination of the radiation fluxes. The median absorbance between the base and top of the stratus cloud layer is 0.22, and the median absorption is 28 Wm^{-2} . An overestimation by the model of the total column absorption (TOA to surface) of 9% is found, which is within agreement of a previous study (Ackerman et al., 2003).

7.2 Outlook

Based on the findings mentioned in the precedent paragraphs, some recommendations are made for further studies:

- Continuous cloud monitoring with a ceilometer and a cloud radar as presented in Chapter 3 is highly recommended to allow more detailed studies of the effect of clouds on radiation. Promising performances can be expected from a revised version of the presented FMCW cloud radar. Additionally, it has the capability to detect higher elevated clouds above a first cloud deck. In contrast to synoptic observations and satellite measurement (e.g., MERIS), cloud radar and ceilometer offer cloud information at high temporal resolution. Combined with another method for cloud cover determination (APCADA, infrared sky scanning instrument) a precious data set could be obtained.
- The clear sky solar radiation simulations with MODTRANTM presented in Chapter 4 could substantially be improved if observations of the single scattering albedo and the asymmetry parameter were available. Such measurements are demanding and require further instruments (e.g., nephelometer), nevertheless they are very valuable for climate monitoring.
- Cloud radiative effects of stratiform clouds can be calculated if reasonable matching of model calculations and observations is obtained simultaneously at surface and at TOA. Satellite observations of the TOA radiation fluxes at high temporal resolution are needed to evaluate the agreement of the modeled fluxes. Especially the GERB high resolution products revealed promising results. When released for publication, enhanced studies with these data sets are highly recommended. In addition, information on cloud optical properties would be most valuable. Polarization techniques may allow this type of information to be obtained by remote sensing.

Finally I would like to emphasize the importance of continuous, complete and constant monitoring of the radiation and the state of the atmosphere (including cloud cover and type). A changing climate causes changes in the water vapor content, has an effect on cloud occurrence and on the radiation transfer under clear sky conditions. The aerosol indirect effect affects cloud properties by modifying the size (decrease) and number (increase) of cloud droplets, and therefore modifies the cloud albedo and lifetime.

The most profitable elements to make advances for such studies at Payerne would be continuous measurements of the aerosol single scattering albedo and asymmetry parameter,

as well as cloud droplet number, droplet size distribution and liquid water content. A new COST Action is currently designed for setting up an observation network of well instrumented meteorological stations with emphasis on continuous operational remote sensing measurements. This initiative (EG-CLIMET – European Ground-based observations of essential variables for CLImate and operational METeorology) could be a significant help for the type of research presented in this thesis.

Appendix A

Instrumental Details

A.1 Ceilometer

Data from a Vaisala CT25K ceilometer were used in this thesis. This light detection and ranging (lidar) system sends out short, powerful laser pulses (905 nm \pm 5 nm) at a frequency of 100 ns in the vertical direction (Vaisala, 2002). The principle of the CT25K ceilometer is based on measurement of the time needed for the short pulse of light to traverse the atmosphere from the transmitter of the ceilometer to a backscattering cloud base and back to the receiver of the ceilometer. Assuming a speed of light $c = 2.99 \times 10^8 m/s$ a reflection from 7620 m (25000 ft) will be seen by the receiver after $t = 50.9 \mu s$.

A.2 FMCW cloud radar

The FMCW radar has a transmitter power of approximately 120 mW. It transmits at a frequency of 78.2 GHz with a frequency modulation of approximately 10 MHz over a period of approximately 770 μs . The radar effectively measures the return of transmitted power reflected (scattered) from a cloud. Use of a frequency modulated carrier wave (FMCW or chirp) provides range information (chirp is a signal in which the frequency increases ('up-chirp') or decreases ('down-chirp') with time). The returned power is proportional to the concentration and size of particles forming the cloud and given by:

$$ReturnPower = \sum \frac{ND^6}{\lambda^4} \quad (A.1)$$

where N is the concentration and summation over all particle sizes, D is the diameter and λ operational wavelength. The advantage of operation at shorter wavelengths is an increase in returned power, or a reduction in drop size resolution for the same returned power. The range is measured simply as a result of the chirp difference frequency, i.e. between transmission and reception after a roundtrip time of flight t :

$$Range = \frac{ct}{2} \quad (A.2)$$

where c is the velocity of light. For a single plane target at a range distance R from the transmitter and receiver, the chirp difference (fd) is a tone (corresponding to the

roundtrip time) and the frequency of which is related to the chirp rate and distance by

$$R = \frac{c \cdot fd}{2B} \quad (\text{A.3})$$

where B is the chirp rate or bandwidth. The range resolution is simply:

$$\Delta R = \frac{c}{2B} \quad (\text{A.4})$$

For multiple reflections, multiple tones are returned and by a combination of digital sampling and Fourier transforming, the range information can be retrieved as a function of time and returned power. The maximum range is defined by the duration of the chirp.

Appendix B

Details on the SWFA

The following paragraphs represent a summarized extract of the paper presented by Long and Ackerman (2000). The four important steps for the determination of cloud free moments are listed and explained.

The shortwave flux analysis (SWFA) code of Long and Ackerman (2000) consist of a method to identify periods of clear skies for a 160° field of view (FOV) using 1-minute broadband measurements of surface total and diffuse *SDR*. The clear-sky detection method uses a sequence of tests that eliminates almost all periods when clouds are present in the hemispheric FOV of the instruments. Because of the cosine response of the instruments the presence of persistent, thin clouds at large zenith angles relative to the instruments is not detected (thus the limitation to 160°). This method does not detect uniform thin haze that produces an enlarged circumsolar disc. This condition of the sky can be classified as cloudy but this decision depends on the specific definition of clear sky. Cloudy skies show shortwave characteristics that clear skies do not, which can be used to separate the two situations within a data set. A series of four tests are used to eliminate data that occur under cloudy skies. Each individual test is not sufficient to determine whether the sky is clear in a given moment, thus only data that passes all tests are shown to be representative of clear skies.

The first test that is applied is to normalize the total shortwave data by a power law function of the cosine of the solar zenith angle (SZA):

$$F_N = \frac{F_\downarrow}{\mu_0^b} \quad (\text{B.1})$$

where F_\downarrow is the total *SDR*, F_N is the normalized total *SDR*, μ_0 is the cosine of the SZA, and b is a constant. Maximum and minimum limits are set, and only normalized values falling inside this range are provisorily flagged as clear.

The second test is to compare the measured downwelling diffuse irradiance to some limit. This diffuse limit is set to match the typical climatological clear sky diffuse irradiance of the instrument location, plus an amount to match an increase during typical hazy conditions. The diffuse limit is subjectively set on the basis of visual inspection of the magnitude of measured diffuse irradiance on known clear sky days in the data being processed. The choice of the limit restricts the amount of haze that is chosen as not being a cloud. The higher the limit is set, the thicker the acceptable haze. The clear sky diffuse

irradiance limit formula is based on the cosine of the SZA:

$$D_{lim} = D_{max}\mu_0^{0.5} \quad (\text{B.2})$$

where D_{lim} is the clear sky limit at the given SZA and D_{max} is a constant.

Next, the temporal change in total SDR is analyzed. For clear periods the change in irradiance is small over short periods of time compared to changes due to cloud effects. The third test compares the change in measured total SDR to the corresponding change in top of atmosphere (TOA) irradiance. The TOA irradiance is calculated as:

$$F_{\downarrow T} = S_0\mu_0, \quad (\text{B.3})$$

where S_0 is the solar irradiance constant (1365 Wm^{-2}), and $F_{\downarrow T}$ is the TOA SDR . For clear sky (ideally) the absolute change in F_{\downarrow} over a short time must be less than the absolute change in $F_{\downarrow T}$.

There are circumstances where measurements that pass these three tests are still not clear-sky measurements. The diffuse ratio (diffuse SDR divided by the total SDR) is sensitive to small changes in both the diffuse and direct SDR . Another characteristic of the clear-sky shortwave components is the smoothness of the time series. Thus the diffuse ratio can be used as a sensitive test of the variability of the measurements through time. The variation in the measurement is tested by using a normalized diffuse ratio.

$$D_N = \frac{D_{\downarrow}}{\mu_0^b} \quad (\text{B.4})$$

where D_{\downarrow} is the measured diffuse ratio, D_N is the normalized diffuse ratio, and b is a constant.

The clear sky SDR for cloudy sky observations can be estimated using an empirical fit. The primary factor that determines the magnitude of the diurnal SDR cycle for clear skies is the SZA. Thus clear-sky irradiance can be empirically adjusted (fit) using the cosine of the SZA as the independent variable. Long and Ackerman (2000) found that a simple power law equation represents well the clear-sky conditions:

$$Y = a\mu_0^b \quad (\text{B.5})$$

where Y represents the clear sky total SDR or diffuse ratio and a and b are regression coefficients. The a constant represents the clear-sky irradiance for a SZA of 0° and includes effects like e.g. the average aerosol and column water vapor amounts. The b constant includes effects like the radiometer cosine response. The regression coefficients of B.5 are determined using a least squares robust estimation that minimizes the sum of the absolute deviations. For details further see Long and Ackerman (2000) and Press et al. (1986).

List of Figures

2.1	The earth's annual global mean energy budget based on Kiehl and Trenberth (1997).	6
2.2	A stratus nebulosus seen from the top of Gurnigel in the Bernese foothills of the Alps. The well-defined cloud top and clear sky above the stratus are typical weather features for high pressure conditions during winter (Photo: D. Nowak, 2006)	8
2.3	Map of Switzerland with the meteorological station Payerne, and the three auxiliary stations Jungfrauoch, La Chaux-de-Fonds, and Arosa. . .	9
2.4	PFR, CH1 NIP and shaded Kipp & Zonen CM21 Pyranometer mounted on a BRUSAG sun tracking instrument	10
2.5	BSRN PAY bench with diffuse <i>SDR</i> and <i>LDR</i> observation system (operative since October 1992).	11
2.6	New diffuse <i>SDR</i> and <i>LDR</i> observation system at the BSRN PAY site (operative since July 2002).	12
2.7	Cloud base and cloud top retrieved with ceilometer and cloud radar 9 December 2003 at the PAY site. Example of an overcast day with low stratus nebulosus and fog alternating.	13
3.1	Upper panel: time series of cloud base (ceilometer, red dots), cloud top (cloud radar, black dots), and 2-D color time series of wind profiler signal-to-noise ratio, 9 December 2003, starting at 21 UTC of the previous day. The three rectangles with grey and purple lines correspond to the profiles measured with the radiosounding at 11 and 23 UTC (dashed line = time of sounding, purple line = temperature with a horizontal scale of 10 K, green line = humidity with a horizontal scale of 100%). Lower panel: time series of surface relative humidity (green), temperature (red), incoming short-wave radiation (blue), and horizontal visibility (black).	22
3.2	Same as FIG. 3.1, but for 19 November 2003.	24
3.3	Number of stratus cloud and fog cases detected at time of synop observations during the TUC campaign. Four groups describe all stratus cases, stratus cases without precipitation, all fog cases and fog cases without precipitation. Shaded bars from left to right: all cases detected by synop observation (black), ceilometer operative (dark grey), cloud radar operative (grey), ceilometer retrieval successful (light grey) and, cloud radar retrieval successful (white)	25

3.4	Comparison of cloud extend (cloud base from ceilometer to cloud top from cloud radar) with determination of cloud top from radiosounding humidity profile (radiosoundings include 3 types of sondes: SRS400, SnowWhite and RS80.	27
4.1	Upper panel: Observed (BSRN) diffuse SDR (solid line) with cloud free detected moments marked as crosses on the solid line, SWFA estimated clear sky SDR (dashed line). Lower panel: same as for the upper panel but for the direct SDR	41
4.2	Modeled versus observed global (a), direct (b), and diffuse (c) SDR . The correlation is 1 for the global, 0.99 for the direct SDR , and 0.98 for the diffuse SDR	42
4.3	Relative differences (%) of modeled minus observed global (a), direct (b), and diffuse (c) SDR	43
4.4	Relative differences (%) of modeled minus observed SDR versus the aerosol optical depth (AOD) used in the model calculation, for the global (a), direct (b), and diffuse (c) SDR	44
5.1	Left side: global SDR_{as} observed at the BSRN station in Payerne, January 1998 to December 2003. Right side: clear sky estimation of the global SDR_{cs} calculated with the SWFA.	52
5.2	Left side: LDR_{as} observed at the BSRN station in PAY, January 1998 to December 2003. Right side: clear sky estimation of the LDR_{cs} calculated with the SWFA.	53
5.3	Effect of stratus nebulosus on surface LDR (left side) and SDR (right side). In panels <i>a</i> and <i>b</i> the normalized cloud effects are displayed, in panels <i>c</i> and <i>d</i> the effect in Wm^{-2} . The night time cases for the SDR are not shown but are accounted in the calculation of the cloud effect. . .	56
6.1	Modeled versus observed surface SDR , 18 cases each calculated at the time of CERES satellite observation over Payerne. The correlation is on the order of 0.96.	69
6.2	Modeled versus observed top of atmosphere reflected shortwave radiation, 18 cases each calculated at the time of CERES satellite observation over Payerne. The correlation is on the order of 0.96.	70
6.3	Box plot for the shortwave absorbance in the atmospheric layer between surface and cloud base (below cloud), within the cloud (in cloud), between cloud top and top of the atmosphere (above cloud) and for the entire atmosphere (total). The black box plots represent absorbance for the 18 cases with CERES time of observation, and the blue box plots represent the absorbance for the 32 cases calculated for 11 UTC (radiosounding launch time).	72

6.4	Box plots for shortwave transmittance in the atmospheric layer between surface and cloud base (below cloud), within the cloud (in cloud), between cloud top and top of the atmosphere (above cloud) and for the entire atmosphere (total). The black box plots represent transmittance for the 18 cases with CERES time of observation, the blue box plots represent the transmittance for the 32 cases calculated for 11 UTC (radiosounding launch time).	74
6.5	The relative differences of modeled minus observed SUR_{toa} for the 18 CERES cases compared to the cloud-top height (a) and the cloud vertical extent (b).	76

List of Tables

2.1	Classification of clouds corresponding to their height and latitude. According to WMO International Cloud Atlas, 1956. For low clouds the height indicated is valid above the ground, for middle and high clouds above the mean sea level.	7
3.1	Observation techniques and instruments used for the study, operational at the meteorological station in Payerne, Switzerland (synop, radiosondes, wind profiler) and experimental for the TUC campaign (ceilometer, cloud radar).	19
3.2	Rate of cloud base and top detection, relative to the total observed situations for both systems operative during TUC in Payerne, Switzerland	26
4.1	Statistical indicators of the agreement between model simulation and observations for the three analyzed datasets: a) 2001–2005 original dataset with old diffuse shortwave downward radiation <i>SDR</i> measurement, b) 2002–2005 with old and new diffuse observation method and aerosol optical depth (AOD) measured at 9 wavelengths, c) 2001–2002 data with old shading system and AOD measured at 4 wavelengths. For each dataset: number of cases, correlation (R^2), median bias in Wm^{-2} and % (the 2.5 and 97.5 percentiles are indicated in brackets), RMSE in Wm^{-2} and %, slope and zero-intercept of model to observation linear regression (95% confidence intervals for the slope and zero-intercept are indicated in brackets).	40
5.1	Cloud effect [Wm^{-2}] on incoming SDR and LDR for different selected stratiform cloud types.	57
6.1	List of the used variables with their source information and time resolution, and a reference for further details. FMCW: Frequency Modulated Continuous Wave. Synop: human eye observations.	62

6.2	Statistical indicators of the agreement between model simulation and observations for the data sets at surface and top of atmosphere (TOA): a) surface diffuse shortwave downward radiation (<i>SDR</i>) measurements at 11 UTC, b) surface <i>SDR</i> measurements at the CERES observation time for possible CERES TOA observation matching, and c) TOA reflected shortwave radiation from CERES. For each data set: number of cases, correlation (R^2), median bias in Wm^{-2} and % (the 2.5 and 97.5 percentiles are indicated in brackets), RMSE in Wm^{-2} and %, slope and zero-intercept of model to observation linear regression (95% confidence intervals for the slope and zero-intercept are indicated in brackets). . . .	68
6.3	Median, minimum and maximum values of the 18 valid CERES cases for the absorbance A and transmittance τ in the atmospheric layers below cloud (bcl), in cloud (cld), above the cloud (acl) and the entire atmosphere from surface to toa (all). The same information is given for the reflectance r , at the surface (sfc) the top of the cloud (cto) and the top of the atmosphere (toa).	75

References

- Ackerman, T. P., D. M. Flynn, and R. T. Marchand, 2003: Quantifying the magnitude of anomalous solar absorption. *J. Geophys. Res.*, **108**. [DOI: 10.1029/2002JD002674].
- Ångström, A., 1930: On the atmospheric transmission of sun radiation. II. *Geogr. Ann. A.*, **12**, 130–159.
- Arking, A., 1991: The radiative effects of clouds and their impact on climate. *B. Am. Meteorol. Soc.*, **71**, 795–813.
- Aviolat, F., T. Cornu, and D. Cattani, 1998: Automatic clouds observation improved by an artificial neural network. *J. Atmos. Ocean. Tech.*, **15**, 14–126.
- Barnard, J., and D. Powell, 2001: Comparison of modeled and measured shortwave broadband radiative fluxes at the SGP and NSA sites (with special emphasis on diffuse radiation). Eleventh ARM Science Team Meeting Proceedings, Atlanta Georgia, 19 - 23 March.
- Bendix, J., B. Thies, J. Cermak, and T. Nauss, 2005: Ground fog detection from space based on modis daytime data - a feasibility study. *Weather Forecast.*, **20**, 989–1005.
- Berk, A., G. Anderson, P. Acharaya, M. Hoke, J. Chetwynd, L. Bernstein, E. Shettle, M. Mathew, and S. Adler-Golden, 2003: *MODTRAN4 Version 3 revised 1 user's manual*. Air Force Research Laboratory, Space Vehicle Dir., Air Force Mater, Command, Hanscom Air Force Base, Massachusetts.
- Berk, A., L. Bernstein, G. Anderson, P. Acharya, D. Robertson, J. Chetwynd, and S. Adler-Golden, 1998: MODTRAN cloud and multiple scattering upgrades with application to AVIRIS. *Remote Sens. Environ.*, **65**, 367–375.
- Boers, R., H. Russchenberg, J. Erkelens, and V. Venema, 2000: Ground-based remote sensing of stratocumulus properties during CLARA, 1996. *J. Appl. Meteorol.*, **39**, 169–181.
- Brutsaert, W., 1975: On a derivable formula for longwave radiation from clear skies. *Water Resour. Res.*, **11**, 742–744.
- Cermak, J., M. Schneebeli, D. Nowak, L. Vuilleumier, and J. Bendix, 2006: Characterization of low clouds with satellite and ground-based remote sensing systems. *Meteorol. Z.*, **15**, 65–72.

- Cess, R. D., M. H. Zhang, P. Minnis, L. Corsetti, E. G. Dutton, B. W. Forgan, D. P. Garber, W. L. Gates, J. J. Hack, E. F. Harrison, X. Jing, J. T. Kiehl, C. N. Long, J.-J. Morcrette, G. L. Potter, V. Ramanathan, B. Subasilar, C. H. Whitlock, D. F. Young, and Y. Zhou, 1995: Absorption of solar radiation by clouds: observations versus models. *Science*, **267**, 496–499.
- Charlock, T., F. G. Rose, D. A. Rutan, T. I. Alberta, D. P. Kratz, L. H. Coleman, G. L. Smith, N. Manalo-Smith, and T. D. Bess, 1997: *Compute surface and atmospheric fluxes (System 5.0). Clouds and the Earth's Radiant Energy System (CERES)*. Release 2.2 ed., Algorithm theoretical basis document (ATBD), NASA Langley Research Center, Hampton, VA, 84 pp.
- Clothiaux, E. E., T. P. Ackerman, G. C. Mace, K. P. Moran, R. T. Marchand, M. A. Miller, and B. E. Martner, 2000: Objective determination of cloud heights and radar reflectivities using a combination of active remote sensors at the ARM CART sites. *J. Appl. Meteorol.*, **39**, 645–665.
- Crewell, S., and co authors, 2004: The Baltex Bridge Campaign: An integrated approach for a better understanding of clouds. *B. Am. Meteorol. Soc.*, **85**, 1565–1584.
- Dai, A., T. R. Karl, B. Sun, and K. E. Trenberth, 2006: Recent trends in cloudiness over the United States. *B. Am. Meteorol. Soc.*, **87**, 597–606.
- Dibbern, J., W. Monna, J. Nash, and G. Peters, (Eds.) , 2003: *COST Action 76: Development of VHF/UHF wind profilers and vertical sounders for use in European observing systems - Final report*. EUR 20614, European Commission.
- Dong, X., P. Minnis, T. P. Ackerman, E. E. Clothiaux, G. G. Mace, C. N. Long, and J. C. Liljegren, 2000: A 25-month database of stratus cloud properties generated from ground-based measurements at the Atmospheric Radiation Measurement Southern Great Plains Site. *J. Geophys. Res.*, **105**, 4529–4537.
- Dürr, B., and R. Philipona, 2004: Automatic cloud amount detection by surface longwave downward radiation measurements. *J. Geophys. Res.*, **109**. [DOI: 10.1029/2003JD004182].
- Dürr, B., R. Philipona, F. Schubiger, and A. Ohmura, 2005: Comparison of modeled and observed cloud-free longwave downward radiation over the Alps. *Meteorol. Z.*, **14**, 47–55.
- Engelbart, D. A. M., W. Monna, J. Nash, and C. Mätzler, (Eds.) , 2008: *COST Action 720: Integrated ground-based remote sensing stations for atmospheric profiling - Final report*. COST Office, Brussels, in print.
- Fischer, E. M., S. Seneviratne, P. L. Vidale, D. Lüthi, and C. Schär, 2007: Soil moisture-atmosphere interactions during the 2003 European summer heat wave. *J. Climate*, **20**, 5081–5099. [DOI: 10.1175/JCLI4288.1].
- Fischer, J., L. Schiller, and R. Preusker, 2000a: *Cloud albedo and cloud optical thickness*. Algorithm Theoretical Basis Document 2.1, 2.2, Freie Universität Berlin, 31 pp.

- , 2000b: *Cloud top pressure*. Algorithm Theoretical Basis Document 2.3, Freie Universität Berlin, 28 pp.
- Gossard, E. E., R. B. Chadwick, W. D. Neff, , and K. Moran, 1982: The use of ground-based Doppler Radars to measure gradients, fluxes and structure parameters in elevated layers. *J. Appl. Meteorol.*, **21**, 211–226.
- Gossard, E. E., D. E. Wolfe, and B. B. Stankov, 1999: Measurement of humidity profiles in the atmosphere by the Global Positioning System and radar wind profilers. *J. Atmos. Ocean. Tech.*, **16**, 156–164.
- Gueymard, C. A., 2004: The sun’s total and spectral irradiance for solar energy applications and solar radiation models. *Sol. Energy*, **76**, 423–453.
- Hack, K. H., 2006: *Typische Wetterlagen im Alpenraum*. Bundesamt für Meteorologie und Klimatologie MeteoSchweiz, 23 pp.
- Halothore, R. N., D. Crisp, S. Schwartz, G. P. Anderson, A. Berk, B. Bonnel, O. Boucher, F.-L. Chang, M.-D. Chou, E. Clothiaux, P. Dubuisson, B. Fomin, Y. Fouquart, S. Freidenreich, C. Gautier, S. Kato, I. Laszlo, Z. Li, J. Mather, A. Plana-Fattori, V. Ramaswamy, P. Ricchiazzi, Y. Shiren, A. Trishchenko, and W. Wiscombe, 2005: Inter-comparison of shortwave Radiative transfer codes and measurements. *J. Geophys. Res.*, **110**. [DOI: 10.1029/2004JD005293].
- Halothore, R. N., and S. E. Schwartz, 2000: Comparison of model-estimated and measured diffuse downward irradiance at surface in cloud-free skies. *J. Geophys. Res.*, **105**, 20 165–20 177.
- Harries, J., and D. Crommelynck, 1999: The geostationary earth radiation budget experiment on MSG-1 and its potential applications. *Adv. Space Res.*, **24**, 915–919.
- Harries, J. E., J. E. Russel, J. A. Hanafin, H. Brindley, J. Futyan, J. Rufus, S. Kellock, G. Matthews, R. Wrigley, A. Last, J. Mueller, R. Mossavati, J. Ashmall, E. Sawyer, D. Parker, M. Caldwell, P. M. Allan, A. Smith, M. J. Bates, B. Coan, B. C. Stewart, D. R. Lepine, L. A. Cornwall, D. R. Corney, M. J. Ricketts, D. Drummond, D. Smart, R. Cutler, S. Dewitte, N. Clerbaux, L. Gonzalez, A. Ipe, C. Bertrand, A. Joukoff, D. Crommelynck, N. Nelms, D. T. Llewellyn-Jones, G. Butcher, G. L. Smith, Z. P. Szewczyk, P. E. Mlynchak, A. Slingo, R. P. Allan, and M. A. Ringer, 2005: The geostationary earth radiation budget project. *B. Am. Meteorol. Soc.*, **86**, 945–960.
- Henzing, J. S., W. H. Knap, P. Stamnes, A. Apituley, J. B. Bergwerff, D. P. J. Swart, G. P. A. Kos, and H. M. ten Brink, 2004: Effect of aerosols on the downward shortwave irradiances at the surface: measurements versus calculations with MODTRAN4.1. *J. Geophys. Res.*, **109**. [DOI: 10.1029/2003JD004142].
- Heymsfield, A. J., 1993: *Microphysical structures of stratiform and cirrus clouds*. Aerosol - Cloud - Climate Interactions, Academic Press Inc., 97–121 pp.
- Hollars, S., Q. Fu, J. Comstock, and T. Ackerman, 2004: Comparison of cloud-top height retrievals from ground-based 35GHz MMCR and GMS-5 satellite observations at ARM TWP Manus site. *Atmos. Res.*, **72**, 169–186.

- Illingworth, A. J., R. J. Hogan, E. J. O'Connor, D. Bouniol, M. E. Brooks, D. P. D. J. Delanoë, J. D. Eastment, N. Gaussiat, J. W. F. Goddard, M. Haeffelin, H. K. Baltink, O. A. Krasnov, J. Pelon, J.-M. Piriou, A. Protat, H. W. J. Russchenberg, A. Seifert, A. M. Tompkins, G.-J. van Zadelhoff, F. Vinit, U. Willen, D. R. Wilson, and C. L. Wrench, 2007: CLOUDNET - continuous evaluation of cloud profiles in seven operational models using ground-based observations. *B. Am. Meteorol. Soc.*, **88**, 883–898.
- Kato, S., T. P. Ackerman, E. G. Clothiaux, J. H. Mather, G. G. Mace, M. L. Wesely, F. Murcray, and J. Michalsky, 1997: Uncertainties in modeled and measured clear-sky surface shortwave irradiances. *J. Geophys. Res.*, **102**, 25 881–25 898.
- Kiehl, J. T., and K. E. Trenberth, 1997: Earth's annual global mean energy budget. *B. Am. Meteorol. Soc.*, **78**, 197–208.
- Kinne, S., R. Bergstrom, O. Toon, E. Dutton, , and M. Shiobara, 1998: Clear-sky atmospheric transmission: An analysis based on FIRE 1991 field experiment data. *J. Geophys. Res.*, **103**, 19 709–19 720.
- Kollias, P., C. Fairall, P. Zuidema, J. Tomlinson, and G. Wick, 2004: Observation of marine stratocumulus in SE Pacific during the PACS 2003 cruise. *Geophys. Res. Lett.*, **31**. [DOI: 10.1029/2004GL020751].
- Li, Z., 2004: *On the solar radiation budget and cloud absorption anomaly debate*. Observation, Theory, and Modeling of the Atmospheric Variability. World Scientific Publishing Co., 437-456 pp.
- Li, Z., A. P. Trishchenko, H. W. Barker, G. L. Stephens, and P. Partain, 1999: Analyses of Atmospheric Radiation Measurement (ARM) program's Enhanced Shortwave Experiment (ARESE) multiple data sets for studying cloud absorption. *J. Geophys. Res.*, **104**, 19 127–19 134.
- Lindberg, J. D., W. J. Lentz, E. M. Measure, and R. Rubio, 1984: Lidar determinations of extinction in stratus clouds. *Appl. Optics*, **23**, 2172–2177.
- Loeb, N. G., S. Kato, K. Loukachine, N. Manalo-Smith, and D. R. Doelling, 2007: Angular distribution models for top-of-atmosphere radiative flux estimation from the Clouds and Earth's Radiant Energy System instrument on the Terra satellite. Part II: Validation. *J. Atmos. Ocean. Tech.*, **24**, 564–584.
- Löhnert, U., S. Crewell, and C. Simmer, 2004: An integrated approach toward retrieving physically consistent profiles of temperature, humidity, and cloud liquid water. *J. Appl. Meteorol.*, **43**, 1295–1307.
- Long, C. N., 2004: The next generation flux analysis: adding clear-sky LW and LW cloud effects, cloud optical depths, and improved sky cover estimates. Fourteenth ARM Science Team Meeting Proceedings, Albuquerque, New Mexico, 22 - 26 March.
- Long, C. N., and T. P. Ackerman, 2000: Identification of Clear Skies from Broadband Pyranometer Measurements and Calculation of Downwelling Shortwave Cloud Effects. *J. Geophys. Res.*, **105**, 15 609–15 626.

- Manninen, T., N. Siljamo, J. Poutiainen, L. Vuilleumier, F. Bosveld, and A. Gratzki, 2004: Cloud statistics based on the estimation of land surface albedo from AVHRR data. *Proc. of SPIE*, **5571**, 412–423.
- Marty, C., and R. Philipona, 2000: The clear sky index to separate clear-sky situations in climate research. *Geophys. Res. Lett.*, **127**, 1641–1644.
- Michalsky, J. J., G. Anderson, J. Barnard, J. Delamere, C. Gueymard, S. Kato, P. Kiedron, A. McComiskey, and P. Ricchiazzi, 2006: Shortwave radiative closure studies for clear skies during the Atmospheric Radiation Measurement 2003 Aerosol Intensive Operation Period. *J. Geophys. Res.*, **111**. [DOI: 10.1029/2005JD006341].
- Miloshevic, L. M., H. Voemel, D. N. Whiteman, B. M. Lesht, F. J. Schmidlin, and F. Russo, 2006: Absolute accuracy of water vapor measurements from six operational radiosonde types launched during AWEX-G and implications for AIRS validation. *J. Geophys. Res.*, **111**. [DOI: 10.1029/2005JD006083].
- Müller, G., 1982: *Handbuch für Beobachter des automatischen Beobachtungsnetzes*. Schweizerische Meteorologische Anstalt (SMA).
- Nash, J., D. Lyth, and M. Oldfield, 2005: Observing fog and low clouds with a combination of 78GHz cloud radar and laser ceilometer. Proceedings of WMO Instruments and Methods Observation Programme, Technical Conference of Meteorological and Environmental Instruments and Methods of Observation Bucharest, Romania, 4-7 May 2005.
- Neff, W. D., 1990: *Atmospheric processes over complex terrain*. 45, Amer Meteor. Soc., Boston, MA, USA., 173–228 pp.
- Nowak, D., D. Ruffieux, J. L. Agnew, and L. Vuilleumier, 2008a: Detection of fog and low cloud boundaries with ground-based remote sensing systems. *J. Atmos. Ocean. Tech.*, **25**, 1357–1368.
- Nowak, D., L. Vuilleumier, C. N. Long, and A. Ohmura, 2008b: Solar irradiance computations compared with observations at the BSRN Payerne site. *J. Geophys. Res.*, **113**. [DOI: 10.1029/2007JD009441].
- O’Connor, E. J., R. J. Hogan, and A. J. Illingworth, 2005: Retrieving stratocumulus drizzle parameters using Doppler radar and lidar. *J. Appl. Meteorol.*, **44**, 14–27.
- Ohmura, A., 2001: Physical basis for the temperature-based melt-index method. *J. Appl. Meteorol.*, **40**, 753–761.
- Ohmura, A., E. G. Dutton, B. Forgan, C. Frhlich, H. Gilgen, H. H. Hegner, A. Heimo, G. Knig-Langlo, B. McArthur, G. Mller, R. Philipona, R. Pinker, C. H. Withlock, K. Dehne, and M. Wild, 1998: Baseline Surface Radiation Network (BSRN): New precision radiometry for climate research. *B. Am. Meteorol. Soc.*, **79**, 2115–2136.
- Oreopoulos, L., A. Marshak, and R. F. Calahan, 2003: Consistency of ARESE II cloud absorption estimates and sampling issues. *J. Geophys. Res.*, **108**. [DOI: 10.1029/2002JD002243].

- Philipona, R., 2002: Underestimation of solar global and diffuse radiation measured at Earth's surface. *J. Geophys. Res.*, **107**. [DOI: 10.1029/2002JD002396].
- Press, W. H., B. P. Flannery, S. A. Teukolsky, and W. T. Vetterling, 1986: *Numerical Recipes: The art of scientific computing*. Cambridge University Press, New York, 818 pp.
- Protat, A., A. Armstrong, M. H. adn Y. Morille, J. Pelon, J. Delanoë, and D. Burniol, 2006: Impact of conditional sampling and instrumental limitations on the statistics of cloud properties derived from cloud radar and lidar at SIRTa. *J. Geophys. Res.*, **33**. [DOI: 10.1029/2005GL025340].
- Quante, M., 2004: The role of clouds in the climate system. *J. Phys IV*, **121**, 61–86.
- Ramanathan, V., R. Cess, E. Harrison, P. Minnis, B. Barkstrom, E. Ahmad, and D. Hartmann, 1989: Cloud Radiative forcing and climate: Results from the Earth Radiation Budget Experiment. *Science*, **243**, 57–63.
- Richner, H., 1999: *Grundlagen aerologischer Messungen speziell mittels der Schweizer Sonde SRS 400*. 61, ISSN 1422-1381, Veröffentlichungen der SMA-MeteoSchweiz.
- Ruckstuhl, C., 2008: Surface Radiation Changes and their Impact on Climate in Central Europe. Ph.D. dissertation, ETH Zurich, Switzerland. [17578].
- Ruffieux, D., J. Nash, P. Jeannet, and J. Agnew, 2006: The COST 720 temperature, humidity and cloud profiling campaign: TUC. *Meteorol. Z.*, **15**, 5–10.
- Rutan, D. A., F. Rose, N. Smith, and T. Charlock, 2001: Validation data set for CERES surface and atmospheric radiation budget (SARB). *WCRP/GEWEX Newsletter*, **11**, 11–12.
- Schüepp, M., 1979: *Witterungsklimatologie, Klimatologie der Schweiz*. Band III, Schweizerische Meteorologische Anstalt, 93 pp.
- Slingo, A., 1989: A GCM parameterization for the shortwave radiative properties of water clouds. *J. Atmos. Sci.*, **46**, 1419–1427.
- Somerville, R., H. L. Treut, U. Cubasch, Y. Ding, C. Mauritzen, A. Mokssit, T. Peterson, and M. Prather, 2007: *Historical Overview of Climate Change*. 1st ed., Climate Change 2007: The Physical Science Basis, Cambridge University Press, Cambridge, United Kingdom and New York, NY, USA.
- Stähelin, J., A. Renaud, J. Bader, R. McPeters, P. Viatte, B. Hoegger, V. Bugnion, M. Giroud, and H. Schill, 1998: Total ozone series at Arosa (Switzerland): Homogenization and data comparison. *J. Geophys. Res.*, **103**, 5827–5841.
- Sun, B., and P. Y. Groisman, 2004: Variations in low cloud cover over the United States during the second half of the twentieth century. *J. Climate*, **17**, 1883–1888.

- Trenberth, K. E., P. Jones, P. Ambenje, R. Bojariu, D. Easterling, A. K. Tank, D. Parker, F. Rahimzadeh, J. Renwick, M. Rusticucci, B. Soden, and P. Zhai, 2007: *Observations: Surface and Atmospheric Climate Change*. 1st ed., Climate Change 2007: The Physical Science Basis, Cambridge University Press, Cambridge, United Kingdom and New York, NY, USA.
- Vaisala, 2002: Ceilometer CT25K User's Guide.
- Valero, F. P. J., P. Minnis, S. K. Pope, A. Bucholtz, B. C. Bush, D. R. Doelling, W. L. S. Jr., and X. Dong, 2000: Absorption of solar radiation by the atmosphere as determined using satellite, aircraft, and surface data during the Atmospheric Radiation Measurement Enhanced Shortwave Experiment (ARESE). *J. Geophys. Res.*, **105**, 4743–4758.
- Verver, G., M. Fujiwara, P. Dolmans, C. Becker, P. Fortuin, and L. Miloshevic, 2006: Performance of the Vaisala RS80A/H and RS90 Humicap sensors and the Meteorolabor 'Snow White' chilled-mirror hygrometer in Paramaribo, Suriname. *J. Atmos. Ocean. Tech.*, **23**, 1506–1518.
- Wang, J., W. Rossow, T. Uttal, and M. Rozendaal, 1999: Variability of cloud vertical structure during ASTEX observed from a combination of rawinsonde, radar, ceilometer and satellite. *Mon. Weather Rev.*, **127**, 2484–2502.
- Warren, S. G., and C. J. Hahn, 2002: *Clouds*. Climatology. Encyclopedia of atmospheric sciences, Academic Press, J. R. Holton, J. A. Curry, and J. A. Pyle (Editors), 476–483 pp.
- Wehrli, C., 2000: Calibrations of filter radiometers for determination of atmospheric optical depths. *Metrologia*, **37**, 419–422.
- Wielicki, B. A., B. R. Barkstrom, E. F. Harrison, R. B. L. III, G. L. Smith, and J. E. Cooper, 1996: Clouds and the Earth's Radiant Energy System (CERES): An earth observation system experiment. *B. Am. Meteorol. Soc.*, **77**, 853–868.

Acknowledgements

The present thesis was completed under the supervision of Prof. Atsumu Ohmura at the Institute for Atmospheric and Climate Science (IAC) at ETH Zurich. I would like to thank Prof. Ohmura for his supervision, for his encouragement and the numerous constructive and interesting discussions.

I am indebted to Laurent Vuilleumier who offered me the opportunity to make my PhD at MeteoSwiss, Payerne. He motivated and encouraged me to work hard whenever difficulties occurred and supported me with uncountable challenging and interesting discussions. I would like to acknowledge Pierre Viatte who responded to my application and offered the well-maintained infrastructure at MeteoSwiss. Furthermore I am thankful to the following people working at MeteoSwiss for their precious and reliable support in different stages of this thesis: Armand Vernez, Eliane Maillard, Martine Collaud, Rolf Philipona, René Stübi, Alain Heimo, Pierre Jeannet, the observer and field team, and the patient and helpful IT-team.

I especially enjoyed the collaboration with Dominique Ruffieux, Charles N. Long, and Judith L. Agnew for the paper manuscripts.

I am thankful to Gail P. Anderson at AFRL/Space Vehicles Directorate for her great and patient help with MODTRANTM. Thanks to David Rutan from Science Systems & Applications, Inc. for the CERES data supply from the NASA Langley Research Center and his valuable assistance. Thanks to Nicolas Clerboux from the Institut Royal Meteorologique, Belgium for the GERB data supply and his assistance. Thanks to Rasmus Lindstrot at Institut für Weltraumwissenschaften, Freie Universität Berlin for providing MERIS data. Furthermore I would like to acknowledge Ueli Möckli from Ruag Aerospace and the collaborators from the military airport Payerne for the access to ceilometer data. Special thanks to Christian Ruckstuhl at the IAC for his help in creating an algorithm facilitating the MODTRANTM model runs. I am also thankful to Bruno Dürr and Sebastian Hoch for their initial help with MODTRANTM.

Cordial thanks to Daniel Walker who shared the office with me at MeteoSwiss. I appreciated his encouragement not only concerning working topics, the scientific discussions and the funny moments we shared. I enjoyed the kind and supporting working environment with my colleagues at the IAC and at MeteoSwiss, Payerne.

I am thankful to my relatives Peter and Marietta Fischer for offering me a home in Zurich and encouraging me during delicious meals and unforgettable evenings.

My deepest thanks go to my mother, Ursula Nowak, and my dear companion in life, Martin Minder, for their encouragement, motivation and patience. My sincere thanks to Roland Wyss and all other friends for their support during this period.

This study was founded by the Swiss climate research programme NCCR Climate, an initiative founded by the Swiss National Science Foundation (NSF).

Veröffentlichungen der MeteoSchweiz

- 78** Arpagaus M, Rotach M, Ambrosetti P, Ament F, Appenzeller C, Bauer H-S, Bouttier F, Buzzi A, Corazza M, Davolio S, Denhard M, Dorninger M, Fontannaz L, Frick J, Fundel F, Germann U, Gorgas T, Grossi G, Hegg C, Hering A, Jaun S, Keil C, Liniger M, Marsigli C, McTaggart-Cowan R, Montani A, Mylne K, Ranzi R, Richard E, Rossa A, Santos-Muñoz D, Schär C, Seity Y, Staudinger M, Stoll M, Vogt S, Volkert H, Walser A, Wang Y, Werhahn J, Wulfmeyer V, Wunram C and Zappa M: 2009, MAP D-PHASE: Demonstrating forecast capabilities for flood events in the Alpine region. Report of the WWRP Forecast Demonstration Project D-PHASE submitted to the WWRP Scientific Steering Committee, 65pp, CHF 73.-
- 77** Rossa AM: 2007, MAP-NWS – an Optional EUMETNET Programme in Support of an Optimal Research Programme, 67pp, CHF 73.-
- 76** Baggenstos D: 2007, Probabilistic verification of operational monthly temperature forecasts, 52pp, CHF 69.-
- 75** Fikke S, Ronsten G, Heimo A, Kunz S, Ostrozklik M, Persson PE, Sabata J, Wareing B, Wichura B, Chum J, Laakso T, Sääntti K and Makkonen L: 2007, COST 727: Atmospheric Icing on Structures Measurements and data collection on icing: State of the Art, 110pp, CHF 83.-
- 74** Schmutz C, Müller P und Barodte B: 2006, Potenzialabklärung für Public Private Partnership (PPP) bei MeteoSchweiz und armasuisse Immobilien, 82pp, CHF 76.-
- 73** Scherrer SC: 2006, Interannual climate variability in the European and Alpine region, 132pp, CHF 86.-
- 72** Mathis H: 2005, Impact of Realistic Greenhouse Gas Forcing on Seasonal Forecast Performance, 80pp, CHF 75.-
- 71** Leuenberger D: 2005, High-Resolution Radar Rainfall Assimilation: Exploratory Studies with Latent Heat Nudging, 103pp, CHF 81.-
- 70** Müller G und Viatte P: 2005, The Swiss Contribution to the Global Atmosphere Watch Programme – Achievements of the First Decade and Future Prospects, 112pp, CHF 83.-
- 69** Müller WA: 2004, Analysis and Prediction of the European Winter Climate, 115pp, CHF 34.
- 68** Bader S: 2004, Das Schweizer Klima im Trend: Temperatur- und Niederschlagsentwicklung seit 1864, 48pp, CHF 18.-
- 67** Begert M, Seiz G, Schlegel T, Musa M, Baudraz G und Moesch M: 2003, Homogenisierung von Klimamessreihen der Schweiz und Bestimmung der Normwerte 1961-1990, Schlussbericht des Projektes NORM90, 170pp, CHF 40.-
- 66** Schär C, Binder P and Richner H (Eds.): 2003, International Conference on Alpine Meteorology and MAP Meeting 2003, Extended Abstracts volumes A and B, 580pp, CHF 100.
- 65** Stübi R: 2002, SONDEX / OZEX campaigns of dual ozone sondes flights: Report on the data analysis, 78pp, CHF 27.-
- 64** Bolliger M: 2002, On the characteristics of heavy precipitation systems observed by Meteosat-6 during the MAP-SOP, 116pp, CHF 36.-
- 63** Favaro G, Jeannet P and Stübi R: 2002, Re-evaluation and trend analysis of the Payerne ozone sounding, 99pp, CHF 33.-
- 62** Bettems JM: 2001, EUCOS impact study using the limited-area non-hydrostatic NWP model in operational use at MeteoSwiss, 17pp, CHF 12.-
- 61** Richner H et al.: 1999, Grundlagen aerologischer Messungen speziell mittels der Schweizer Sonde SRS 400, 140pp, CHF 42.-

Kürzlich erschienen

- 60** Gisler O: 1999, Zur Methodik einer Beschreibung der Entwicklung des linearen Trends der Lufttemperatur über der Schweiz im Zeitabschnitt von 1864 bis 1990, 125pp, CHF 36.-
- 59** Bettems J-M: 1999, The impact of hypothetical wind profiler networks on numerical weather prediction in the Alpine region, 65pp, CHF 25.-
- 58** Baudenbacher, M: 1997, Homogenisierung langer Klimareihen, dargelegt am Beispiel der Lufttemperatur, 181pp, CHF 50.-
- 57** Bosshard, W: 1996, Homogenisierung klimatologischer Zeitreihen, dargelegt am Beispiel der relativen Sonnenscheindauer, 136pp, CHF 38.-

Arbeitsberichte der MeteoSchweiz

- 223** Dürr B: 2008, Automatisiertes Verfahren zur Bestimmung von Föhn in den Alpentälern, 22pp, CHF 62.-
- 222** Schmutz C, Arpagaus M, Clementi L, Frei C, Fukutome S, Germann U, Liniger M und Schacher F: 2008, Meteorologische Ereignisanalyse des Hochwassers 8. bis 9. August 2007, 29pp, CHF 64.-
- 221** Frei C, Germann U, Fukutome S und Liniger M: 2008, Möglichkeiten und Grenzen der Niederschlagsanalysen zum Hochwasser 2005, 19pp, CHF 62.-
- 220** Ambühl J: 2008, Optimization of Warning Systems based on Economic Criteria, 79pp, CHF 75.-
- 219** Ceppi P, Della-Marta PM and Appenzeller C: 2008, Extreme Value Analysis of Wind Observations over Switzerland, 43pp, CHF 67.-
- 218** MeteoSchweiz (Hrsg): 2008, Klimaszenarien für die Schweiz – Ein Statusbericht, 50pp, CHF 69.-
- 217** Begert M: 2008, Die Repräsentativität der Stationen im Swiss National Basic Climatological Network (Swiss NBCN), 40pp, CHF 66.-
- 216** Della-Marta PM, Mathis H, Frei C, Liniger MA and Appenzeller C: 2007, Extreme wind storms over Europe: Statistical Analyses of ERA-40, 80pp, CHF 75.-
- 215** Begert M, Seiz G, Foppa N, Schlegel T, Appenzeller C und Müller G: 2007, Die Überführung der klimatologischen Referenzstationen der Schweiz in das Swiss National Climatological Network (Swiss NBCN), 47pp, CHF 68.-
- 214** Schmucki D und Weigel A: 2006, Saisonale Vorhersage in Tradition und Moderne: Vergleich der "Sommerprognose" des Zürcher Bööggs mit einem dynamischen Klimamodell, 46pp, CHF 68.-
- 213** Frei C: 2006, Eine Länder übergreifende Niederschlagsanalyse zum August Hochwasser 2005. Ergänzung zu Arbeitsbericht 211, 10pp, CHF 59.-
- 212** Z'graggen, L: 2006, Die Maximaltemperaturen im Hitzesommer 2003 und Vergleich zu früheren Extremtemperaturen, 74pp, CHF 75.-
- 211** MeteoSchweiz: 2006, Starkniederschlagsereignis August 2005, 63pp, CHF 72.-
- 210** Buss S, Jäger E and Schmutz C: 2005: Evaluation of turbulence forecasts with the aLMo, 58pp, CHF 70.-
- 209** Schmutz C, Schmuki D, Duding O, Rohling S: 2004, Aeronautical Climatological Information Sion LSGS, 77pp, CHF 25.-
- 208** Schmuki D, Schmutz C, Rohling S: 2004, Aeronautical Climatological Information Grenchen LSZG, 73pp, CHF 24.-
- 207** Moesch M, Zelenka A: 2004, Globalstrahlungsmessungen 1981-2000 im ANETZ, 83pp, CHF 26.-
- 206** Schmutz C, Schmuki D, Rohling S: 2004, Aeronautical Climatological Information St.Gallen LSZR, 78pp, CHF 25.-
- 205** Schmutz C, Schmuki D, Ambrosetti P, Gaia M, Rohling S: 2004, Aeronautical Climatological Information Lugano LSZA, 81pp, CHF 26.-
- 204** Schmuki D, Schmutz C, Rohling S: 2004, Aeronautical Climatological Information Bern LSZB, 80pp, CHF 25.-
- 203** Duding O, Schmuki D, Schmutz C, Rohling S: 2004, Aeronautical Climatological Information Geneva LSGG, 104pp, CHF 31.-

Kürzlich erschienen

- 202** Bader S: 2004, Tropische Wirbelstürme – Hurricanes –Typhoons – Cyclones, 40pp, CHF 16.-
- 201** Schmutz C, Schmuki D, Rohling S: 2004, Aeronautical Climatological Information Zurich LSZH, 110pp, CHF 34.-
- 200** Bader S: 2004, Die extreme Sommerhitze im aussergewöhnlichen Witterungsjahr 2003, 25pp, CHF 14.-

Herausgeber

Bundesamt für Meteorologie und Klimatologie, MeteoSchweiz, © 2008

MeteoSchweiz
Krähbühlstrasse 58
CH-8044 Zürich
T +41 44 256 91 11
www.meteoschweiz.ch

Weitere Standorte
CH-8058 Zürich-Flughafen
CH-6605 Locarno Monti
CH-1211 Genève 2
CH-1530 Payerne